

**Assessment of an Innovative Experimental Facility for Testing Diffusing
Serpentine Inlets with Large Amounts of Boundary Layer Ingestion**

Michael R. Hylton

Thesis submitted to the faculty of the Virginia Polytechnic Institute and State University
in partial fulfillment of the requirements for the degree of

Master of Science
in
Mechanical Engineering

Dr. Walter F. O'Brien, Co-Chairman
Dr. Wing F. Ng, Co-Chairman
Dr. Clinton L. Dancey

July 9, 2008

Blacksburg, Virginia

Keywords: Blended-Wing-Body, Boundary-Layer-Ingesting, Serpentine Inlet,
Aerodynamic Interface Plane, Distortion

Copyright © 2008 by Michael R. Hylton

Assessment of an Innovative Experimental Facility for Testing Diffusing Serpentine Inlets with Large Amounts of Boundary Layer Ingestion

Michael R. Hylton

ABSTRACT

An innovative experimental facility was developed for testing flush-mounted, diffusing serpentine inlets intended for use on blended-wing-body aircraft. The static ground test facility was able to simulate the boundary layer profile expected to be ingested by inlets mounted on the aft sections of these aircraft. It generated Mach numbers ranging from 0.19 to 0.4 and boundary layer thicknesses between 36% and 45%. The circumferential distortions at the aerodynamic interface plane of the serpentine inlet were also calculated, and ranged between 0.0042 for the lowest Mach number, to 0.0098 for the highest Mach number. Reynolds numbers for the tests ranged between 1.2 million and 2.4 million depending on engine speed and Mach number. The results of the experiment were compared to a previous NASA report, and showed close agreement in distortion patterns and pressure losses at a Mach number of 0.25.

Acknowledgements

I would like to thank Dr. O'Brien and Dr. Ng for providing guidance and support throughout the course of this project. I would also like to thank Dr. Dancey for agreeing to devote his time and knowledge by serving as a committee member. The dedication and expertise they provided have improved the quality of this work, and have helped me to grow as a person and an engineer. I would also like to thank the project sponsors NASA and UTRC, who gave me and Virginia Tech the opportunity to collaborate with them. Mr. David Arend, who was our NASA project monitor, and Dr. Razvan Florea, Dr. Bill Cousins, and Dr. Om Sharma from UTRC, who worked closely with us throughout the entire project to ensure its success.

Personally, I would like to thank my family and friends for providing unwavering support during my time here. To my Mom and Dad, who have supported me both emotionally and financially throughout my entire academic career, and to my friends, who were always there to listen and help pick me up when frustration began setting in. Their devotion and patience has and always will be appreciated.

Table of Contents

Abstract.....	ii
Acknowledgements.....	iii
Table of Contents.....	iv
List of Figures.....	v
List of Tables.....	ix
Nomenclature.....	x
1.0 Introduction.....	1
1.1 Background Information.....	1
1.2 Literature Review.....	4
1.2.1 Static Ground Test Facilities.....	4
1.2.2 Flow in Serpentine Ducts.....	7
1.3 Summary.....	10
2.0 Experimental Set-up.....	12
2.1 Overview and Purpose of Experimental Facility.....	12
2.2 Serpentine Inlet Geometry.....	17
2.3 Design of Experimental Facility.....	21
2.3.1 Computational Fluid Dynamics Simulations.....	21
2.3.2 Detailed Description of Experimental Facility.....	28
2.3.3 Structural Analysis of Experimental Facility.....	39
2.4 Instrumentation.....	46
2.5 Test Procedure.....	52
2.6 Summary.....	53
3.0 Data Reduction and Calculations.....	55
3.1 Calculations at the Throat of the Serpentine Inlet.....	55
3.2 Calculations at AIP of Serpentine Inlet.....	57
3.3 Summary.....	64
4.0 Results.....	65
4.1 Boundary Layer Profiles entering Serpentine Inlet and Bypass Duct.....	65
4.2 Static Pressure in Experimental Facility.....	80
4.3 AIP Data.....	84
4.3.1 Circumferential Distortion Elements.....	85
4.3.2 Radial Distortion Element.....	93
4.4 Wall Static Pressures in Serpentine Inlet.....	97
4.5 Comparison with NASA Results.....	99
4.6 Summary.....	104
5.0 Conclusions and Recommendations.....	106
5.1 Summary of Key Results.....	106
5.2 Recommendations for Future Research.....	108
6.0 References.....	109
Appendix A: Uncertainty Analysis.....	112
Appendix B: Material Properties for Aluminum 6061.....	114
Appendix C: Instrumentation Numbering Scheme.....	115
Appendix D: Experimental Facility Section Views.....	123

List of Figures

Figure 1.1 – Model of BWB Aircraft Design (Courtesy NASA)	2
Figure 1.2 – Typical Geometry for Early Tests on Serpentine Ducts.....	8
Figure 1.3 – Diffusing Serpentine Duct Geometry	9
Figure 2.1 – NASA Inlet A Removable Test Section.....	13
Figure 2.2 – Pratt and Whitney JT15D-1 Gas Turbine Engine.....	14
Figure 2.3 – Desired Boundary Layer Profile at Inlet Lip.....	16
Figure 2.4 – Computer-Generated Perspective of Inlet Tested.....	18
Figure 2.5 – Front View of Inlet A Throat Geometry.....	19
Figure 2.6 – Complete EPS Machined Inlet	20
Figure 2.7 – Pressure Losses with Flat Plate Design	22
Figure 2.8 – NACA Airfoil Inlet Design	23
Figure 2.9 – CFD Model of Inlet Ramp.....	23
Figure 2.10 – Pressure Losses with 4” Ramp Design.....	24
Figure 2.11 – Pressure Losses with 5.5” Ramp Design.....	25
Figure 2.12 – Local Mach Numbers around Inlet and at AIP.....	25
Figure 2.13 – Static Pressures throughout Experimental Facility.....	26
Figure 2.14 – Summary of Boundary Layer Profiles.....	27
Figure 2.15 – CFD Model showing Revised Bypass Duct Profile	28
Figure 2.16 – Overall CAD Model of Experimental Facility	29
Figure 2.17 – Serpentine Inlet with Base Plate and Mating Pipe	30
Figure 2.18 – Rear Plenum Chamber.....	30
Figure 2.19 – Inlet Control Device inside Rear Plenum.....	31
Figure 2.20 – Wind Tunnel-Plenum Junction Plate.....	32
Figure 2.21 – Bypass Duct Blockage Plate.....	33
Figure 2.22 – Outer Structure of Bypass Duct.....	34
Figure 2.23 – Removable Section of Lexan.....	35
Figure 2.24 – 5.5 inch Inlet Boundary Layer Generation Ramp	36
Figure 2.25 – Outer Structure of Inlet Ramp Cover	37
Figure 2.26 – Bellmouth on Front of Experimental Facility	38
Figure 2.27 – Completed Experimental Facility.....	39
Figure 2.28 – Mesh Between Circumferential Supports and Aluminum Skin	41
Figure 2.29 – FEA Model with Loads and Constraints Applied	42
Figure 2.30 – Resulting Stresses in Experimental Facility	43
Figure 2.31 – Resulting Displacements in Experimental Facility	43

Figure 2.32 – Resulting Displacements Associated with Buckling Failure	44
Figure 2.33 – Internal View of Rivet Construction Technique	45
Figure 2.34 – External View of Rivet Construction Technique	46
Figure 2.35 – Boundary Layer Rake Installed in Center of Inlet.....	47
Figure 2.36 – Bypass Duct Rakes Installed	48
Figure 2.37 – Static Pressure Taps in Serpentine Inlet	49
Figure 2.38 – Static Pressure Taps in Experimental Facility	50
Figure 2.39 – AIP Rake Installed.....	51
Figure 3.1 – Circumferential Locations of Arms on AIP Rake	58
Figure 3.2 – Typical Ring Total Pressure Plot.....	59
Figure 3.3 – Typical Total Pressure Plot for a Multiple-per-Revolution Pattern	61
Figure 3.4 – Typical Radial Distortion Intensity Graph	63
Figure 4.1 – Boundary Layer Profile with Engine Operating at 55% Speed.....	66
Figure 4.2 – Non-dimensionalized Boundary Layer Profile with Engine Operating at 55% Speed.....	67
Figure 4.3 – Boundary Layer Profile with Engine Operating at 65% Speed.....	68
Figure 4.4 – Non-dimensionalized Boundary Layer Profile with Engine Operating at 65% Speed.....	68
Figure 4.5 – Air Flow through Bypass Duct and Serpentine Inlet Generating a Thick Boundary Layer Profile.....	69
Figure 4.6 – Air Flow through Bypass Duct and Serpentine Inlet Generating the Correct Boundary Layer Profile.....	70
Figure 4.7 – Boundary Layer Profile with Engine Operating at 65% Speed and 54% Bypass Duct Blockage	71
Figure 4.8 – Non-dimensionalized Boundary Layer Profile with Engine Operating at 65% Speed and 54% Bypass Duct Blockage	72
Figure 4.9 – Boundary Layer Profile with Engine Operating at 75% Speed and 54% Bypass Duct Blockage	73
Figure 4.10 – Non-dimensionalized Boundary Layer Profile with Engine Operating at 75% Speed and 54% Bypass Duct Blockage.....	74
Figure 4.11 – Predicted Mass Flow Rates at 75% Engine Speed	75
Figure 4.12 – Predicted Bypass Duct Exit Area at 75% Engine Speed	75
Figure 4.13 – Bypass Duct Profile with Engine Operating at 55% Speed	77
Figure 4.14 – Bypass Duct Profile with Engine Operating at 65% Speed	77
Figure 4.15 – Bypass Duct Profile with Engine Operating at 65% Speed and 54% Bypass Duct Blockage.....	78
Figure 4.16 – Bypass Duct Profile with Engine Operating at 75% Speed and 54% Bypass Duct Blockage.....	78

Figure 4.17 – Local Static Pressures in Experimental Facility at 55% Engine Speed.....	80
Figure 4.18 – Local Static Pressures in Experimental Facility at 65% Engine Speed.....	81
Figure 4.19 – Local Static Pressures in Experimental Facility at 65% Engine Speed with 54% Bypass Duct Blockage.....	83
Figure 4.20 – Local Static Pressures in Experimental Facility at 75% Engine Speed with 54% Bypass Duct Blockage.....	84
Figure 4.21 – Circumferential Distortion Graphs at 55% Engine Speed.....	86
Figure 4.22 – AIP Total Pressure Loss at 55% Engine Speed.....	86
Figure 4.23 – Multiple-per-Revolution Pattern for Inlet at 55% Engine Speed	88
Figure 4.24 – Circumferential Distortion Graphs at 65% Engine Speed.....	89
Figure 4.25 – AIP Total Pressure Loss at 65% Engine Speed.....	89
Figure 4.26 – Multiple-per-Revolution Pattern for Inlet at 65% Engine Speed	90
Figure 4.27 – Circumferential Distortion Graphs at 65% Engine Speed with 54% Bypass Duct Blockage.....	91
Figure 4.28 – AIP Total Pressure Loss at 65% Engine Speed with 54% Bypass Duct Blockage	92
Figure 4.29 – Multiple-per-Revolution Pattern for Inlet at 65% Engine Speed with 54% Bypass Duct Blockage	93
Figure 4.30 – Radial Distortion Graph at 55% Engine Speed	94
Figure 4.31 – Radial Distortion Graph at 65% Engine Speed	95
Figure 4.32 – Radial Distortion Graph at 65% Engine Speed with 54% Bypass Duct Blockage	96
Figure 4.33 – Static Pressure Losses in Serpentine Inlet at 55% Engine Speed.....	98
Figure 4.34 – Static Pressure Losses in Serpentine Inlet at 65% Engine Speed.....	98
Figure 4.35 – Static Pressure Losses in Serpentine Inlet at 65% Engine Speed with 54% Bypass Duct Blockage	99
Figure 4.36 – Comparison of Non-dimensionalized Boundary Layer Profiles	101
Figure 4.37 – NASA Total Pressure Loss at AIP	103
Figure C.1 – AIP Rake (Looking through AIP from Upstream)	115
Figure C.2 – Boundary Layer Rake	116
Figure C.3 – Bypass Duct Rakes (Looking through Bypass Duct from Upstream)	117
Figure C.4 – Serpentine Inlet Static Pressure Taps (View 1 of 2).....	118
Figure C.5 – Serpentine Inlet Static Pressure Taps (View 2 of 2).....	119
Figure C.6 – Static Pressure Taps in Experimental Facility	120
Figure D.1 – Detailed Description of Experimental Facility.....	123
Figure D.2 – Locations of Section Views in Experimental Facility.....	123
Figure D.3 – Section View A.....	124
Figure D.4 – Section View B.....	124

Figure D.5 – Section View C.....	124
Figure D.6 – Section View D.....	125
Figure D.7 – Section View E.....	125
Figure D.8 – Section View F.....	126
Figure D.9 – Section View G.....	126

Note: The figures included in this thesis are the work of the author unless otherwise referenced.

List of Tables

Table 2.1 – Location of Probes on Boundary Layer Rake.....	47
Table 2.2 – Radial Locations of Bypass Duct Probes.....	48
Table 2.3 – Radial Locations of Probes on AIP Rake	51
Table 4.1 – Circumferential Distortion Intensities at 55% Engine Speed	87
Table 4.2 – Circumferential Distortion Extents at 55% Engine Speed.....	87
Table 4.3 – Circumferential Distortion Intensities at 65% Engine Speed	90
Table 4.4 – Circumferential Distortion Extents at 65% Engine Speed.....	90
Table 4.5 – Circumferential Distortion Intensities at 65% Engine Speed with 54% Bypass Duct Blockage.....	92
Table 4.6 – Circumferential Distortion Extents at 65% Engine Speed with 54% Bypass Duct Blockage.....	92
Table 4.7 – Radial Distortion Intensities at 55% Engine Speed.....	94
Table 4.8 – Radial Distortion Intensities at 65% Engine Speed.....	95
Table 4.9 – Radial Distortion Intensities at 65% Engine Speed with 54% Bypass Duct Blockage	96
Table 4.10 – NASA Experimental Results	102
Table B.1 – Summary of Aluminum 6061 Material Properties.....	114
Table C.1 – Measurement Locations in Experimental Facility	121
Table C.2 – Measurement Locations at AIP of Serpentine Inlet	122

Nomenclature

3D	Three-Dimensional
A_c	Cross-sectional area (ft ²)
AIP	Aerodynamic Interface Plane
ASME	American Society of Mechanical Engineers
ARP	Aerospace Recommended Practice
BWB	Blended-Wing-Body
BLI	Boundary-Layer-Ingesting
C_p	Specific heat at constant pressure
C_v	Specific heat at constant volume
CAD	Computer Aided Drawing
CFD	Computational Fluid Dynamics
CNC	Computer Numerical Controlled
D_c	Characteristic length (ft)
$DPCP_i$	Circumferential distortion intensity for ring i
$DPRP_i$	Radial distortion intensity for ring i
EPS	Expanded Polystyrene
FEA	Finite Element Analysis
h_{max}	Maximum height at serpentine inlet lip
ICD	Inlet Control Device
ISA	Instrumentation Systems and Automation
ITT	Inter-Turbine Temperature
k	Indexing variable used to refer to the k -th low pressure region
L	Overall axial length of serpentine inlet
M	Mach number
M_{ave}	Average Mach number
\dot{m}	Mass flow rate (lb _m /s)
MPR_i	Multiple-per-revolution value for the i -th ring at the AIP
N	Number of radial rings on AIP rake
NACA	National Advisory Committee for Aeronautics
NASA	National Aeronautics and Space Administration
p_o	Total pressure (psi)
p_s	Static pressure (psi)
P_∞	Atmospheric pressure (psi)

PAV_i	Average total pressure for a ring (psi)
$PAVLOW_i$	Average total pressure in the low pressure region (psi)
$PFAV$	Area weighted face average total pressure (psi)
$P(\theta)_i$	Total pressure at a specific location on the AIP rake (psi)
psi	Pounds per square inch
Q	Number of low pressure regions for a multiple-per-revolution pattern
R	Gas constant for air (psi*ft ³ /lb _m *R)
SAE	Society of Automotive Engineers
T	Temperature (°F)
UTRC	United Technologies Research Center
V_{ave}	Average velocity (ft/s)
x	Axial position of static pressure taps in serpentine inlet
$\left(\frac{\Delta PC}{P}\right)_i$	Circumferential distortion intensity for a ring
γ	Ratio of specific heats
μ	Dynamic viscosity (lb _m /ft*s)
θ_{1i}	Radial location of beginning of AIP low pressure region (degrees)
θ_{2i}	Radial location of end of AIP low pressure region (degrees)
θ_i^-	Extent of circumferential distortion (degrees)
θ_{i1}^-	Extent of first low pressure region for a multiple-per-revolution pattern (degrees)
θ_{i2}^-	Extent of second low pressure region for a multiple-per-revolution pattern (degrees)
θ_{i1}^+	Extent of first high pressure region for a multiple-per-revolution pattern (degrees)
θ_{i2}^+	Extent of second high pressure region for a multiple-per-revolution pattern (degrees)
ρ	Density (lb _m /ft ³)

1.0 Introduction

1.1 Background Information

With aircraft design moving forward in the twenty-first century, a new program was initiated by NASA to investigate revolutionary new designs for airplanes. This initiative was titled the Ultra Efficient Engine Technology program, and was tasked with designing a next-generation hybrid wing aircraft using embedded engines (Owens et al. 2006). These airplanes are known as blended-wing-body (BWB) aircraft because the wings and fuselage are not separate and distinct parts of the airplane. Instead, these two parts are blended together to form one solid, triangular-shaped design that incorporates the fuselage and wings. The advantages of an aircraft having this design are an increase in the lift-to-drag ratio of the plane, a reduction in the empty and takeoff weights for the plane, and smaller thrust requirements resulting in a decrease in fuel consumption. A BWB transport plane design would also have capacities of up to eight hundred passengers because of multiple cabin levels (Liebeck et al. 1998). Figure 1.1 below shows a model of a planned BWB airplane design.

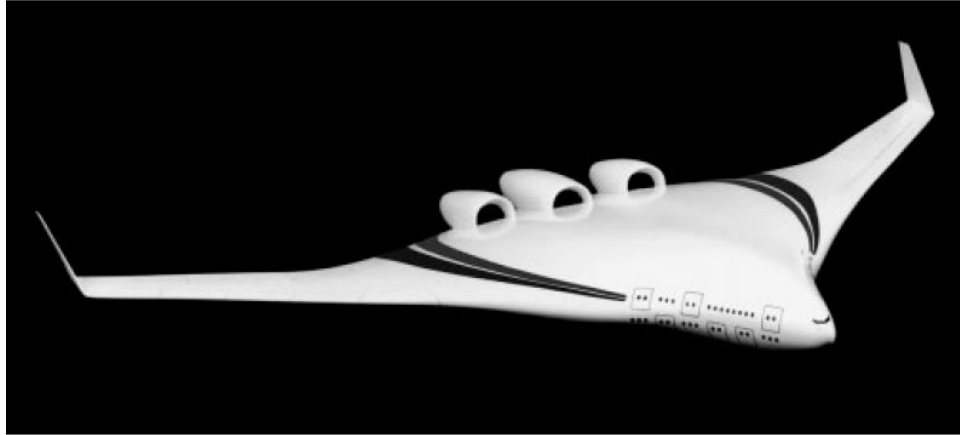


Figure 1.1 – Model of BWB Aircraft Design (Courtesy NASA)

While many benefits are realized by such an aircraft, there are also many challenges that must be solved before the design can be implemented. As can be seen in the figure above, one unique aspect of the BWB design is that the engines can be embedded on the aft section of the aircraft, reducing drag. An alternate design has the engines mounted on pylons either above the rear part of the airplane or on the sides below the wings. With these podded designs, the engine inlet sits in the freestream and is able to ingest essentially uniform airflow. With an embedded design, the engines are no longer mounted in the freestream, but will ingest a boundary layer flow produced by the wing. The engines are mounted inside the airframe, obstructing the ability of the engine inlet to deliver flow to the engine. This problem is solved by using serpentine inlets to duct air flow into the embedded engine. A serpentine inlet typically has an elongated s-shaped design that is able to offset the flow by turning it through an enclosed duct. This duct solves the problem of delivering flow to the embedded engine, but creates other problems because of the distortion and pressure loss associated with turning the air. These pressure losses and distortions must be minimized to ensure stable and high efficiency operation of the engine during flight.

As previously mentioned, another problem that must be addressed when mounting serpentine inlets on the aft sections of BWB aircraft is the boundary layer that develops as air flows across the front portion of the aircraft. This boundary layer increases the flow distortion and pressure losses inside the serpentine inlet because of the non-uniformity of the flow entering the inlet. Because the serpentine inlets on BWB aircraft must ingest this wing-generated boundary layer, they are often referred to as boundary-layer-ingesting (BLI) inlets. Although serpentine inlets are currently in use on several commercial and military aircraft such as the Boeing 727, Lockheed Tristar L-1011, General Dynamics F-16, and McDonnell-Douglas F-18 (Harloff et al. 1992), the problems associated with BLI inlets has not been studied in great detail (Berrier et al. 2005). This is because the serpentine inlets on these aircraft are mounted either on the front portion of the aircraft, or away from the fuselage and aircraft body when aft mounted, where they are able to ingest flow that is almost uniform (Ting et al. 1975).

With possible future aircraft designs being based on the BWB structure, a method for testing and evaluating the inlets and engines for use in these airplanes must be developed. The present thesis examines the design and development of a unique experimental facility that can be used to test the interaction between a simulated BWB aircraft boundary layer developed at the front of a serpentine inlet, and the resulting effect it has on the distortion and pressure loss at the engine-face aerodynamic interface plane (AIP). It provides an important step toward the development of testing full-scale inlets and engines that are integrated together in one static ground test facility. After a review of past literature containing information on ground test facilities and the development of flow in serpentine inlets, this thesis will detail the design of the

experimental facility used to test a diffusing serpentine inlet with large amounts of boundary layer ingestion. It will review the methods and calculations used to characterize the flow at the front and at the AIP of the inlet, and will present experimental results obtained showing the effectiveness of the facility at duplicating the boundary layer growth expected along the surface of BWB aircraft, and the associated flow effects in the serpentine inlet. Finally, this thesis will show how the experiments conducted benefit the inlet design community by outlining future research that can be performed based on the knowledge and experience obtained here.

1.2 Literature Review

1.2.1 Static Ground Test Facilities

As new technologies and tools are developed for designing and testing aircraft systems and components, they lead to new ideas that alter standard designs and practices that have been established for many years. One of these areas is the development of a method for testing aircraft engines and inlets. Until recently, the standard practice for testing engine components was to test them individually as isolated systems. This process began with the aircraft manufacturer designing and testing an aircraft engine inlet in a wind tunnel. Data were collected at the AIP of the inlet to describe the flow and distortion that was generated. These measurements were then provided to engine manufacturers who designed a series of tests using screens to duplicate the distortion created by the inlet. Tests were then run at varying conditions to develop the operating lines and stall margin for the engine (Davis, et al. 2002).

A problem with conducting the tests on isolated parts is the inability to capture and recreate certain interactions only present when the pieces are coupled together. A failure to test for these interactions and their resulting effects on the performance of the system has led to airframes being mated to engines where certain desired operational limits are unable to be reached (Anderson 1983). The complex interactions present at the interface between inlets and engines were addressed by Smith (1996) when he reviewed the history and progress of ground test facilities. His work was focused on the interactions between turbofan and turbojet engines with their corresponding inlets, which are the types of engines that would be installed on BWB aircraft. He found that the interface affected the entire system in three main areas; performance, operability, and durability and reliability. *Performance* dealt with the affect the engine-inlet interface had on successfully completing the tasks of a mission. *Operability* looked at how the engine-inlet interface changed the expected response of the system when a pilot altered the controls. The *durability and reliability* aspect examined how the interface affected the readiness of aircraft for flight. Smith compiled an extensive list of factors and interactions for each of these three broad categories to show the complexity involved when mating the two pieces. He outlined one case pursued by the Lockheed Corporation during World War II where the design process examined the engine-inlet connection using a system level approach where ground test facilities were used to test the interactions. This cutting-edge idea appeared to be the future for designing airframes and engines, but was slow to catch on because of the long lead times and large investments in capital money required.

Davis, Hale, and Beale (2002) brought to light other issues not raised by Smith concerning the integration of engines and inlets for system level tests. Their study involved a numerical approach to address the problems associated with variations in total pressure during unsteady and transient operation, along with circumferential swirl created at the AIP of inlets. Typically, manufacturer tests have ignored these two phenomena. However, recent engine tests showed that the performance of engines without inlet guide vanes was highly sensitive to swirl at their inlets. The presence of swirl is a common problem associated with serpentine inlet diffusers because of rotating vortices that form at the exit of the duct (Harloff et al. 1992). Since BWB aircraft may implement serpentine inlets, the need to develop a way to model and test this interaction becomes even more important. An examination of wind tunnel test results also revealed that transient distortion patterns and pressure losses can be much larger than those values recorded at steady-state. Since most distortion tests are run at steady-state for engines and inlets, this creates a vacancy in the operational information for an inlet and engine connection. Mating the components together for an integrated static ground test would allow any problems generated to be noticed and addressed. It has also been shown that swirl combined with a total pressure distortion in front of a rotating fan can cause the engine to surge even if the distortion was deemed acceptable by standard means (Davis et al. 2002).

Beale (2001) proposed that integrating airframe and propulsion systems for static ground tests is needed for further development of more advanced aircraft. Because airplanes today are able to operate at higher Mach numbers and are more maneuverable due to thrust vectoring capabilities, designers are having difficulty determining the

complex interactions between aircraft components. More advanced static ground test facilities with integration capabilities are needed for designers to continue to develop new technologies and airplanes.

1.2.2 Flow in Serpentine Ducts

Flow through serpentine ducts has been examined by many different researchers in many different ways over the years (Harloff et al. 1992; Wellborn et al. 1994; Berrier et al. 2005; Plas et al. 2007). These investigations have been both numerical and experimental, and have involved a variety of geometries and flow conditions. Most of this research has been performed on ducts of either circular or square cross-sectional areas that contain two curves in opposite directions. The ducts tested also typically have some ratio of diffusion from the inlet area to the exit area, causing the flow to decelerate. This diffusion is useful for serpentine inlets that are installed on aircraft because the diffused flow has a higher pressure and matches the engine inlet flow velocity requirements, which improves the performance of the jet engine. Although the diffusion of serpentine inlets helps engines, the ducts have other characteristics that affect the flow so as to reduce the performance of engines, as described below. This section will summarize some of the key results from the previous research that has been conducted that are applicable to the experiment being performed here.

Figure 1.2 below shows a typical shape used for early tests on serpentine duct geometries. The figure shows two opposing turns of equal radius, and a constant circular cross-sectional area. A series of experimental and numerical research was performed on

this duct, resulting in some early conclusions about the flow through curved ducts. Experimental results showed that as the speed of the flow through the duct was increased, the thinner boundary layers developed inside the duct resulted in smaller secondary flows around the inflection points in the duct (Taylor et al. 1984). However, these secondary flows were still large enough to create complex, three-dimensional flow at the exit of the duct. These secondary flows caused rotating vortices along the top surface of the duct resulting in large flow distortions (Towne 1984).

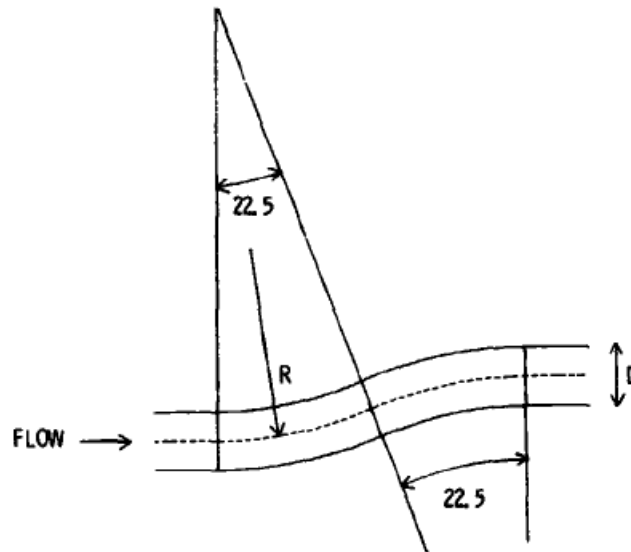


Figure 1.2 – Typical Geometry for Early Tests on Serpentine Ducts (Towne 1984)

Another important investigation was performed by Harloff, et al. (1992) and Wellborn, et al. (1994) that examined the effect on the flow when it passed through a diffusing serpentine duct. Figure 1.3 below shows a half-shell model of the diffusing duct tested in those experiments. The diffusion added another layer of complexity not seen in many tests up to that date. Altering the cross-sectional area of the duct generated large streamline curvature. This streamline curvature then created adverse pressure

gradients along the surface of the duct, leading to significant secondary flows. These secondary flows and adverse pressure gradients caused significant flow separation along the bottom surface of the duct after the second curve. Knowledge of these regions of flow separation is of critical importance to airframe and engine manufacturers. As Reichert and Wendt (1994) pointed out, these secondary flows that form rotating vortices at the exit of the duct are responsible for much of the distortion at the inlet AIP. Inlet designers need to reduce the size of the separation and distortion, while engine designers must design engines capable of withstanding the distortions and pressure losses created. Wellborn et al. (1994) also concluded that the flow through the duct was symmetrical by examining oil flow patterns through the duct. The results of these studies are of particular importance here because the diffusing geometry used in their experiments closely resembles the inlet tested in the Wellborn experiment.

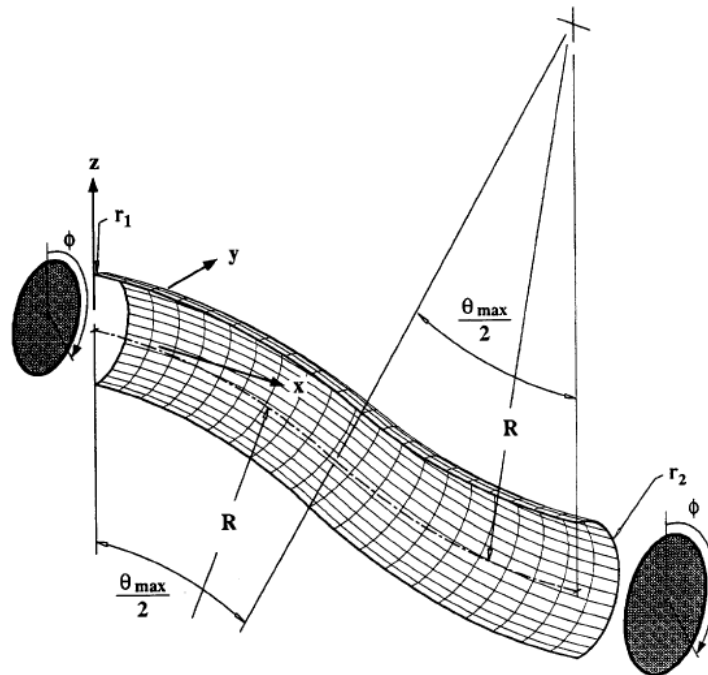


Figure 1.3 – Diffusing Serpentine Duct Geometry (Wellborn et al. 1994)

Three recent research projects have been conducted using similar experimental methods to those being applied here. The first was performed by Rabe (2003) at Virginia Tech, where a half-scale serpentine inlet for use in military aircraft was tested. This project used a jet engine to create suction through the serpentine inlet, generating Mach numbers up to 0.55 through the inlet, representing cruise conditions for the aircraft. The second was conducted by Tournier (2005) at Massachusetts Institute of Technology, where a small-scale model of an inlet used on subsonic cruise missiles was tested. This project used a one megawatt De Laval air compressor to generate suction through the serpentine inlet for Mach numbers up to 0.88. An inlet distortion screen was also placed in front of the inlet opening to help generate a fifteen percent boundary layer thickness for the entering flow. The last project was done by NASA, and formed the basis for the work being done here (Berrier et al. 2005). The work conducted by NASA focused on experimental tests and numerical simulations on a flush-mounted, serpentine inlet. The same inlet geometry was used here so that a comparison of results could be made for validation. The NASA project resulted in several papers that were used here for background information and as references (Allan and Owens, 2006; Allan et al. 2006; Owens et al. 2006).

1.3 Summary

The previous sections provide some background information and motivation for the investigation reported here. The decision by NASA to start a program designing a hybrid wing aircraft as the basis for the next generation of airplanes created the need for an experimental facility for testing candidate engine inlet designs. As the background on

the history of static ground test facilities showed, this new experimental facility should seek to integrate the inlet and engine into one system for testing, because of the complex interactions not accounted for in individual tests. Because the engines in these BWB aircraft will be embedded in the aft section of the airframe, serpentine inlets must be used to duct the air into the engine. These inlets will need to be able to ingest boundary layers that form as air flows over the outer surface of the airplanes. Many previous projects and tests have been conducted on serpentine ducts, a key sampling of which was covered previously. These tests showed the flow separations and vortices likely to form at the AIP due to the adverse pressure gradients and diffusing cross-sectional area.

2.0 Experimental Set-up

The following sections of this chapter will discuss details of the design and development of the experimental set-up. It will cover the purpose of the facility, the simulations performed to ensure the flow was generated accurately and safely, and a description of the components used in constructing the experimental rig. The instrumentation plan including locations and types of measurements taken will also be covered, along with the test procedure followed when operating the engine and rig.

2.1 Overview and Purpose of Experimental Facility

To test the serpentine inlet being used in this research, an experimental facility needed to be designed and constructed. The purpose of this facility was to generate a flow entering the inlet that would be similar to the flow encountered by the inlet under actual flight conditions. The experimental facility may be described as a specialized wind tunnel for serpentine inlet testing.

The flight conditions desired for this experiment were based on a National Aeronautics and Space Administration (NASA) experiment where several different flush-mounted serpentine inlets were tested (Berrier et al. 2005). The experiments were performed in the 0.3-Meter Transonic Cryogenic Tunnel located at the Langley Research Center. The tunnel was closed-loop, fan-driven, and had a thirteen inch by thirteen inch cross-sectional test area. The AIP of the inlets tested were vented to the atmosphere, so flow through the inlet and tunnel was generated by increasing and maintaining the air

pressure inside the tunnel greater than atmospheric pressure. To ensure continuous flow through the inlets being tested, the ratio of freestream total pressure to atmospheric pressure was kept at a value of two or greater for the duration of the test. Maintaining the conditions described above allowed NASA to test four different inlet designs at a range of Mach numbers from 0.25 to 0.83 and a range of Reynolds numbers from 5.1 million to 13.9 million. The AIP diameter was used as the characteristic length for calculating the Reynolds number, and was a constant 2.448 inches for all of the inlet designs tested. Figure 2.1 below shows one of the designs tested, labeled as inlet A. This was the inlet design chosen to validate the new experimental set-up. The figure also shows a set of fences in front of the inlet opening, along with a set of probes used to measure the boundary layer profile. The fences were installed to help generate a boundary layer similar to what would be created as air flows over the fuselage of a BWB aircraft while cruising at altitude (Berrier, et al. 2005). The details of this boundary layer are described below in more detail.



Figure 2.1 – NASA Inlet A Removable Test Section

Using the NASA experiment as a reference allowed the data collected here to be compared with a previous set of data and results. Comparing the data and results between the two experiments created an important baseline of information about the new facility that should prove beneficial in conducting future tests.

With knowledge of the NASA experimental set-up and flow conditions, a suction wind tunnel was designed and developed for use in this experiment as a static ground test facility. One unique aspect of the wind tunnel was the use of a jet engine to create the suction flow through the tunnel as opposed to a fan or compressor. Using a jet engine allowed for a more realistic representation of the flow that would be drawn in through the serpentine inlet compared to the flow that would be generated using a fan or compressor. The jet engine used during the experiment was the Pratt and Whitney JT15D-1 turbofan shown below in Figure 2.2.



Figure 2.2 – Pratt and Whitney JT15D-1 Gas Turbine Engine

The JT15D-1 contained a single-stage transonic axial fan, and a single-stage high pressure centrifugal compressor for the core air flow. The engine had a maximum mass

flow rate of 73 pounds-mass per second when operated at ninety-nine percent rated power. With a bypass ratio for the fan of 3.3:1, rated flow is comprised of a mass flow rate of 17 pounds-mass per second through the core and a mass flow rate of 56 pounds-mass per second through the bypass. The maximum overall compressor pressure ratio for the engine was 8.1:1. Power was delivered to the engine using a combination of high and low pressure turbines. A single stage high pressure turbine was used to provide power for the high pressure centrifugal compressor, while a two stage low pressure turbine was used to provide power to the fan (Pratt and Whitney Customer Training Manual, 1999).

The engine was capable of delivering a maximum thrust of 2200 pounds with a maximum thrust specific fuel consumption of 0.540 pounds per hour per pounds of thrust. It had a dry weight of 516 pounds, and was mounted to a steel sled containing the latter part of the experimental set-up. The flexible engine mount for the JT15D-1 allowed it to move forward and backward during operation, preventing a significant amount of vibration from being transferred to the sled and the experimental set-up. Further damping and isolation of the engine vibration was achieved using a specially designed inflatable seal around the engine inlet. The fan face had an inlet diameter of twenty-one inches, which is important when considering the size of the serpentine inlet being tested. Testing a serpentine inlet with a smaller exit diameter would change the velocity and mass flow that could be pulled through the inlet, causing the engine to possibly surge or stall. Precautions were taken to prevent this from happening, and will be discussed in the following sections (Pratt and Whitney Customer Training Manual, 1999).

Although the JT15D-1 is capable of running at ninety-nine percent power for the fan and ninety-five percent power for the high pressure turbine for sustained periods of time, installation of a rear plenum chamber and inlet control device (ICD) in front of the fan inlet limited the engine to operation at ninety percent high pressure turbine power. The purpose of these two pieces of the experimental set-up will be discussed later. Maximum power could not be achieved because the inter-turbine temperature (ITT) reached its maximum allowable continuous operating value of 680 degrees Celsius.

Because the serpentine inlet tested was intended for use in BWB aircraft, the experimental facility needed to be able to generate a thirty percent thickness boundary layer profile. A thirty percent boundary layer profile for the tests conducted here means the air flow reaches its freestream velocity at a distance from the bottom of the inlet that is equal to thirty percent of the maximum height of the inlet. For the following sections, this boundary layer profile will be referred to as fully developed. Since the inlet tested here had a maximum height of 8.375 inches at its lip, the flow boundary layer needed to be fully developed at a height of 2.513 inches. A representation of the boundary layer desired is shown below in Figure 2.3.

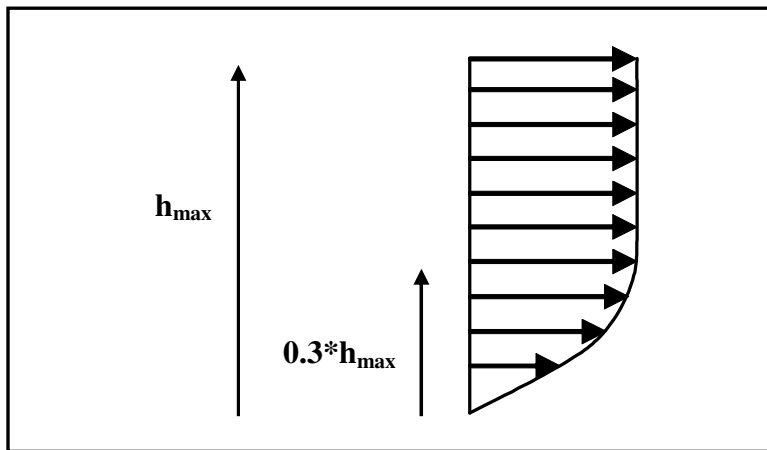


Figure 2.3 – Desired Boundary Layer Profile at Inlet Lip

In an actual aircraft installation, this boundary layer would be caused by the serpentine inlets being mounted on the aft sections of BWB aircraft. As air flows over the upper body of the airplane, a boundary layer grows. The serpentine inlet then swallows the resulting flow at the rear of the airplane. Because the inlet has an entrance flow that contains a boundary layer and is not uniform across the entire height of the inlet lip, the serpentine duct is referred to as a BLI inlet. The boundary layer profile shown above needed to be present at the lip of the serpentine inlet for an accurate simulation of the BWB cruise flight conditions.

In addition to the thirty percent boundary layer profile, a Mach number of 0.5 was desired across the front face of the serpentine inlet. This Mach number was chosen because it represented a realistic flight speed for BWB aircraft during operation. In the initial tests of the wind tunnel-engine system reported here, a maximum Mach number across the face of the inlet of 0.39 was achieved. Generating this Mach number was done by controlling the operating power of the JT15D-1 engine. Allowing the engine to run at seventy-five percent of rated fan speed resulted in the maximum Mach number above. It is expected that a higher inlet face Mach number will be achieved in future tests.

2.2 Serpentine Inlet Geometry

The geometry for the serpentine inlet used in the experimental set-up was based on the inlet A configuration that was tested in the NASA experiment. This inlet design was developed for NASA by Boeing and was intended for use on BWB transport planes

and on certain military aircraft. A computer-generated perspective of inlet A is shown below in Figure 2.4.

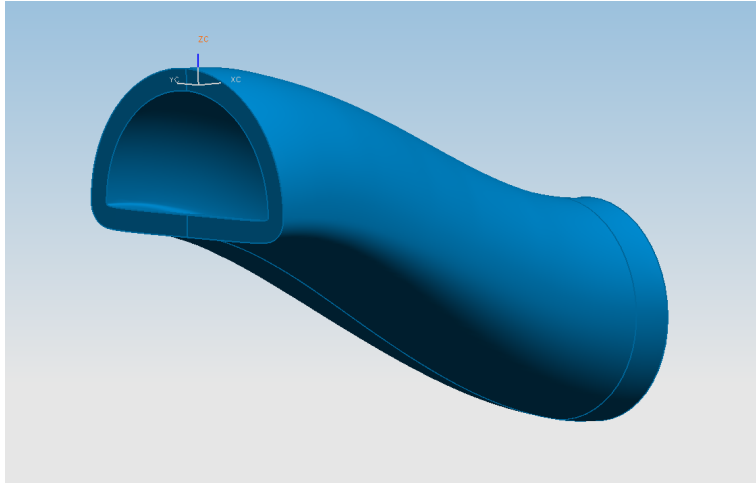


Figure 2.4 – Computer-Generated Perspective of Inlet Tested

The geometry shown is a diffusing serpentine inlet capable of ingesting large boundary layers that are not fully developed. It is designed to be mounted flush with the outer skin of BWB aircraft, and is used to duct air into the engines that are mounted inside the frame of the airplane. The NASA inlet tested had a maximum front throat height of 1.703 inches, maximum throat width of 3.249 inches, and an AIP exit diameter of 2.448 inches. The experiment conducted here used a larger scale version of the same inlet design with a desired AIP exit diameter of 12 inches. The ratios for all other dimensions were kept the same, resulting in a maximum front throat height of 8.348 inches and maximum throat width of 15.926 inches. The front throat geometry for the inlet was elliptical, but closely resembled a semi-circular area. Figure 2.5 below shows a front view of the inlet throat looking downstream (Berrier et al. 2005).

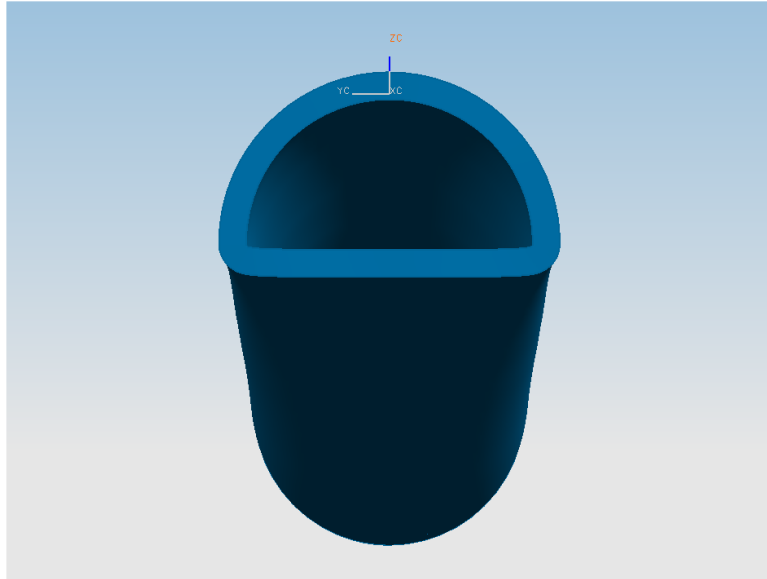


Figure 2.5 – Front View of Inlet A Throat Geometry

The diffuser design for the inlet was based on the Gerlach shaping criterion (Berrier et al. 2005). This design criterion helped determine the desired cross-sectional area of the inlet at different locations by controlling secondary flows. If the local speed of the flow was too slow, the cross-sectional area was decreased to help speed the flow up, and if the local flow speed was too high, the cross-sectional area was increased to help slow the flow down. The result was a duct with a complex curvature that transformed from a partial elliptical shape at the front to a circular shape at its exit. The circular geometry at the AIP is important because the inlet must be able to be mounted in front of an aircraft engine, which also has a circular inlet. The diffusion ratio of the outlet area of the duct to the inlet area of the duct was 1.083.

Due to the complex curvature of the inlet, it was fabricated using four solid blocks of high-density expanded polystyrene (EPS) that were machined to shape using a computer numerical controlled (CNC) machine. The blocks were then glued together and

sanded smooth to form the final inlet geometry. The completed EPS inlet is shown below in Figure 2.6.



Figure 2.6 – Complete EPS Machined Inlet

Because of the high-speed flows expected in the experiment and the resulting large pressure differentials, the strength of the EPS inlet was a concern. This was resolved by covering the inlet with a special primer paint and polyurethane coating. The primer paint was needed to seal the surface of the inlet to prevent air from leaking through, altering the chemical reaction and curing process of the polyurethane coating. Since the primer sealed the surfaces of the inlet, it made the inlet airtight, preventing any air from being pulled in through the inlet during testing. Once cured, the polyurethane coating created a hard structural outer shell covering the EPS inlet, increasing its strength. This extra structural support was important to provide the necessary strength of the inlet to sustain the pressures created by the high velocity internal flow. Four polyurethane coatings were applied to the outer surface of the inlet, but only two coatings were applied to the inner surface. Fewer coatings were applied to the inside surface of

the inlet to prevent the inner dimensions from being altered due to the extra layers of coating. In the testing reported herein, the coated duct demonstrated adequate strength, and operated without incident.

2.3 Design of Experimental Facility

The design process followed to develop an experimental facility (wind tunnel) capable of generating the desired boundary layer profile, mass flow, and freestream Mach numbers are explained in detail in the following sections. The design of the facility included work in three major areas: computational fluid dynamics (CFD) simulations, three-dimensional computer aided drawing (CAD) models, and finite element analysis (FEA) simulations.

2.3.1 Computational Fluid Dynamics Simulations

The CFD simulations for the wind tunnel were performed by the project sponsor United Technologies Research Center (UTRC) using the commercial CFD code CFL3D (Florea, 2008). These simulations were used to determine the internal flow path of the air that was needed to generate the boundary layer desired. CFD was chosen as the preferred method for determining the flow path required because of its ability to generate alternate design solutions, and to close on an optimum geometry in a relatively short amount of time. The unique requirements of the experimental facility meant that several iterations of different designs would need to be tested before a final design would be selected. Although the CFD simulations took between eight and fourteen hours to converge

depending on the size of the mesh and the speed of the flow in the simulation, this time was small when compared to the time that would be involved in constructing and testing different designs. Three major design ideas were tested using CFD. The first design involved placing a flat plate even with the bottom surface of the inlet inside a semi-circular duct. This design produced a boundary layer thickness of only eight percent and almost no distortion at the AIP, as seen below in Figure 2.7.

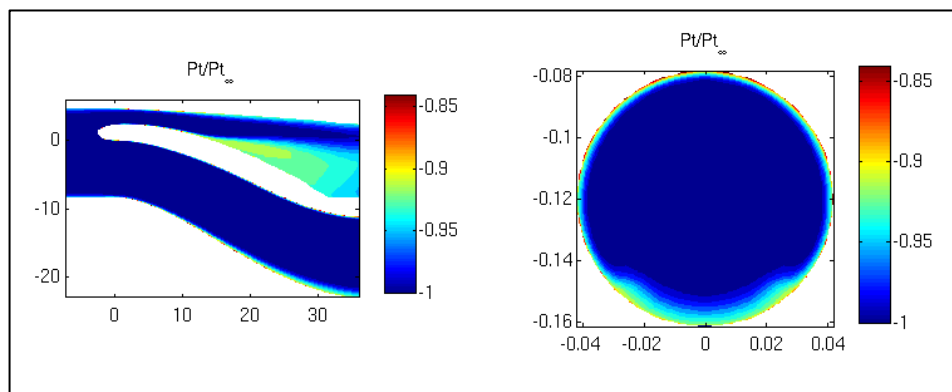


Figure 2.7 – Pressure Losses with Flat Plate Design (Courtesy UTRC)

The second design tested placed the inlet at the fifty percent chord location of a National Advisory Committee for Aeronautics (NACA) airfoil. The airfoil chosen was from the NACA 65(10)16 series, which was placed inside a conical inlet area as shown in Figure 2.8. This design also resulted in a boundary layer thickness of less than ten percent, similar to the flat plate design. Fabrication of the conical piece around the NACA airfoil plate would have been challenging, giving another reason why this design was not chosen.

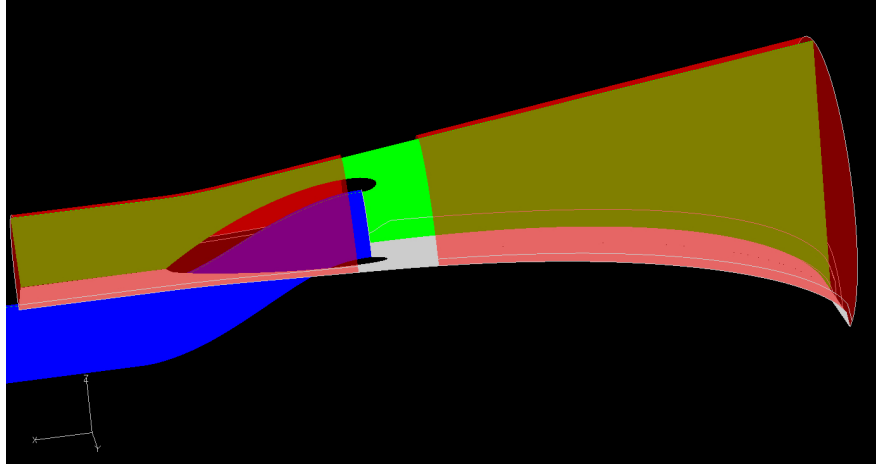


Figure 2.8 – NACA Airfoil Inlet Design (Courtesy UTRC)

The third major design idea involved placing a variable height flow ramp inside of a semi-circular entrance duct. The concept was to accelerate the flow to a higher Mach number where the area was a minimum at the top of the ramp, and then allow the flow to decelerate following the ramp, causing a boundary layer to grow along the diffusing surface. A CFD model illustrating the concept is shown in Figure 2.9.

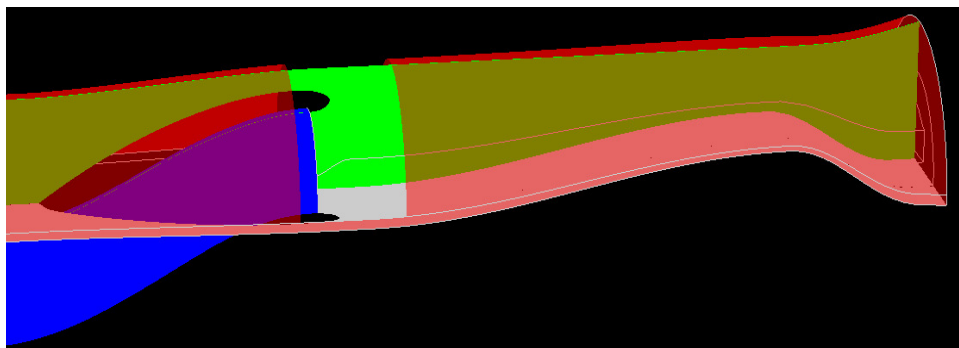


Figure 2.9 – CFD Model of Inlet Ramp (Courtesy UTRC)

The first iteration on this design used a ramp with a height of four inches. This resulted in a boundary layer thickness of twenty-one percent, less than desired, but much closer to the thirty percent boundary layer desired. It also resulted in more realistic

distortions at the AIP of the serpentine inlet. Figure 2.10 below shows the predicted pressure losses through the inlet and at the AIP.

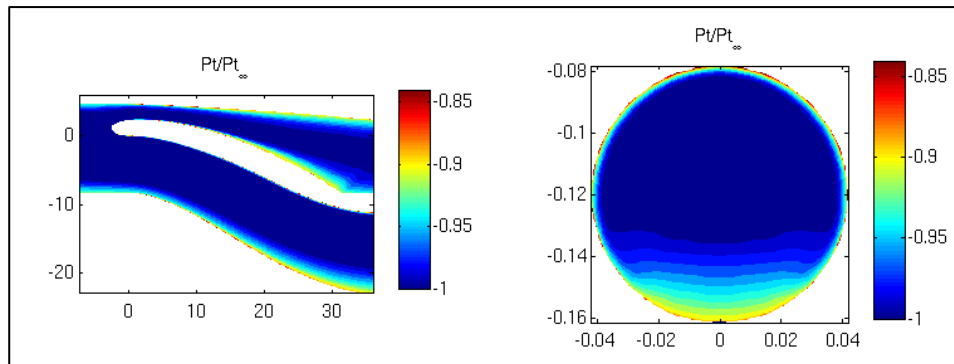


Figure 2.10 – Pressure Losses with 4” Ramp Design (Courtesy UTRC)

The second iteration of the ramp inside a semi-circular duct used a bump with a maximum height at its peak of 5.5 inches. The predicted boundary layer thickness for this design was between twenty-nine and thirty-one percent, depending on the mass flow through the serpentine inlet. A mass flow of thirty-four pounds-mass per second resulted in a 29.5 percent boundary layer profile, while a mass flow of thirty-six pounds-mass per second gave a boundary layer profile at the inlet face of 30.5 percent. The total pressure losses through the inlet and at the AIP associated with the 5.5 inch ramp is shown below in Figure 2.11.

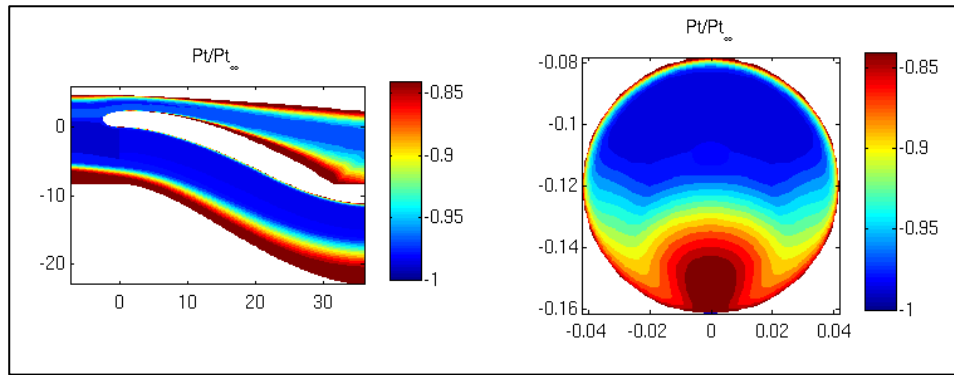


Figure 2.11 – Pressure Losses with 5.5” Ramp Design (Courtesy UTRC)

An examination of the Mach number contour plot for the 5.5 inch ramp with the larger mass flow revealed the presence of locally transonic and supersonic flow around the lip of the inlet in the bypass duct, as shown below in Figure 2.12.

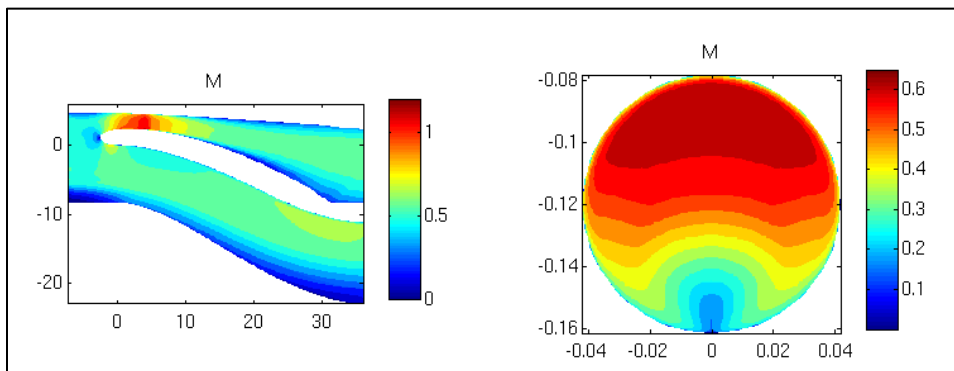


Figure 2.12 – Local Mach Numbers around Inlet and at AIP (Courtesy UTRC)

The possible presence of supersonic flow through the bypass duct raised a concern about the resulting local low static pressures that resulted. These static pressures would cause local high forces on the wind tunnel components, and raised concerns for possible structural failure either in the serpentine inlet or in the walls and supports making up the outer part of the flow path. To help strengthen the inlet, it was covered in several layers of polyurethane coating as described previously. To ensure the structural

strength of the outer walls of the wind tunnel, a complex FEA simulation was performed. The details of the structural analysis are covered in a later section. As Figure 2.13 shows below, the two main regions of concern are located at the maximum height of the ramp and around the lip of the serpentine inlet. The speed of the flow at these two locations is predicted to approach supersonic velocity.

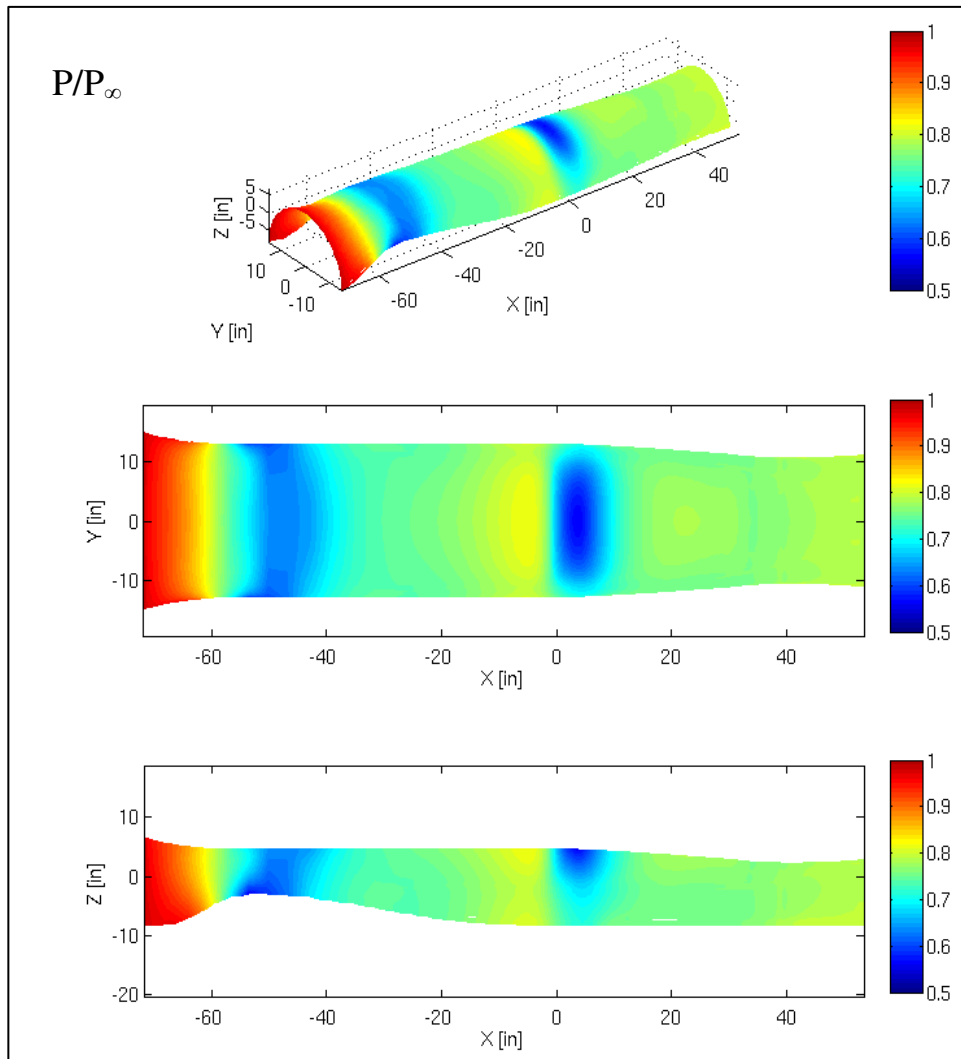


Figure 2.13 – Static Pressures throughout Experimental Facility (Courtesy UTRC)

A summary of the different boundary layer profiles associated with each design is shown below in Figure 2.14. It shows that placing a ramp inside a semi-circular duct

generates a boundary layer that best approximates the boundary layer seen in the NASA experiment. The four inch ramp height profile is close to the NASA profile for the first twenty percent of the inlet throat height, but becomes fully developed too quickly. In contrast, the 5.5 inch ramp height profile does not follow the NASA profile as close in the bottom part of the throat, but becomes fully developed at approximately the same point. Since achieving an inlet boundary layer profile that becomes fully developed at thirty percent of the inlet throat height was most important, the design with the 5.5 inch ramp height was chosen for construction.

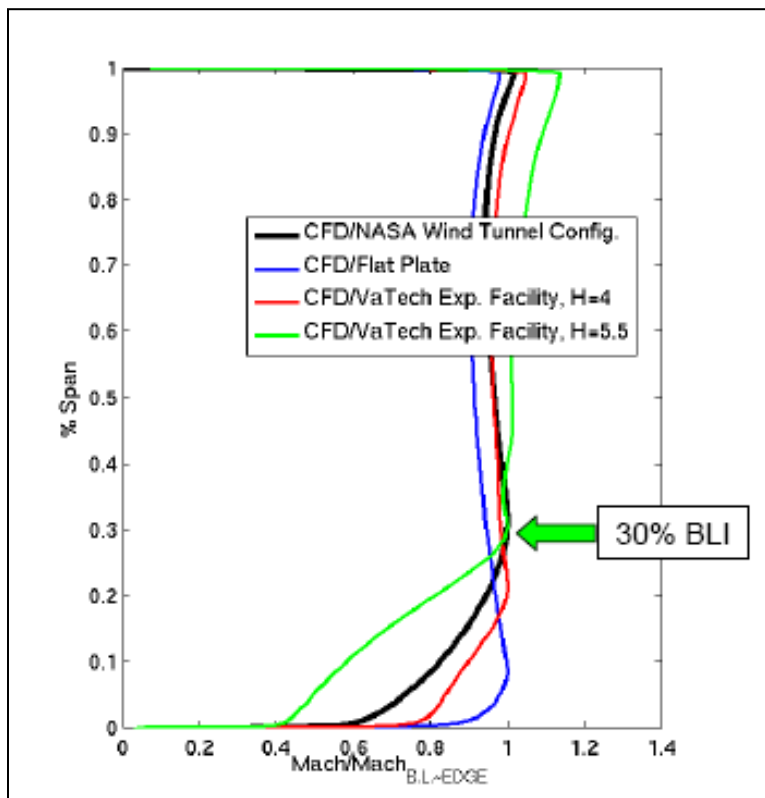


Figure 2.14 – Summary of Boundary Layer Profiles (Courtesy UTRC)

In addition to the flow in front of the serpentine inlet, one other concern was addressed through the CFD simulations. This problem involved the separation of the

flow in the bypass duct along the upper surface of the serpentine inlet. The first CFD simulations were run with a constant semi-circular cross-sectional area in the bypass duct, similar to what was seen in front of the serpentine inlet. These simulations revealed the presence of some flow separation due to the large changes in area behind the inlet. The problems associated with this flow separation were propagating upstream, altering the flow across the front face of the inlet. To prevent this flow separation in the bypass duct, the profile of the outer wall had to be changed. As can be seen below in Figure 2.15, the wall in the bypass duct was changed from a constant diameter to a nozzle design that was both convergent and divergent. The convergent part of the bypass wall produced an expanding flow without separation. The divergent part then decelerated the flow, increasing the air pressure and reducing the flow velocity to better match the engine inlet requirements.

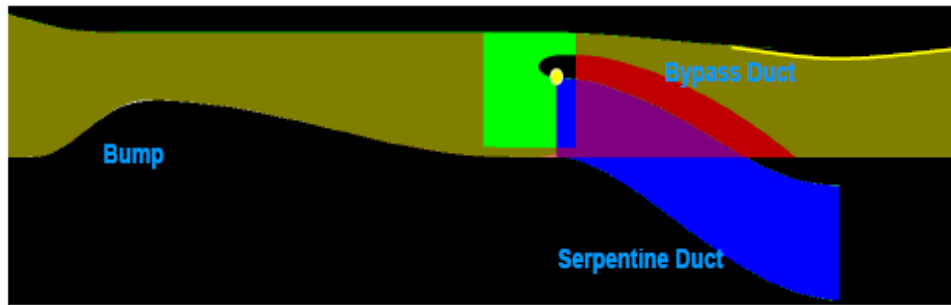


Figure 2.15 – CFD Model showing Revised Bypass Duct Profile (Courtesy UTRC)

2.3.2 Detailed Description of Experimental Facility

Following the CFD-produced internal flow path of the air, a three-dimensional (3D), full-scale CAD model was generated to aid in the engineering design of a structure that could create and support the flow path needed. Two different 3D modeling programs

were used for this task, AutoCAD and Unigraphics NX5. The CAD model was needed to specify sizes, types of connections to be made, and to aid in visualizing the overall layout of the facility. It also allowed fabrication drawings of the individual pieces to be created quickly, speeding up construction time. Figure 2.16 below shows a side CAD view of the overall experimental facility. Drawings showing sectioned views of the air flow through the facility at different axial locations are provided in Appendix D.

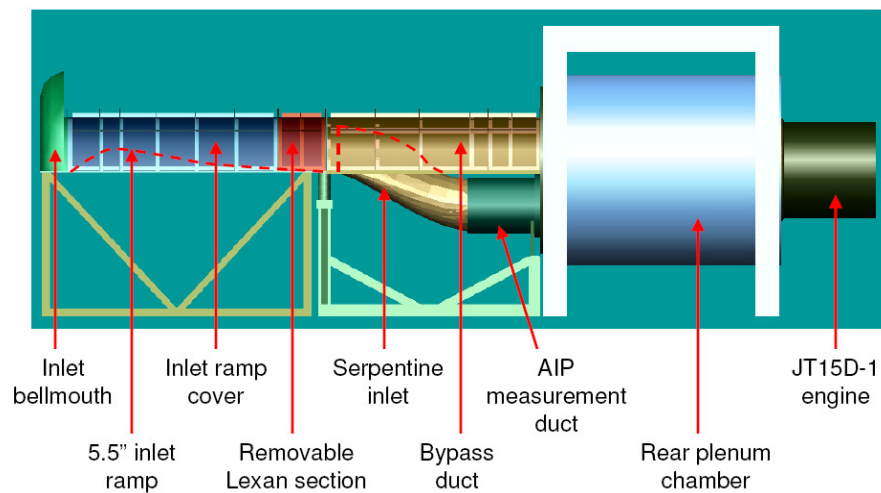


Figure 2.16 – Overall CAD Model of Experimental Facility

Each piece of the experimental facility was created in the 3D CAD model and positioned in its correct location, as shown in the figure. The first part of the model created was the serpentine inlet, which then served as a reference point for all other pieces. Since the inlet was designed to be a flush-mounted BLI inlet, a base plate was created for through which the inlet was passed. At the AIP (discharge) of the inlet, a one-half inch deep circular notch was cut into the duct. This notch accommodated a steel pipe that was used to connect the serpentine inlet to the rear plenum. Figure 2.17 below shows the serpentine inlet passing through the base plate with the steel pipe attached to the discharge area.



Figure 2.17 – Serpentine Inlet with Base Plate and Mating Pipe

The rear plenum served as a sealed chamber where the air exiting the serpentine inlet and bypass duct could further diffuse. This diffusion and resulting pressure recovery played an important role in maintaining safe operation of the jet engine during testing. A large decrease in air pressure in front of the engine inlet could result in the engine stalling or surging and possible damage to the engine. The plenum is shown below in Figure 2.18 with the rear cover plate and base plate attached.



Figure 2.18 – Rear Plenum Chamber

Inside of the rear plenum, an inlet control device (ICD) was attached to the front of the engine inlet. The ICD served two major purposes in the experiment. The first was to remove any swirl and to reduce the scale of the turbulence in the flow so the engine received clean, non-distorted airflow. The second was to serve as a foreign object debris (FOD) screen, preventing any loose pieces of material from being ingested through the engine. The ICD accomplished these two functions with a metal honeycomb mesh around an inner supporting frame. The mesh was fine enough to stop foreign objects from passing through, but was coarse enough to not significantly restrict the airflow to the engine. Figure 2.19 below shows the ICD mounted inside the rear plenum.

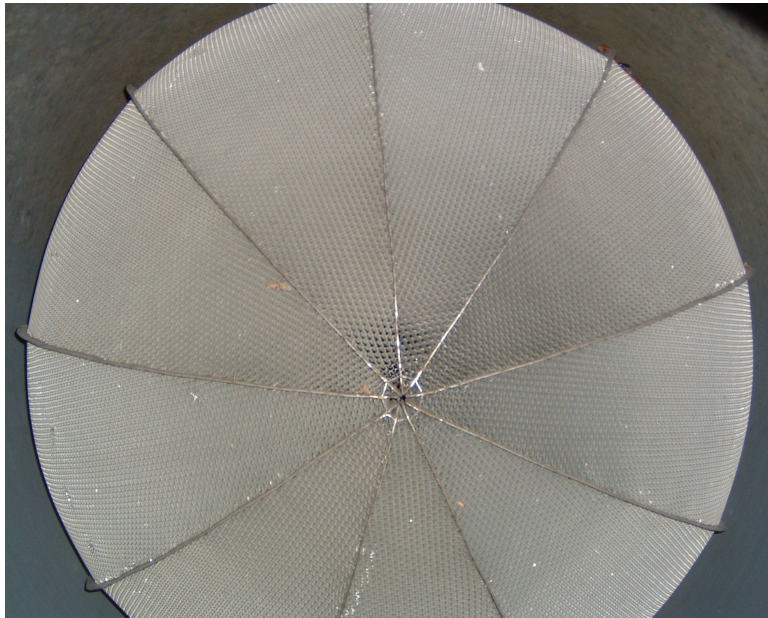


Figure 2.19 – Inlet Control Device inside Rear Plenum

Flow into the plenum occurred through two openings, one from the serpentine inlet and one from the bypass duct. A wind tunnel-plenum junction plate was attached to the front of the rear plenum, and two holes were cut into this plate. The upper hole

allowed the tunnel bypass flow to exit into the plenum, while the lower hole provided for flow through the serpentine inlet into the plenum. This rear plate also served as a mount for the steel pipe connected to the AIP of the serpentine inlet. Figure 2.20 below shows the junction plate attached to the rear plenum using four clamps and two positioning tabs on the bottom.

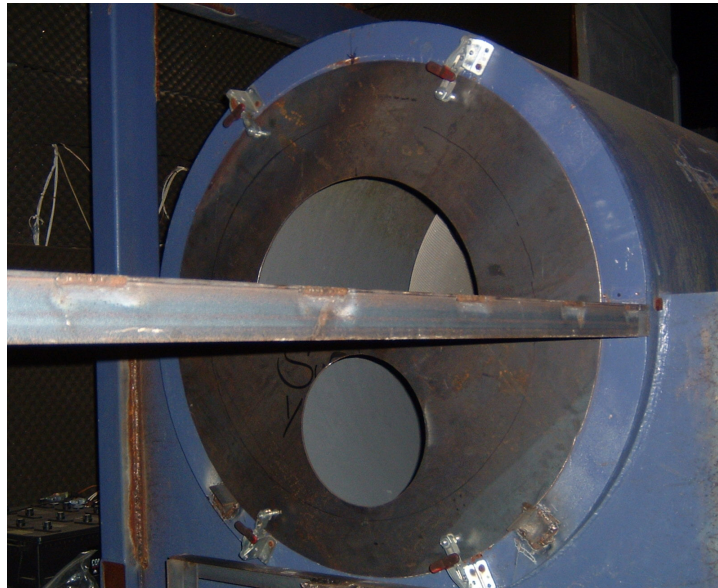


Figure 2.20 – Wind Tunnel-Plenum Junction Plate

Aluminum plates were machined to place over the upper opening in Figure 2.20 to control the mass flow ratios between the bypass duct and serpentine inlet. These blockage plates allowed the boundary layer for different engine speeds to be controlled by using different size blockages. The plates had a uniform outer diameter, but varying inner diameters that blocked a different percentage of the open area. These plates were positioned behind the bypass duct but in front of the junction plate, making interchanging plates fast and easy. A CAD drawing showing a blockage plate installed in front of the bypass duct opening is given below in Figure 2.21.

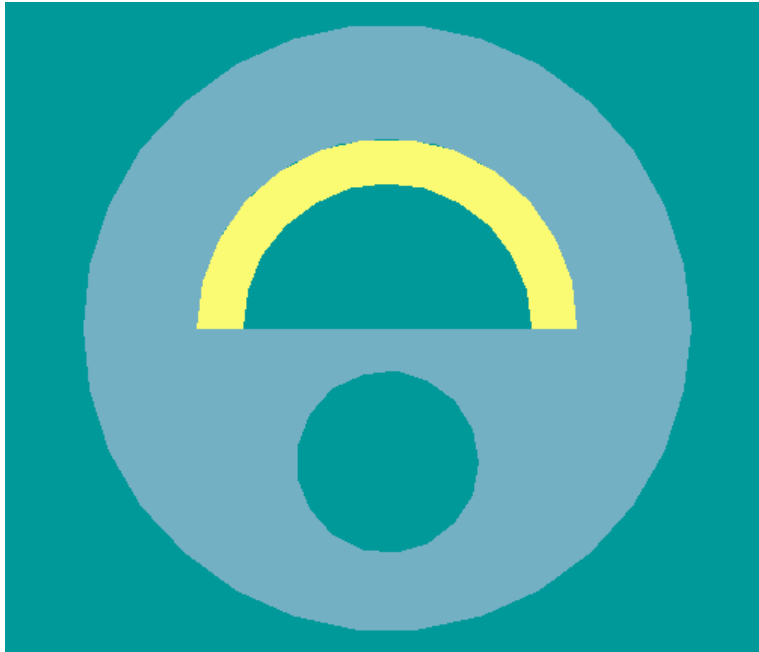


Figure 2.21 – Bypass Duct Blockage Plate

The bypass duct contained a complex curvature that was difficult to fabricate. First, seven circumferential supports were made using 1/8"x1/8"x1" aluminum angle. Notches were cut in the aluminum angle allowing the supports to be curved to shape. Extra supports were placed around the throat location toward the back of the duct and at the front of the duct where the serpentine inlet lip was located because of the large pressure losses expected in these regions. The aluminum skin was then riveted to the circumferential supports in five sections. The skin had to be cut into sections to attach it without wrinkling and distortion. The aluminum used for the skin was a 6061 alloy that was thirty-two thousandths of an inch thick. Five longerons made of 6061 aluminum angle were then fabricated and riveted to the aluminum skin to provide extra stiffening. The longerons were attached at angles of zero degrees, forty-five degrees, ninety degrees, one hundred thirty-five degrees, and one hundred eighty degrees. These longerons can be

seen running longitudinally along the duct. The finished structure is shown below in Figure 2.22.



Figure 2.22 – Outer Structure of Bypass Duct

In front of the bypass duct was a twelve-inch removable section of Lexan. The transparent Lexan allowed the internal components of the experiment to be observed during engine operation. The Lexan used was ninety thousandths of an inch thick, and had the same circumferential supports as the bypass duct. Only three longerons were necessary to stiffen the Lexan since it had a length of only twelve inches; one at zero degrees, one at ninety degrees, and one at one hundred eighty degrees. This piece of Lexan was designed to be removable if necessary for later experiments so that an adjustable flow control “collar” can be installed in its place. This collar will help control the pitch and yaw angles entering the serpentine inlet, and also serve to control the mass flow through the bypass duct. Figure 2.23 below shows the removable Lexan section.

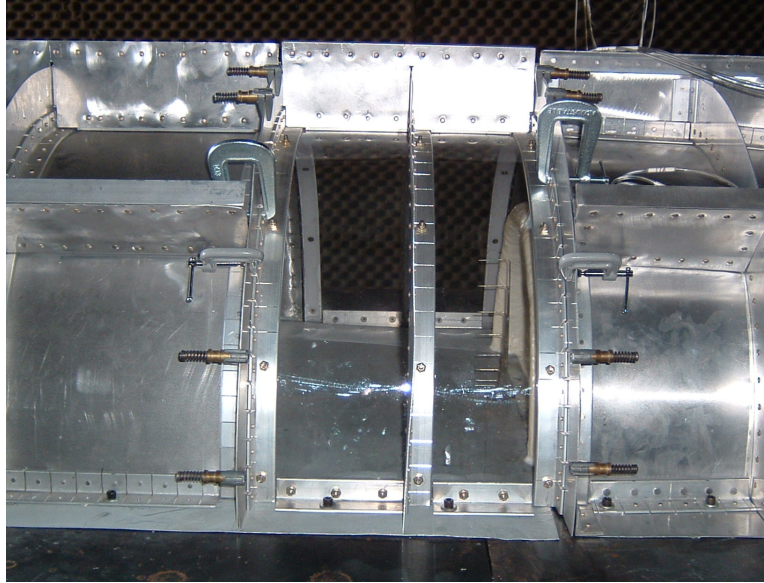


Figure 2.23 – Removable Section of Lexan

Forward of the Lexan section was the 5.5 inch ramp needed to generate the boundary layer profile, and a cover over the ramp to guide the air through the duct. The ramp design and fabrication technique was based on the structure used to construct the wings of airplanes. The inner support structure had two struts running the length of the ramp axially, and two stiffeners running horizontally between the two struts. An aluminum skin thirty-two thousandths of an inch thick was then riveted to the inner supports, completing the ramp. The aluminum skin was cut so that the ramp could slide inside the duct cover, but with a close fit of the edges close to the inner duct wall so the gap could be sealed, preventing air leakage during operation. Figure 2.24 below shows the completed ramp.

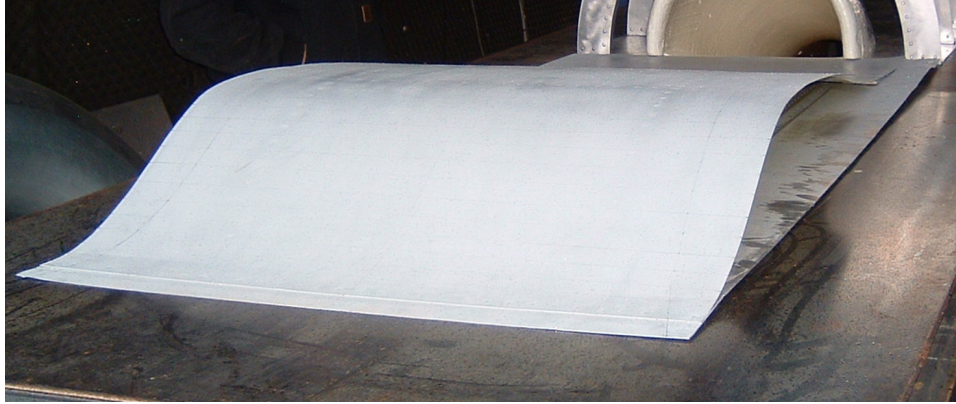


Figure 2.24 – 5.5 inch Inlet Boundary Layer Generation Ramp

The cover duct over the ramp was fabricated in a similar manner to the bypass duct cover. Seven circumferential supports made of the same 6061 aluminum angle were cut to length and notched, forming the outer support structure for the duct. These supports were also positioned at locations where the maximum pressure differentials were expected as predicted by the CFD static pressure plot. One location of especially large pressure losses was at the maximum height of the inlet ramp. CFD predicted low pressure with locally transonic and possibly supersonic flow in this region, indicating the need for extra supports. Five sets of longerons were included to provide extra stiffness to the aluminum skin between supports. These longerons were once again located every forty-five degrees circumferentially, as was done on the bypass duct structure. The inlet ramp cover is shown below in Figure 2.25.



Figure 2.25 – Outer Structure of Inlet Ramp Cover

An inlet bellmouth was designed for the front of the experimental facility connected to the inlet ramp cover frame. This bellmouth was used to smooth the air flow entering the front of the experiment, preventing any flow separation that could distort the boundary layer profile. The bellmouth was designed based on standards included in the American Society of Mechanical Engineers (ASME) Flow Measurement Engineering Handbook (Flow Measurement Engineering Handbook Third Edition, 1996). The design was based on the ISA 1932 nozzle, which has a double-radius contoured inlet. Figure 2.26 below shows the bellmouth in place at the front of the experimental facility.



Figure 2.26 – Bellmouth on Front of Experimental Facility

The figure above also shows two threaded rods attached to the bottom of the plate supporting the bellmouth. These rods and bolts allowed the angle of the plate supporting the inlet ramp and cover to be adjusted, ensuring the experiment was level. A similar threaded connection was used for the base plate supporting the bypass duct and serpentine inlet. Two other parts of the experimental set-up were contained inside the bypass duct and were important in helping keep the serpentine inlet in place during testing. The first was an aluminum strap placed around the outer surface of the inlet, which prevented the inlet from lifting up or moving when subjected to the horizontal and vertical forces created when turning the air inside the inlet. The second was a flat metal plate that extended from the back of the inlet ramp to the inside of the throat of the serpentine inlet by two inches. This flat plate created a smooth surface for the air to flow into the inlet, and also helped secure the lower part of the reinforced EPS duct. This metal plate prevented the serpentine inlet from deforming during high speed tests.

Once all parts of the experimental facility were in place, the air gaps between pieces were sealed using either silicone or an expanding spray-on insulation. Silicone

was used for the small gaps and where keeping a smooth profile was important in preventing disruption of the flow, such as between the inlet ramp and its cover. The spray-on insulation was used for larger gaps where maintaining a smooth flow was not as important, such as sealing between the serpentine inlet and base plate. Since the Lexan piece was a removable section, it was sealed using a rubber gasket that fitted over the stiffeners between the inlet ramp cover, the Lexan piece, and the bypass duct cover. This rubber gasket was then held in place using a combination of cleko clamps and c-clamps. The completed experimental facility is shown below in Figure 2.27.

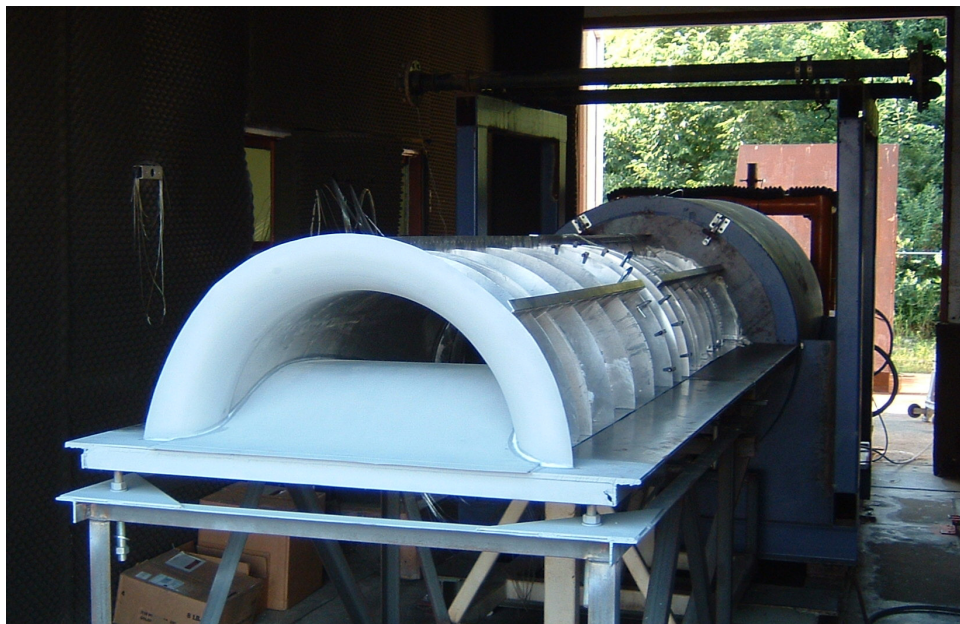


Figure 2.27 – Completed Experimental Facility

2.3.3 Structural Analysis of Experimental Facility

To ensure the structural strength of the experimental facility, an FEA simulation was performed on the upper structure made up of the inlet ramp cover, removable Lexan section, and bypass duct cover. The need for this analysis was confirmed when

examining the large static pressure losses in the facility predicted by the CFD simulations. A failure of the experimental facility would affect not only the experiment being conducted, but could also lead to significant damage of the jet engine being used to create suction through the wind tunnel. This potential for failure and resulting damage led to the decision to complete the structural analysis described below to ensure the experimental facility could withstand any forces or pressures it might see.

The finite element analysis was completed using the commercial software package ANSYS in conjunction with the 3D CAD modeling software Unigraphics NX5. The first step in the analysis was to create a CAD model of only the pieces being analyzed. This CAD model was then meshed using a four-node, 3D tetrahedral element type. One important factor when creating the mesh was to make sure the elements were connected where the circumferential supports and aluminum skin were riveted together. This was done by examining the mesh to see if any nodes were connected to only one element. Figure 2.28 below shows a proper mesh where the nodes on the aluminum match the nodes on the circumferential supports. This assures correct load transfer between support and skin.

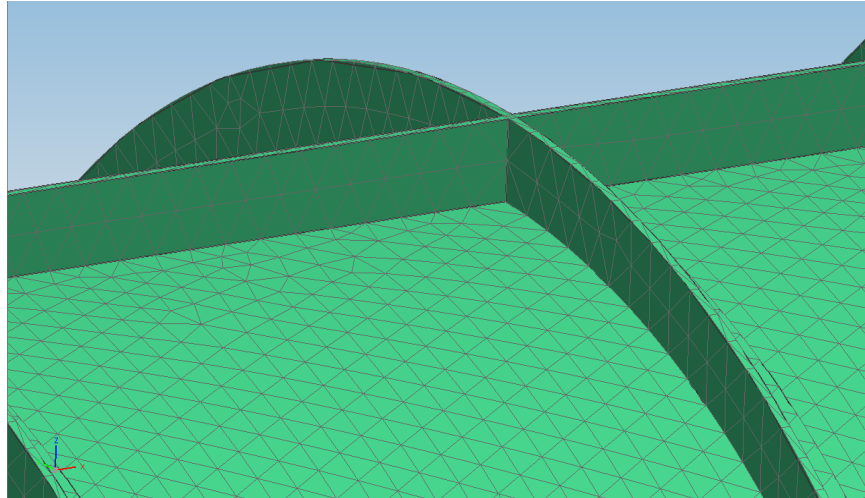


Figure 2.28 – Mesh Between Circumferential Supports and Aluminum Skin

Once the model was meshed, material properties were applied to the supports and skin. All pieces analyzed were made of Aluminum 6061. A summary of the material properties used in the analysis are provided in Appendix B. The skin for the entire structure is thirty-two thousandths of an inch thick, while the circumferential supports are all made of 1/8"x1/8"x1" aluminum angle. Once the material properties were applied, the loads and constraints were applied to the model. Since the structure was bolted to the supporting base plates, a fixed boundary condition was applied to the two longerons located on the bottom of the structure at zero degrees and one hundred eighty degrees. This boundary condition prevented translational and rotational motion of the bottom two longerons. When specifying the loads acting on the structure, a normal pressure of 13.7 pounds per square inch (psi) acting toward the center of curvature was applied on all surfaces. This pressure was used because it represented a worst-case scenario for the experimental facility. Since the experimental facility was located at an elevation of 2,200 feet above sea level, atmospheric pressure at that elevation was approximately 13.7 psi. If the jet engine created a vacuum inside the sealed structure at any point, the maximum

resulting external pressure would be 13.7 psi. Although the CFD predicted a maximum static pressure loss of only seven psi during its maximum level of operation, running the analysis with twice the expected pressure loss at any point created an additional factor of safety. Figure 2.29 below shows the final loads and constraints applied to the assembled three-piece model.

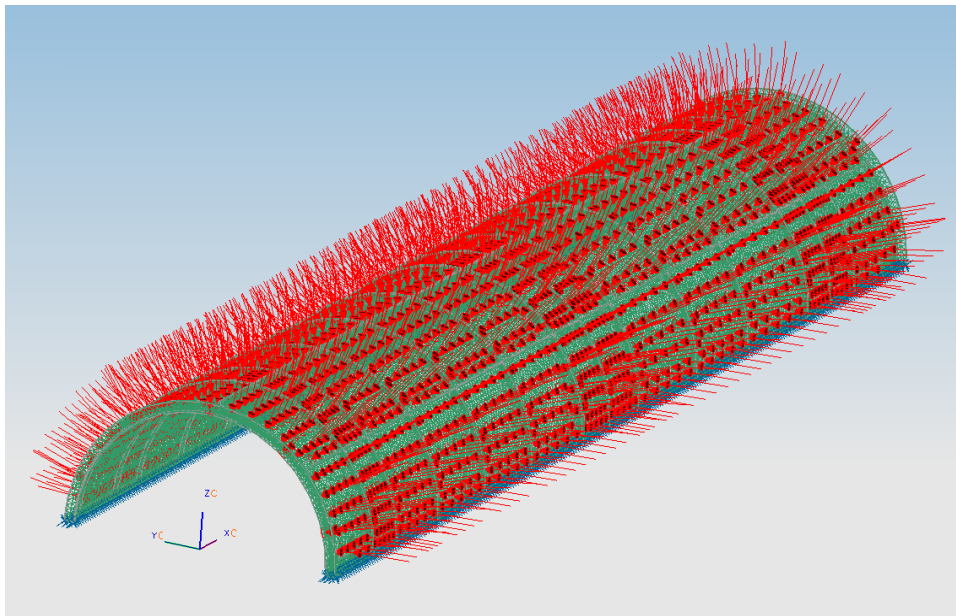


Figure 2.29 – FEA Model with Loads and Constraints Applied

Once all loads and constraints were applied, the first part of the structural analysis was run. This part of the analysis focused on the maximum stresses and deflections that occurred and the resulting factor of safety. The stress analysis resulted in a maximum local stress of 6,092 psi, which occurred in the long unsupported regions of the bypass duct. Since the aluminum used in the structure has a yield strength of 35,000 psi, this gave a factor of safety of 5.75. Figure 2.30 below shows the resulting stresses on the assembly, while the scale on the left side of the figure is in units of psi.

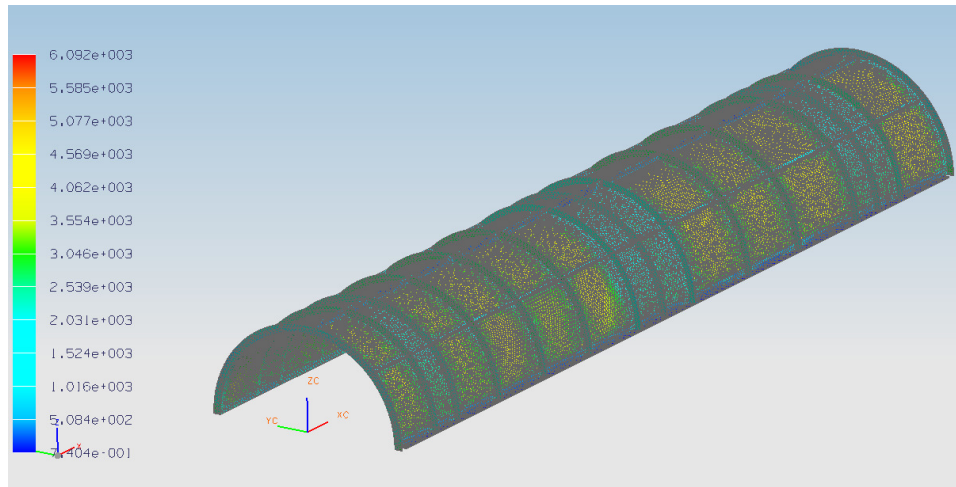


Figure 2.30 – Resulting Stresses in Experimental Facility

In addition to the stresses, the displacements were also examined as part of the analysis. The maximum displacement predicted for the assembly was 0.00902 inches. The resulting deflections are shown below in Figure 2.31, with the scale on the left being shown in units of inches.

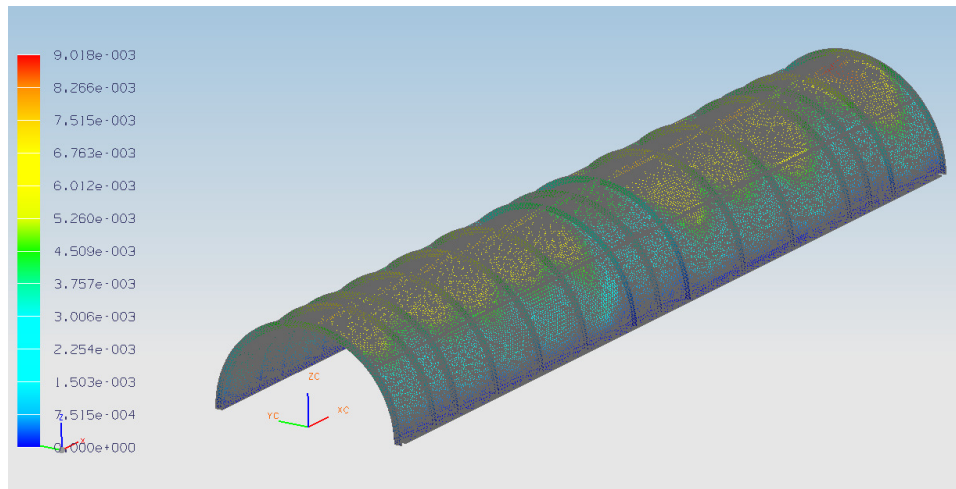


Figure 2.31 – Resulting Displacements in Experimental Facility

In addition to the traditional stress analysis, a buckling analysis was also performed because of the possibility of the aluminum skin failing in the unsupported

regions. The buckling analysis was a more advanced simulation that considered the possibility of failure in a different manner under the same loading conditions. The point of the analysis was to find the load that would cause the structure to bypass its bifurcation point where it was still in a state of stable equilibrium, and into a state of failure.

Buckling failure often occurs suddenly and dramatically with little or no warning, resulting in a special set of design conditions that must be followed (Hibbeler, 2000). A Lanczos linear buckling analysis was performed to determine where the experimental facility was predicted to fail. As Figure 2.32 shows, failure was not expected to occur until the back half of the bypass duct reached a displacement of 1.128 inches. Since the maximum expected deflection of the duct determine in the first part of the stress analysis was 0.00902 inches, it was not anticipated that the structure would fail due to buckling.

The units for the scale in the figure below are in inches.

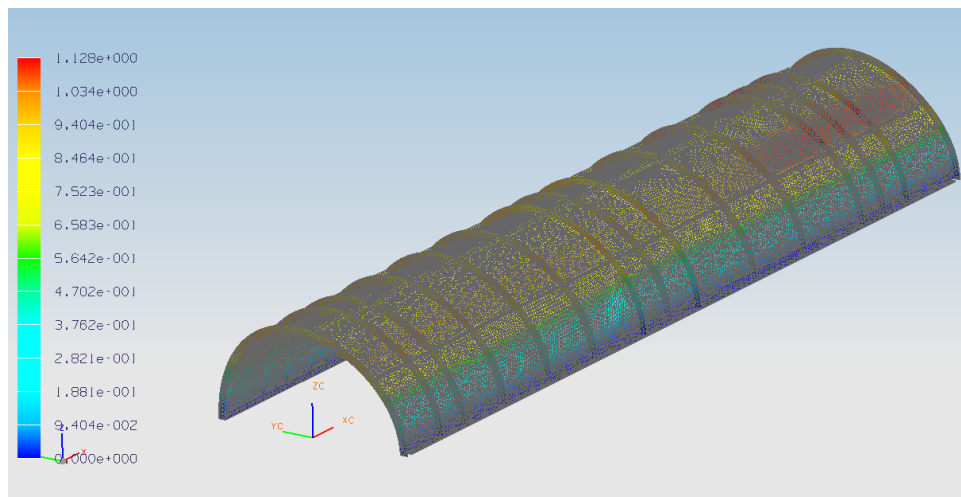


Figure 2.32 – Resulting Displacements Associated with Buckling Failure

The last part of the structural analysis performed was a test to determine if the rivets would pull through the aluminum skin and structural support when subjected to a

vacuum of 13.7 psi. Figure 2.33 below shows a test coupon with three types of rivets that were tested. The National Aerospace Standard 1097 rivets were used for all inside surfaces of the wind tunnel duct because they could be countersunk and mounted flush with the inner surface. The Mil Spec. 20426 rivets could also be countersunk and mounted flush with the inner surface, but they required larger holes and countersinks because of the larger rivet head size. They were not used during construction because the larger holes would weaken the aluminum skin more than the smaller holes. The Mil Spec. 20470 large cap rivets were only used for external connections during construction because of the protruding rivet head. Figure 2.34 shows the back side of the rivets tested and how the aluminum skin is attached to the supports and longerons. The test was performed by placing a rubber boot over the heads of the rivets and hooking the rubber boot into a vacuum pump. The vacuum pump was then used to reduce the pressure inside the boot to a vacuum, subjecting the rivets to a 13.7 psi pressure trying to push the rivets through the supports. No rivets were pulled through the support, and no deformation or change along the surface was observed.

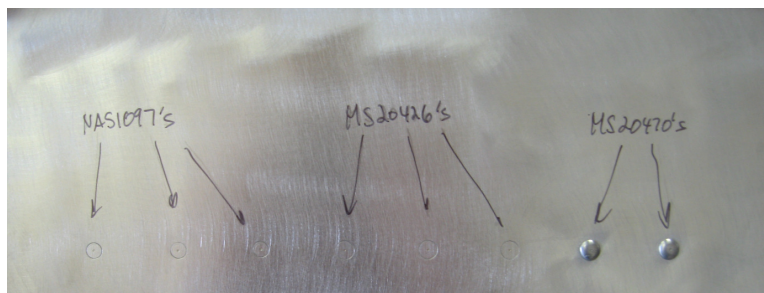


Figure 2.33 – Internal View of Rivet Construction Technique



Figure 2.34 – External View of Rivet Construction Technique

2.4 Instrumentation

The design of the instrumentation for this facility was based on the need to characterize the flow both at the inlet-throat and at the AIP of the serpentine inlet. This was done using a combination of sixty-four static and total pressure measurements. The design of the individual probes was based on the United Sensor modified Prandtl design where the horizontal length of the probe was at least fourteen times the diameter of the tube. The long horizontal portion of tube made the probe less sensitive to variations in Mach number (www.unitedsensorcorp.com/). To understand the flow at the inlet throat, a boundary layer rake was installed along with one static pressure probe. The boundary layer rake consisted of ten total pressure probes, and was positioned in the middle of the inlet throat facing directly upstream into the flow. This rake was used to determine the boundary layer profile entering the serpentine inlet. Table 2.1 below specifies the vertical locations of the total pressure probes assuming zero to be the bottom of the serpentine inlet throat. Figure 2.35 shows the boundary layer probe installed in the experiment. Because of the long cantilevered design of the boundary layer rake, initial tests revealed that the rake developed a horizontal vibration at higher engine speeds. This problem was solved by encasing the probe rake in an aerodynamic support strut.

Table 2.1 – Location of Probes on Boundary Layer Rake

Probe	Vertical Location (inches)
1	0.100
2	0.210
3	0.420
4	0.756
5	1.285
6	2.056
7	3.084
8	4.318
9	5.614
10	6.961



Figure 2.35 – Boundary Layer Rake Installed in Center of Inlet

To measure the flow velocities entering the bypass duct, three sets of rakes each containing three total pressure probes were installed. These rakes were positioned at circumferential locations of forty-five degrees, ninety degrees, and one hundred thirty-five degrees. Table 2.2 below lists the radial locations for the probes, while Figure 2.36 shows the rakes installed in the bypass duct. Each rake contains one probe at each radial location.

Table 2.2 – Radial Locations of Bypass Duct Probes

Probe	Radial Distance (inches)
1	10.875
2	11.688
3	12.500



Figure 2.36 – Bypass Duct Rakes Installed

To help determine what is happening to the flow inside the serpentine inlet, a series of static pressure taps were installed. A set of four probes were installed at two different axial locations along the inlet. The axial locations were twelve inches from the front of the inlet and twenty-four inches from the front of the inlet. This divided the inlet into three equal sections. The four taps at each location were positioned at ninety degree increments; one probe on the top of the inlet, one probe on the right side of the inlet, one probe on the left side of the inlet, and one probe on the bottom of the inlet. All static pressure taps were mounted flush with the inner surface of the inlet. Figure 2.37 shows the static pressure taps on three sides. There are also two taps on the far side of the inlet that are blocked from view.

Local velocities and Mach numbers were calculated for each of the probe measurements based on the static pressure measured at the base of the probe. While the use of pitot-static probes at each measurement location would have been desirable for higher accuracy, it was not practical. Reference to the CFD predictions showed that the static pressure remained relatively constant at the wall value for each of the probe locations.

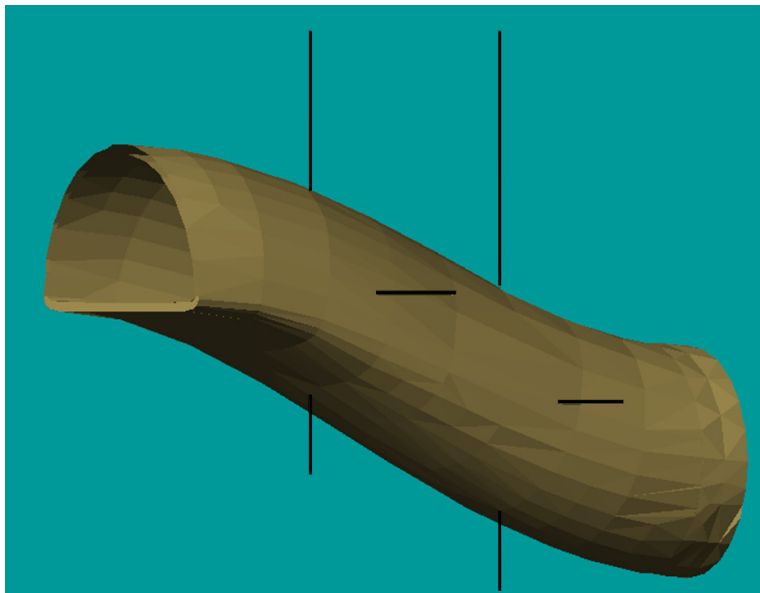


Figure 2.37 – Static Pressure Taps in Serpentine Inlet

To help monitor the experimental facility during operation, a series of static pressure taps were installed at key locations where large pressure losses were expected. Referring to Figure 2.38, the key locations were at the maximum height of the inlet ramp (1), at the base of the boundary layer rake going into the serpentine inlet (2), at the base of the bypass probe rake going into the bypass duct (3), in the rear plenum (4), and in the JT15D-1 fan casing (5). Special care was taken to ensure that the ends of the static pressure taps were flush with the inner surfaces where they were mounted. The static

pressure taps at the base of the boundary layer and bypass probe rakes were also used to perform the calculations needed to determine the Mach numbers at these locations.

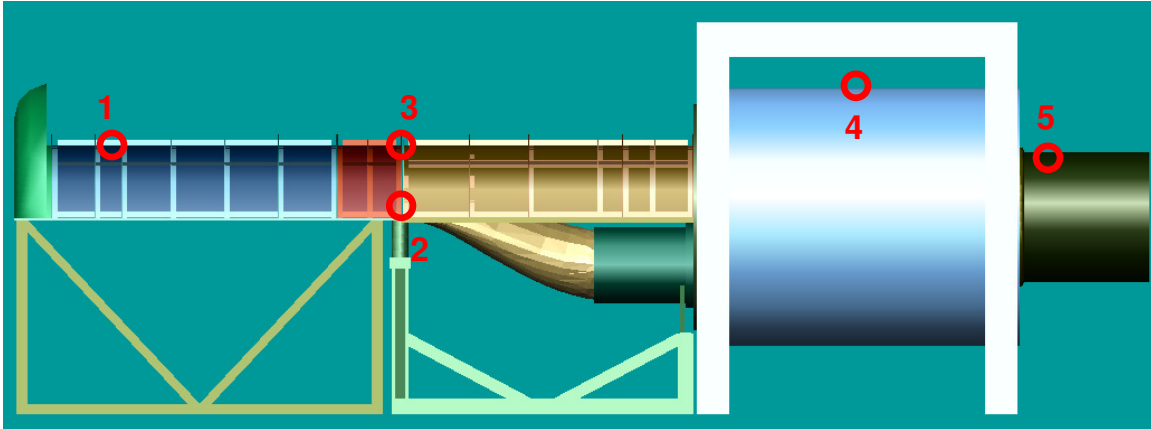


Figure 2.38 – Static Pressure Taps in Experimental Facility

The measurements at the AIP of the serpentine inlet consisted of thirty-two total pressure measurements. The locations of these pressure measurements were based on recommendations specified by the Society of Automotive Engineers (SAE) in their Aerospace Recommended Practice (ARP) Report 1420 (SAE ARP 1420). This report states that probes should be located at the centroids of equal area rings. For the initial experiments reported here, the design for the AIP rake used four arms spaced every forty-five degrees circumferentially for a total of eight arms. Each of these arms contained four probes positioned at the area centroids according to SAE ARP 1420. Table 2.3 below gives the radial locations for each probe, while Figure 2.39 shows the resulting AIP rake installed in the experiment. The rake seen below allowed the circumferential and radial distortions to be quantified as will be described later.

Table 2.3 – Radial Locations of Probes on AIP Rake

Probe	Radial Location (inches)
1	2.121
2	3.674
3	4.743
4	5.612

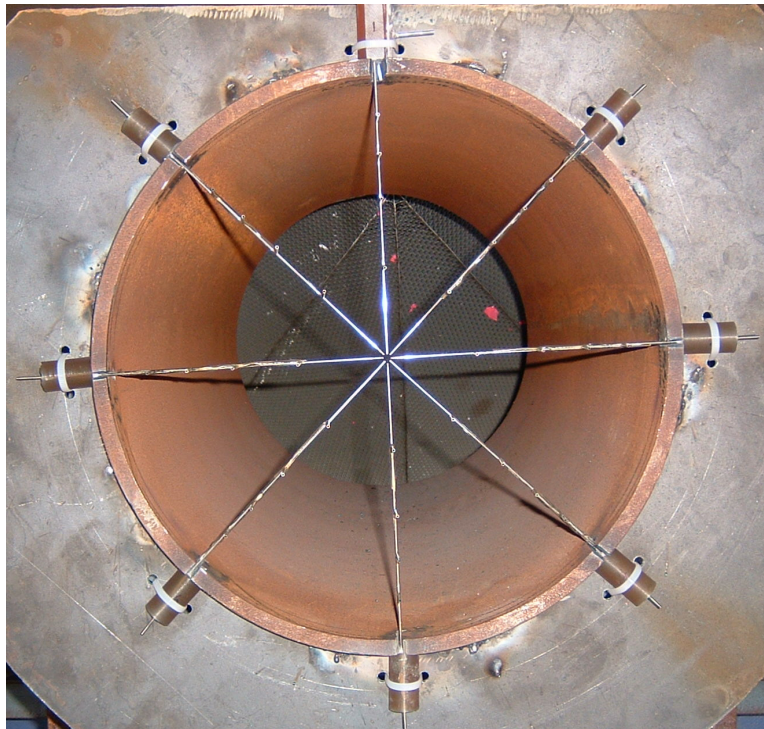


Figure 2.39 – AIP Rake Installed

Standard procedures were established and followed when collecting data during testing. The engine was brought to the desired speed and allowed to run unchanged for three minutes to assure only steady-state data was collected. At the end of the three minutes, data were collected for thirty seconds at a frequency of ten hertz. The data collection frequency accommodated the long time constants of the long pressure measurement tubular connections. This resulted in a total of three hundred data points

being collected for each pressure measurement location. These three hundred data points were then averaged for each measurement to obtain one final average value that was used in calculations. Data were collected using a PSI System 8400 and a miniature electronic pressure scanner that could record thirty-two pressure measurements simultaneously. The transducer contained in the pressure scanner had a range of zero to fifteen psi. The system was calibrated using a deadweight tester to ensure the pressure measurements were accurate. Since only thirty-two measurements could be collected at a time, the pressure tubes collecting the measurements had to be interchanged at each engine speed. Humidity was also a concern during testing since it could lead to condensation forming in the tubes collecting the pressure measurements. For the tests performed here, the humidity never exceeded 57%, and no condensation was formed inside the tubes. A test log was kept which monitored the ambient temperature, pressure, humidity, and engine speed associated with each set of data collected.

2.5 Test Procedure

An additional standard procedure was followed when running the experimental facility to ensure that no damage was done either to the experiment or the jet engine. Each test began by starting the jet engine and increasing its speed to 50%, which corresponded to its idle speed. A leak check was then performed both on the engine and the experimental facility to ensure that no air was being drawn in from undesired locations. Once this was done, the engine was left at its idle speed for three minutes so that a set of data could be collected. This data was then immediately processed to check the static pressures at the five key locations mentioned earlier. If no large static pressure

losses were seen, the engine was then increased to 55% speed, where it was left for another three minutes for a set of data to be collected. The static pressures were again processed immediately, and if all pressures were satisfactory, a full set of data was collected including boundary layer and AIP data. The engine was then increased in ten percent increments, and the process repeated until all data were collected. The static pressure loss in the fan casing was used as the primary indication of facility stability. A pressure loss greater than two psi below atmospheric pressure was established as unacceptable and the engine would be shut down if this threshold were reached. Large pressure losses in the fan casing would result in the fan stalling, which needed to be avoided. Because of proprietary restrictions, a fan map could not be obtained for the JT15D-1, which would have helped determine the operating point during testing, further ensuring the safety of the engine. All testing was performed in a test cell at the Gas Turbine Laboratory located on-site at the Virginia Tech Montgomery Executive airport in Blacksburg, Virginia.

2.6 Summary

The design of the experimental facility was an integral part of this research. The planned investigation required the integrated test of both the test article (the serpentine duct), and the unique facility that could generate the required high speed dual flow environment. The future goals of the research, namely the demonstration of a robust flow control design methodology for BWB BLI serpentine inlets cannot be achieved without the successful operation of this unique test facility.

Thus, much effort was devoted to the correct design of the facility, as reported above. The facility construction was an important step that took a great deal of time and effort to complete. Combining several disciplines such as CFD, FEA, and 3D CAD models allowed more aspects of the design to be covered that otherwise would have been possible with only one or two software packages.

The successful test of the completed facility with a serpentine duct in place, and the validation of the acquired data by comparison with reported NASA results was equally important. In addition to the design and construction, an instrumentation plan was developed and installed that encompassed the key reasons for conducting the experiment, which included the boundary layer profile and distortions at the AIP of the serpentine inlet. As will be reported below, the results compared favorably with the available NASA data.

Overall, a unique facility was developed that will support research and development of robust BLI inlets with flow control for AIP distortion control, and eventually, with modifications, to an actual integrated test of a fan engine directly connected to a flow controlled inlet.

3.0 Data Reduction and Calculations

The calculations performed to characterize the flow were centered on data from two major locations on the serpentine inlet. The first location was at the front of the inlet around the throat, and the second was at the inlet AIP. The following two sections will detail the equations and calculations used in the data reduction.

3.1 Calculations at the Throat of the Serpentine Inlet

The major variable of interest at the inlet throat was the Mach number measured using the boundary layer rake and bypass duct rakes. The rakes measured total pressures at different vertical and circumferential locations, while two static pressure taps located at the bases of the rakes measured local static pressures. The combination of these two pressures at one location was enough to calculate the Mach number of the flow. For the calculations, the air was assumed to behave as a perfect gas, and the probe flow was considered isentropic. Modeling the air as a perfect gas allowed the ratio of specific heats to remain constant, as defined by γ in Equation 3.1. C_p is defined as the specific heat of a substance at constant pressure, while C_v refers to the specific heat of a substance at constant volume. A constant value of $\gamma=1.4$ was used throughout the calculations (Hill and Peterson, 1992).

$$\gamma = \frac{C_p}{C_v} \quad 3.1$$

The Mach number relationship defined by the total and static pressures at a point is given below in Equation 3.2. The variable p_o represents the total pressure, while p_s represents the static pressure.

$$\frac{p_o}{p_s} = \left(1 + \frac{\gamma - 1}{2} M^2 \right)^{\frac{\gamma}{\gamma - 1}} \quad 3.2$$

This equation was rearranged to solve for the Mach number as shown below in Equation 3.3. This equation was used to determine the Mach number at the ten probe locations on the boundary layer rake and on the three probes for each rake in the bypass duct).

$$M = \sqrt{\left(\frac{2}{\gamma - 1} \right) \left[\left(\frac{p_o}{p_s} \right)^{\frac{\gamma - 1}{\gamma}} - 1 \right]} \quad 3.3$$

The Reynolds number of the flow was calculated from probe measurements. Equation 3.4 below defines the Reynolds number for the flow through the experimental facility.

$$\text{Re} = \frac{\rho V_{ave} D_c}{\mu} \quad 3.4$$

The density and dynamic viscosity of the air, ρ and μ , respectively, were determined from a table listing air densities and dynamic viscosities as functions of the ambient temperature. The characteristic length for calculating the Reynolds number, D_c , was based on the AIP diameter of the serpentine inlet. This was the method used by NASA in the original experiment, so similar practices were followed here. The average

velocity of the flow, V_{ave} , was determined using the average Mach number along with the temperature and gas constant for air, R (Cengel and Cimbala, 2006). Equation 3.5 shows the initial form of the equation, which was rearranged to solve for the average velocity, as shown in Equation 3.6. The average Mach number was calculated using a weighted average that took into consideration the Mach numbers seen at the ten probes along with the vertical distance between probes on the boundary layer rake.

$$M_{ave} = \frac{V_{ave}}{\sqrt{\gamma RT}} \quad 3.5$$

$$V_{ave} = M_{ave} \sqrt{\gamma RT} \quad 3.6$$

The mass flow rates through the serpentine inlet and bypass duct were of interest because the ratios of those two flows are directly involved in determining the inlet boundary layer that develops. Static pressure taps at the entrance to the bypass duct and serpentine inlet were used to determine the density of the air entering each part, and the average velocity was determined as described above. The cross-sectional area, A_c , was also calculated at the entrance to both the bypass duct and serpentine inlet. These three variables were then combined to calculate the mass flow rate using Equation 3.7.

$$\dot{m} = \rho V_{ave} A_c \quad 3.7$$

3.2 Calculations at AIP of Serpentine Inlet

The calculations using the thirty-two total pressure measurements at the AIP of the serpentine inlet were guided by the recommendations provided by the industry

standard SAE ARP 1420. This standard is widely used to specify the inlet flow distortion guidelines for gas turbine engines. Since serpentine inlets will be mounted in front of turbofan engines on BWB aircraft, the distortion created by the inlet expressed in standard form is an important parameter. The circumferential position of the arms on the AIP rake is defined below by Figure 3.1.

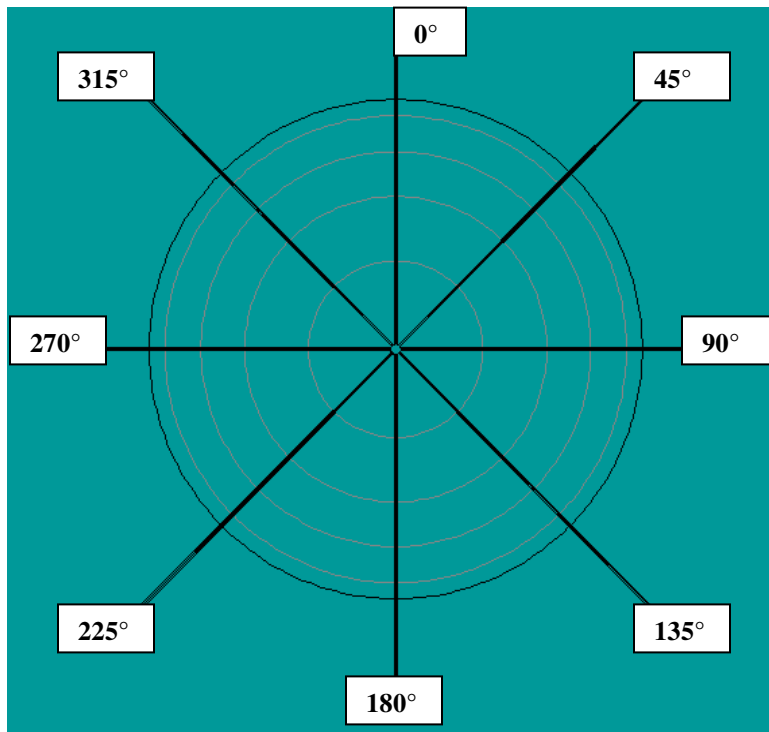


Figure 3.1 – Circumferential Locations of Arms on AIP Rake

The distortion at the AIP is defined by several different descriptor elements. These elements are broken down into two main categories, circumferential distortion elements and radial distortion elements. The circumferential elements include the intensity, extent, and multiple-per-revolution pattern. The intensity element represents the magnitude of the pressure deficiency for each radial ring, the extent represents the angular region where the pressure deficiency is located, and the multiple-per-revolution

pattern looks at the number of pressure deficient regions for each radial ring. The radial distortion element is made up of only the radial intensity, which compares the average pressure for the ring to the average pressure for the entire face of the AIP (SAE ARP 1420).

The circumferential distortion is calculated for each ring in the AIP rake, resulting in an intensity, extent, and multiple-per-revolution value for each ring. Figure 3.2 below shows a typical total pressure plot for an eight-arm AIP rake.

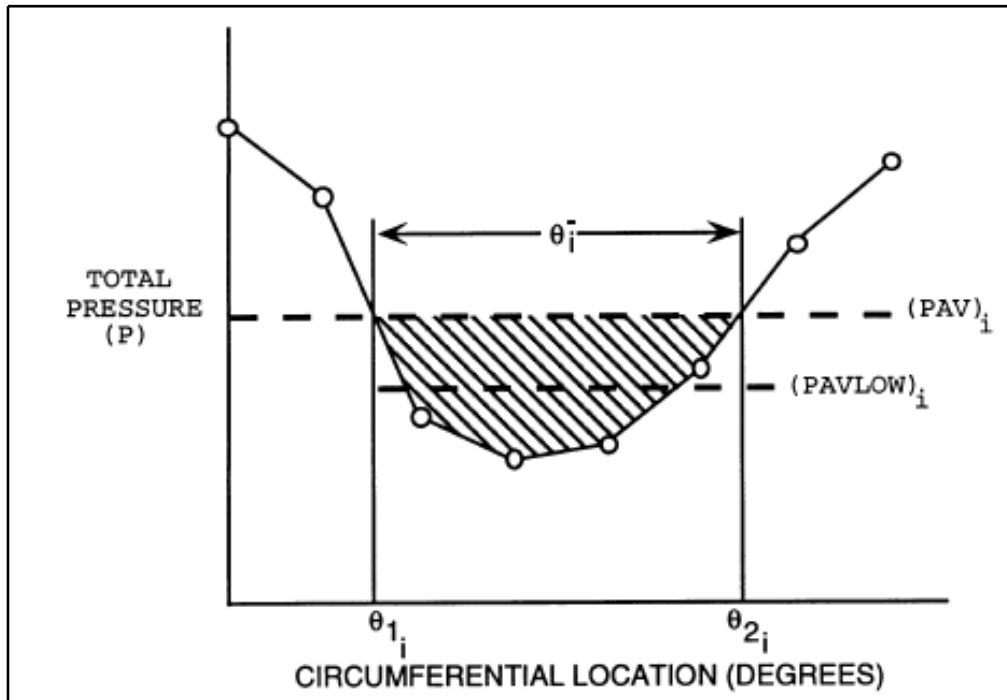


Figure 3.2 – Typical Ring Total Pressure Plot (SAE ARP 1420)

Referring to the nomenclature from Figure 3.2, the circumferential size of the low pressure region is given by the extent, described below in Equation 3.8.

$$\Theta_i^- = \Theta_{2_i} - \Theta_{1_i} \quad 3.8$$

The circumferential distortion intensity, representing the level of distortion in the flow, is then defined by Equations 3.9 through 3.11.

$$\left(\frac{\Delta PC}{P}\right)_i = \left(\frac{PAV - PAVLOW}{PAV}\right)_i \quad 3.9$$

$$PAV_i = \frac{1}{360} \int_0^{360} P(\Theta)_i d\Theta \quad 3.10$$

$$PAVLOW_i = \frac{1}{\Theta_i^- \Theta_i^+} \int_{\Theta_i^-}^{\Theta_i^+} P(\Theta)_i d\Theta \quad 3.11$$

In the above equations, PAV_i represents the ring averaged total pressure, while $PAVLOW_i$ represents the average pressure in the low pressure region. The function $P(\Theta)_i$ results from a linear fit between adjacent data points.

The above equations assume the existence of a *one-per-revolution* distortion pattern. This means there is only one pressure deficient region contained within one circumferential revolution at the AIP, resulting in a *multiple-per-revolution* value of one for the ring. If multiple low pressure regions exist, a different set of equations must be used to describe the multiple-per-revolution pattern. In Figure 3.3 below, two low pressure regions of extents Θ_{i1}^- and Θ_{i2}^- are separated by two high pressure regions of extents Θ_{i1}^+ and Θ_{i2}^+ .

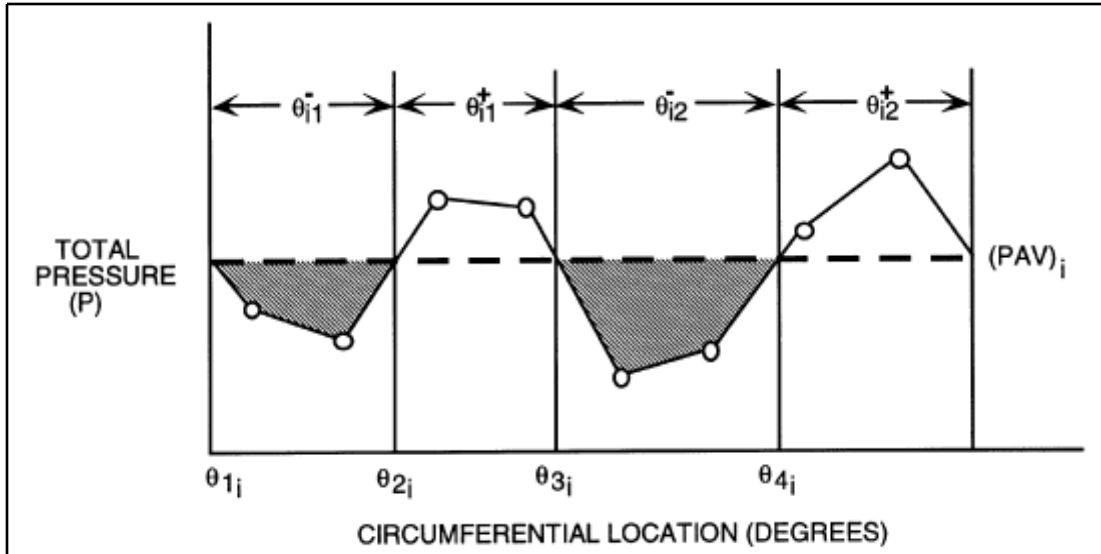


Figure 3.3 – Typical Total Pressure Plot for a Multiple-per-Revolution Pattern (SAE ARP 1420)

For patterns where the extent of the high pressure region following the low pressure region is less than twenty-five degrees, the total extent is defined using Equation 3.12 where Q is the number of low pressure regions in the pattern and k refers to the k -th low pressure region.

$$\Theta_i^- = \sum_{k=1}^Q \Theta_{ik}^- \quad 3.12$$

Using Equation 3.8 defined above to describe the circumferential distortion intensity, PAV_i is defined the same way, but $PAVLOW_i$ is now defined using Equation 3.13.

$$PAVLOW_i = \frac{1}{\Theta_i^-} \sum_{k=1}^Q \int_{\Theta_{ik}^-} P(\Theta)_i d\Theta \quad 3.13$$

This new definition for $PAVLOW_i$ results in the circumferential distortion intensity described below in Equation 3.14. It also results in a multiple-per-revolution value of one for the case where the extent of the high pressure region is less than twenty-five degrees.

$$\left(\frac{\Delta PC}{P}\right)_i = \frac{\sum_{k=1}^Q \left[\left(\frac{\Delta PC}{P}\right)_{ik} \Theta_{ik}^- \right]}{\sum_{k=1}^Q \Theta_{ik}^-} \quad 3.14$$

If the extent of the high pressure region following the low pressure region is greater than twenty-five degrees, then the resulting multiple-per-revolution pattern is greater than one. The circumferential distortion intensity is then the quantity $\left(\frac{\Delta PC}{P}\right)_{ik}$

that yields the maximum value of the quantity $\left[\left(\frac{\Delta PC}{P}\right)_{ik} \Theta_{ik}^- \right]$. The extent is then the

Θ_{ik}^- that results in the maximum value of the quantity $\left[\left(\frac{\Delta PC}{P}\right)_{ik} \Theta_{ik}^- \right]$. The multiple-per-revolution value for this ring is then given below in Equation 3.15.

$$MPR_i = \frac{\sum_{k=1}^Q \left[\left(\frac{\Delta PC}{P}\right)_{ik} \Theta_{ik}^- \right]}{\left[\left(\frac{\Delta PC}{P}\right)_{ik} \Theta_{ik}^- \right]_{\max}} \quad 3.15$$

The radial distortion element is defined only by the radial distortion intensity. The definition is given below in Equation 3.16, and is based on the nomenclature in Figure 3.4.

$$\left(\frac{\Delta PR}{P}\right)_i = \frac{PFAV - PAV_i}{PFAV} \quad 3.16$$

The variable *PFAV* refers to the area weighted face average total pressure, and is defined below in Equation 3.17, with *N* being the number of radial rings contained on the AIP rake.

$$PFAV = \frac{1}{N} \sum_{i=1}^N PAV_i \quad 3.17$$

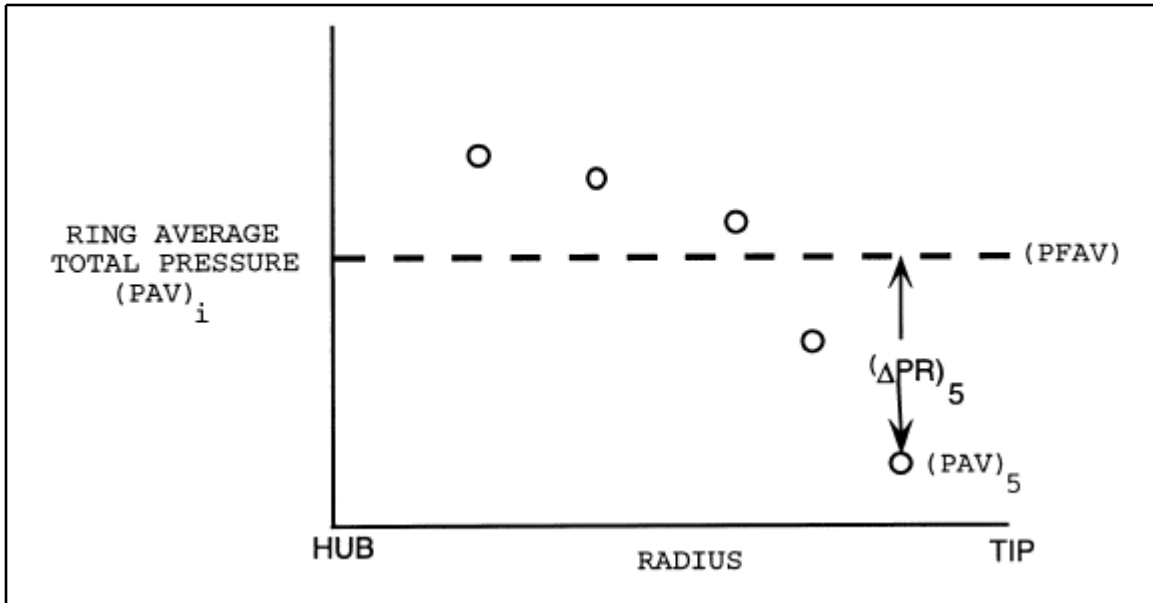


Figure 3.4 – Typical Radial Distortion Intensity Graph (SAE ARP 1420)

The radial distortion can be either positive or negative for a given ring. A positive value means the ring average total pressure is less than the face average total pressure, while a negative value means the ring average total pressure is greater than the face average total pressure. Referring to Figure 3.4 above, the three data points on the left all have negative radial distortion intensities, while the two data points on the right have

positive distortion intensities. All of the equations, nomenclature, and graphs used to define the flow distortion at the AIP in this section were taken from SAE ARP 1420.

3.3 Summary

The equations and calculations provided in the above sections were needed to characterize the flow entering the throat of the serpentine inlet, and exiting the inlet at the AIP. The throat calculations will determine the profile of the boundary layer being ingested by the inlet, which is one of the important criteria used to determine the effectiveness of the test facility. The AIP rake and subsequent calculations will help diagnose the effectiveness of the serpentine inlet at minimizing pressure losses and distortions. Knowing how the flow behaves at this location is important for the BWB application because the installed engine must accommodate the losses created by the serpentine inlet while maintaining a stability margin to prevent stalling or surging.

4.0 Results

Tests were conducted with the JT15D-1 operating at fan speeds of fifty-five percent, sixty-five percent, and seventy-five percent of rated maximum speed. Flow blockages were installed over the bypass duct exit to control the mass flow split between the bypass and the serpentine test duct. A combination of static and total pressure measurements were collected at the sixty-four locations described earlier while the engine was operating at these speeds. These data were then processed according to the data reduction techniques specified in the previous section. The results from these tests and calculations are presented below according to the locations in the experimental facility where the measurements were collected.

4.1 Boundary Layer Profiles entering Serpentine Inlet and Bypass Duct

The first data processed dealt with the boundary layer profile at the throat of the serpentine inlet. This gave an indication of how successful the experimental facility was at generating the thirty percent boundary layer profile desired. Figure 4.1 below shows the boundary layer developed when the engine was run at fifty-five percent power, which corresponded to an AIP diameter-based Reynolds number of 1.2 million. For this test, the bypass duct exit was left open to its maximum area. This created a bypass duct exit area to serpentine inlet exit area of 2.1. The resulting boundary layer profile was fully developed at thirty-six percent of the overall height of the inlet throat, and showed good agreement with the thirty percent boundary layer profile desired. This profile also had a

maximum Mach number of 0.19, which was smaller than the desired value of 0.5. To help compare these results with the CFD and other experiments run at different Mach numbers, the non-dimensionalized boundary layer profile shown in Figure 4.2 was generated. This profile was created by dividing the Mach numbers at the different probe locations by the freestream Mach number. This non-dimensionalized profile showed little variation from the original profile, and was also fully developed at thirty-six percent. The mass flow rate through the serpentine inlet for this case was calculated as 9.9 pounds-mass per second, while the mass flow rate through the bypass duct was 24.1 pounds-mass per second. This created a mass flow ratio of 2.4 favoring the flow through the bypass duct.

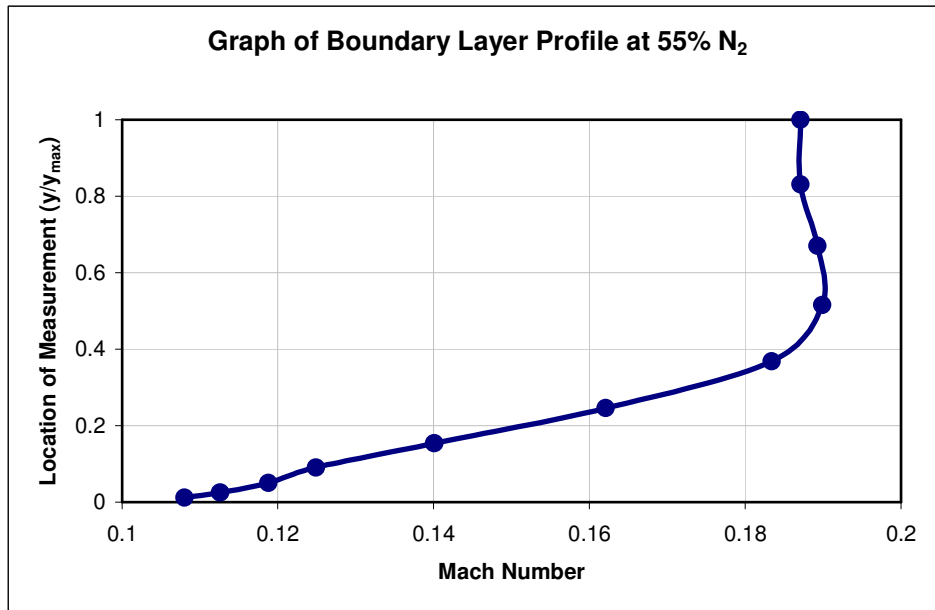


Figure 4.1 – Boundary Layer Profile with Engine Operating at 55% Speed

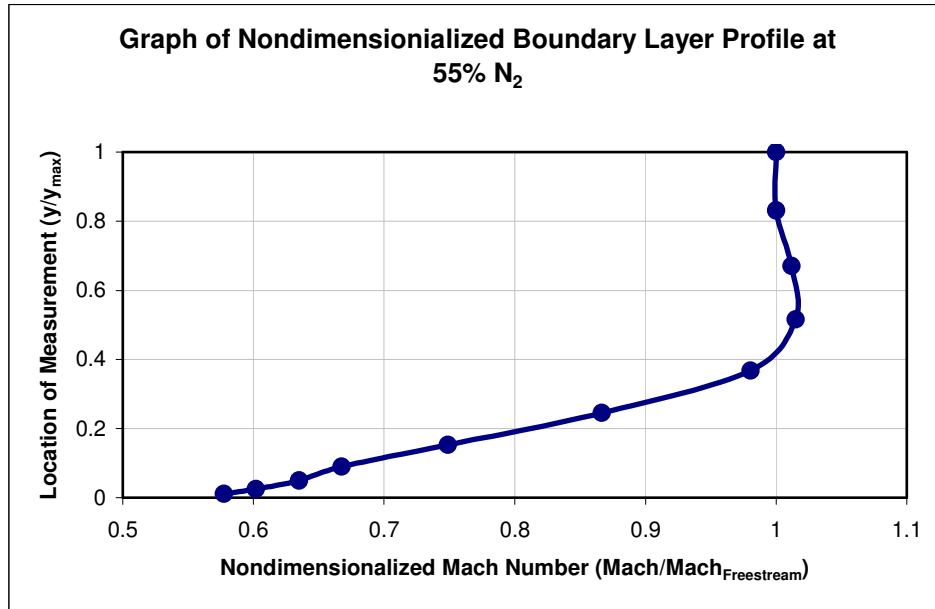


Figure 4.2 – Non-dimensionalized Boundary Layer Profile with Engine Operating at 55% Speed

The second engine fan speed tested was at sixty-five percent, resulting in a Reynolds number of 1.5 million. For this initial test at sixty-five percent speed, the bypass duct exit area was again left fully open, creating the same area exit ratio with the serpentine inlet of 2.1. It generated a maximum Mach number at the throat of 0.25, which was larger than the 0.19 created when running the engine at fifty-five percent speed, but was still well below the desired Mach number of 0.5. This engine fan speed resulted in a boundary layer profile that was not fully developed until eighty-three percent of the inlet height, as shown below in Figure 4.3. Non-dimensionalizing this profile with the freestream Mach number gave the same results, similar to what was observed at the lower engine speed. This boundary layer profile was much thicker than the desired profile of thirty percent thickness.

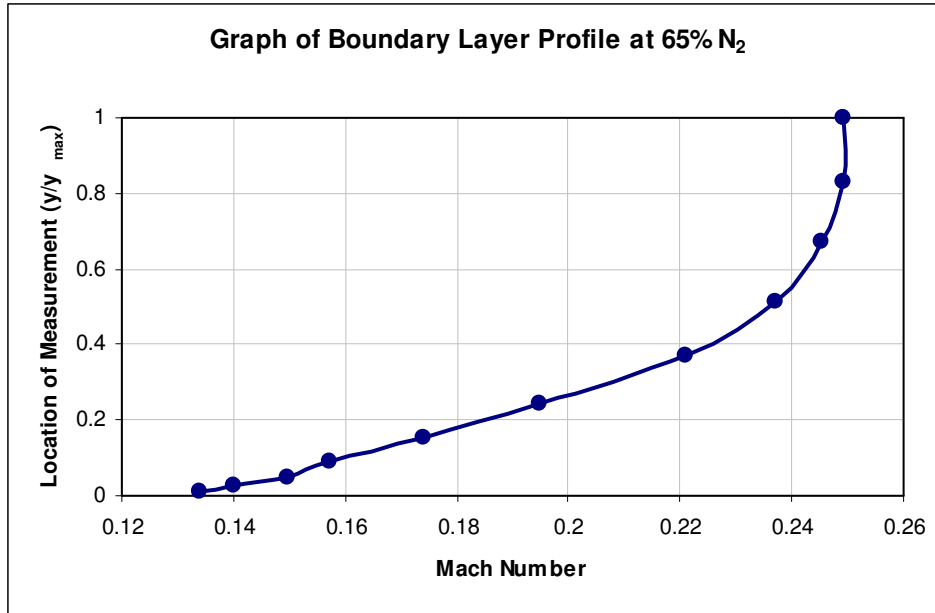


Figure 4.3 – Boundary Layer Profile with Engine Operating at 65% Speed

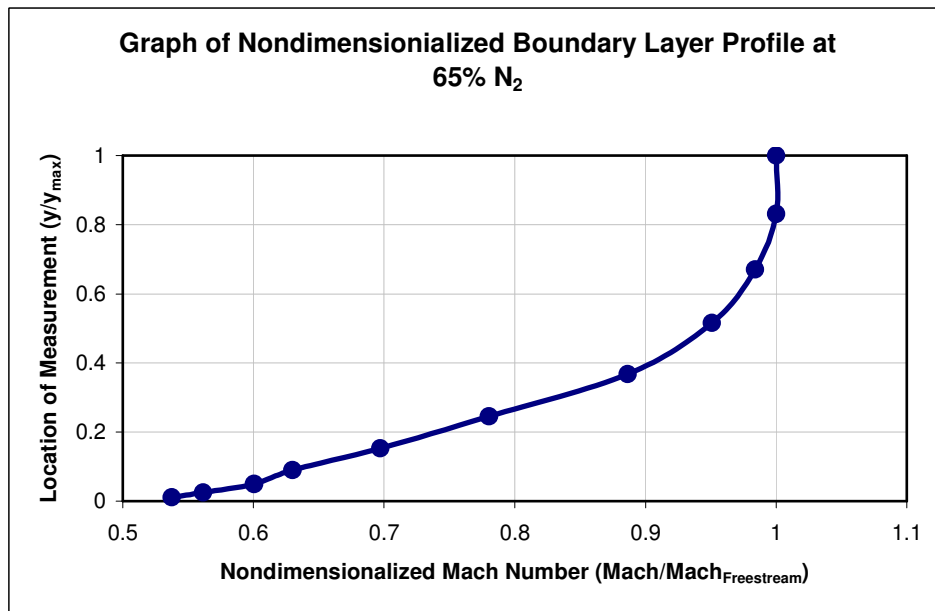


Figure 4.4 – Non-dimensionalized Boundary Layer Profile with Engine Operating at 65% Speed

The reason for this large boundary layer thickness was the increased mass flow ratios through the bypass and the serpentine inlet. The mass flow rate through the bypass duct was calculated as 29.5 pounds-mass per second, while the mass flow rate through

the serpentine inlet was only 11.9 pounds-mass per second. This resulted in a mass flow rate through the bypass duct that was 2.5 times greater than the mass flow rate through the serpentine inlet. Figure 4.5 below illustrates what was happening to the flow. More air was being pulled through the bypass duct, preventing the air in the center of the inlet ramp from being pulled through the serpentine inlet and forming the correct boundary layer profile.

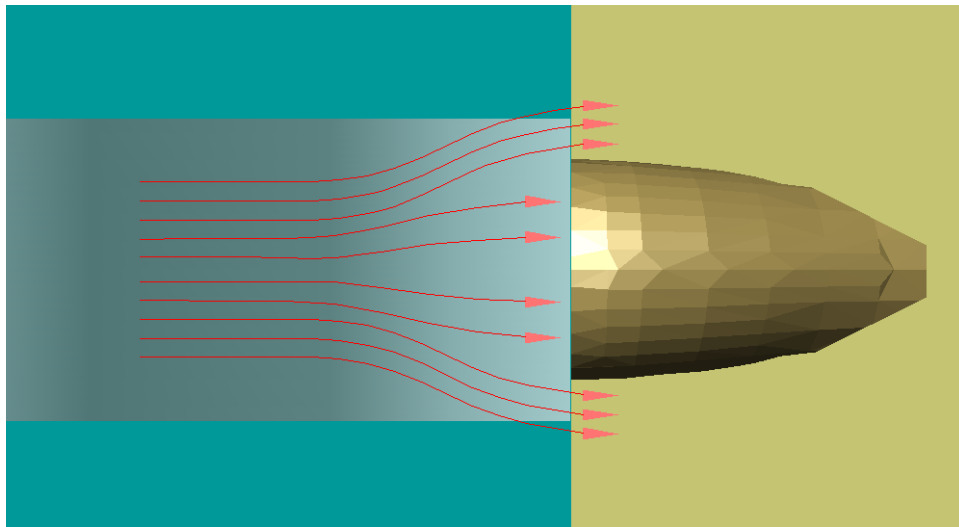


Figure 4.5 – Air Flow through Bypass Duct and Serpentine Inlet Generating a Thick Boundary Layer Profile

To correct this problem, a blockage plate that served as a flow control valve as previously described was installed over the exit area where the bypass duct flow emptied into the rear plenum. This blockage reduced the exit area for the bypass duct, restricting the mass flow rate that could be pulled through it. Operating at the same fan speed, this caused the engine to increase the mass flow rate through the serpentine inlet, generating an improved boundary layer profile. As expected, determining the correct blockage for a

certain engine speed was an iterative process. An illustration of the effect of restricting the bypass flow is shown below in Figure 4.6.

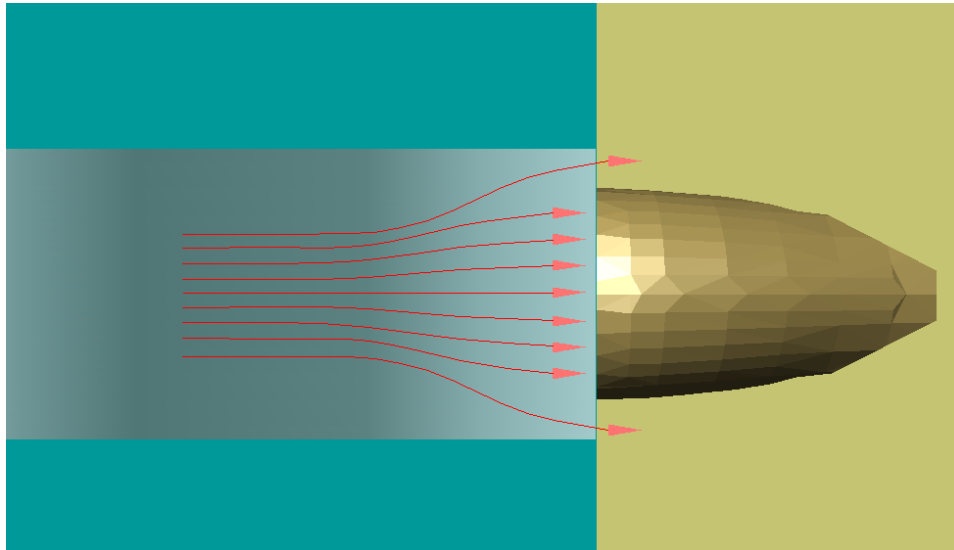


Figure 4.6 – Air Flow through Bypass Duct and Serpentine Inlet Generating the Correct Boundary Layer Profile

To prove this boundary layer control process, a blockage plate was installed over the exit area for the bypass duct and the engine was accelerated to sixty-five percent speed. The new blockage installed reduced the exit area by fifty-four percent, creating an exit area that was only 1.1 times larger than the serpentine inlet exit area. This was down from the 2.1 exit area ratio from the first test at sixty-five percent engine speed. This test resulted in a similar Reynolds number of 1.5 million and maximum Mach number of 0.25. However, as Figure 4.7 shows below, restricting the bypass exit area altered the boundary layer profile developed. It resulted in a boundary layer profile that was fully developed at a thickness of forty-five percent. This profile was fully developed at almost half the height from the previous test at sixty-five percent speed. Non-dimensionalizing had a slight effect on the thickness, reducing it to fully developed at only forty-two

percent of the inlet height, as shown in Figure 4.8. Examining the mass flow rates proved that the ratio of the flow through the bypass duct versus through the serpentine inlet was a primary factor determining the thickness of the boundary layer developed. The mass flow rate through the bypass duct for this test was 24.2 pounds-mass per second, while the mass flow rate through the serpentine inlet was 12.3 pounds-mass per second. This resulted in a mass flow rate through the bypass duct that was only two times greater than the mass flow rate through the serpentine inlet, down from the ratio of 2.5 for the first test at sixty-five percent engine speed.

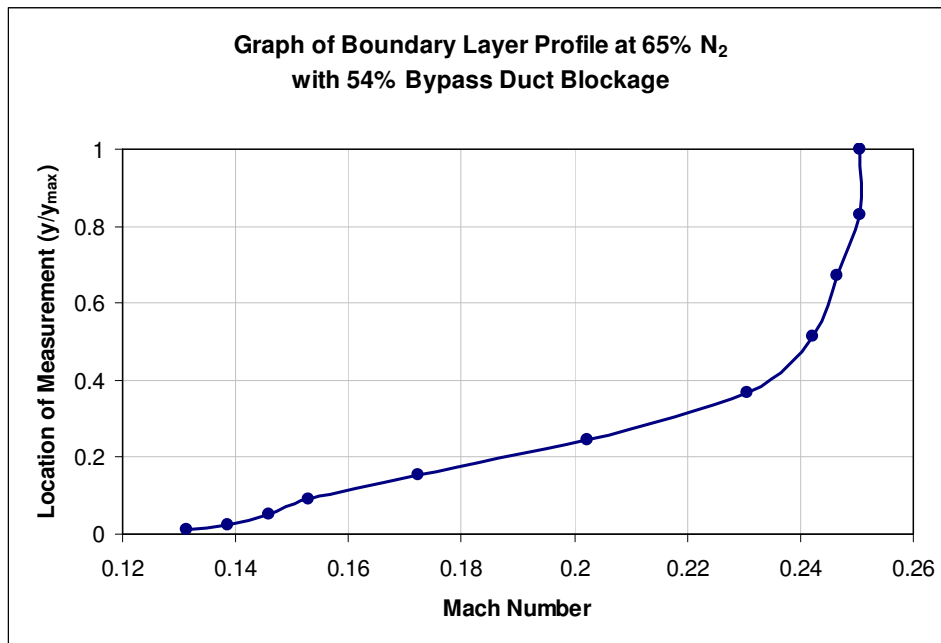


Figure 4.7 – Boundary Layer Profile with Engine Operating at 65% Speed and 54% Bypass Duct Blockage

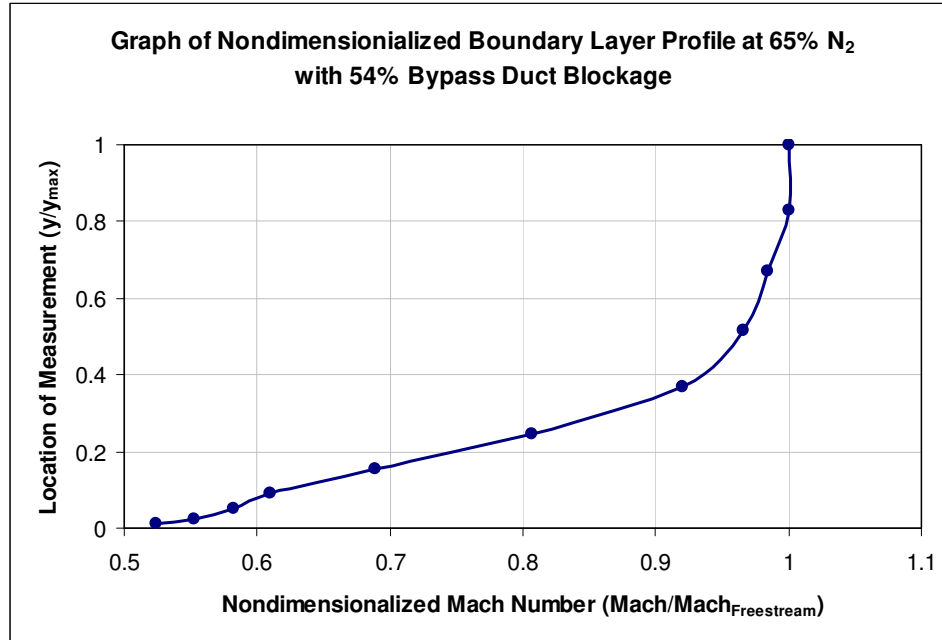


Figure 4.8 – Non-dimensionalized Boundary Layer Profile with Engine Operating at 65% Speed and 54% Bypass Duct Blockage

A fourth test was run with the engine operating at seventy-five percent speed with the same fifty-four percent blockage in the bypass duct exit area. This test had an AIP area-based Reynolds number of 2.4 million, and a maximum measured Mach number of almost 0.4 at the serpentine inlet throat. This Mach number was closer to the goal value of 0.5. The increasing maximum Mach numbers with increasing engine speed were expected, and although no tests conducted here achieved a Mach number of 0.5, the engine had ten to fifteen percent rated fan speed remaining that could be used to conduct tests at higher speeds that could result in Mach numbers of 0.5. Running the engine at seventy-five percent speed with the 54% bypass area blockage resulted in a boundary layer profile that was not fully developed until eighty-two percent of the inlet height, as shown in Figure 4.9. This result was similar to that seen when the engine was run at sixty-five percent speed with no flow blockage for the bypass duct. Non-dimensionalizing gave a similar profile in Figure 4.10 which also was fully developed at

approximately eighty-two percent of the inlet height. The mass flow rate through the bypass duct was 31.0 pounds-mass per second, while the mass flow rate through the serpentine inlet was 18.3 pounds-mass per second. For this test, the flow rate through the bypass duct was 1.7 times greater than the flow through the serpentine inlet. However, the thick boundary layer shows that more blockage is required to reduce the mass flow rate through the bypass duct even more. The exact amount of blockage needed would have to be determined experimentally, but should give results similar to those at sixty-five percent speed.

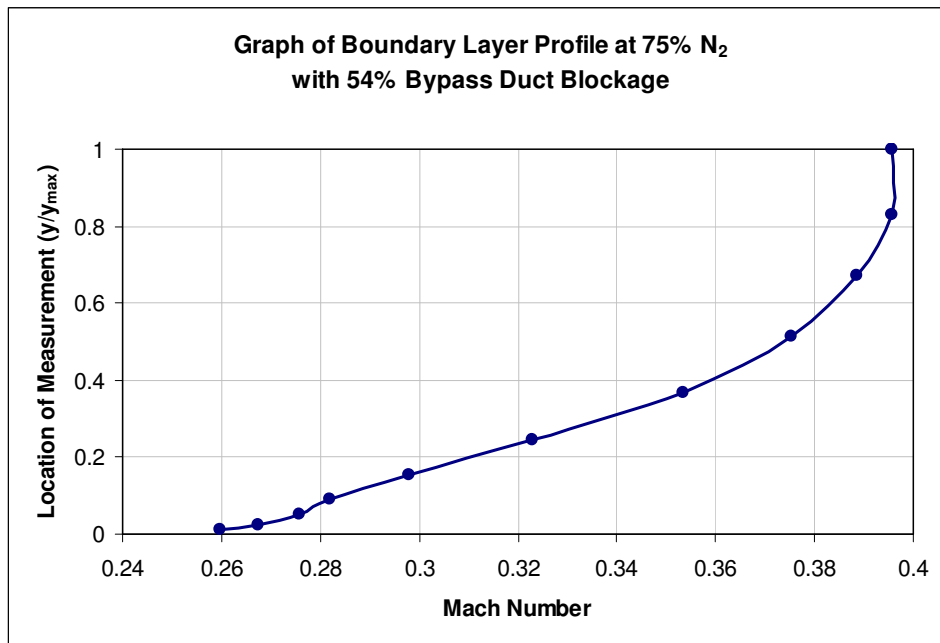


Figure 4.9 – Boundary Layer Profile with Engine Operating at 75% Speed and 54% Bypass Duct Blockage

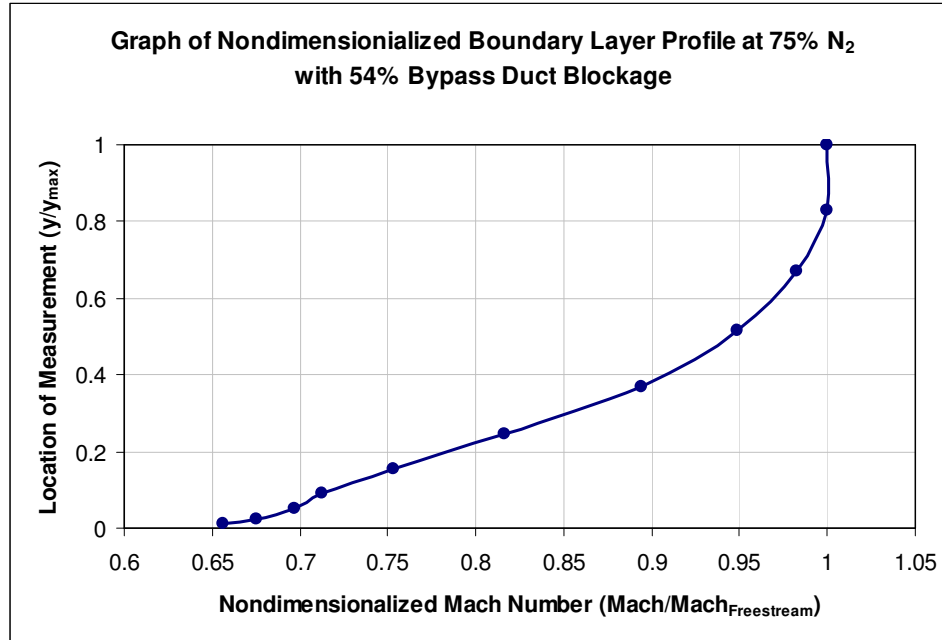


Figure 4.10 – Non-dimensionalized Boundary Layer Profile with Engine Operating at 75% Speed and 54% Bypass Duct Blockage

Using the data collected from the previous tests, a prediction can be made regarding the correct mass flow rates needed through the bypass duct and serpentine inlet, along with the correct amount of bypass duct blockage needed to achieve the correct boundary layer profile at seventy-five percent engine speed. Based on the decrease in the mass flow ratios, the bypass duct needs a mass flow rate of 24.3 pounds-mass per second, while the serpentine inlet needs a mass flow rate of 15.8 pounds-mass per second. This mass flow ratio can be achieved by blocking seventy-six percent of the bypass duct exit area. The extrapolations used to determine these values are shown below in Figures 4.11 and 4.12.

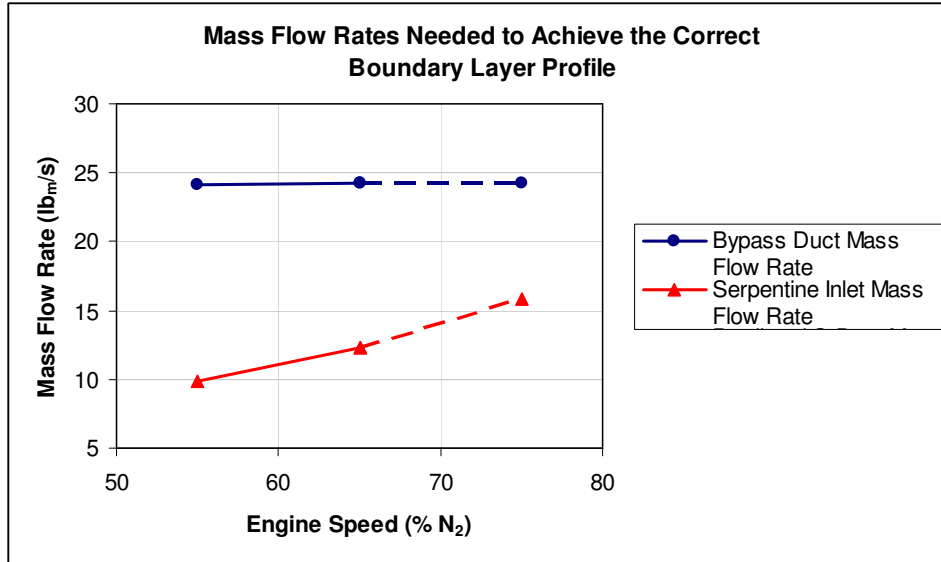


Figure 4.11 – Predicted Mass Flow Rates at 75% Engine Speed

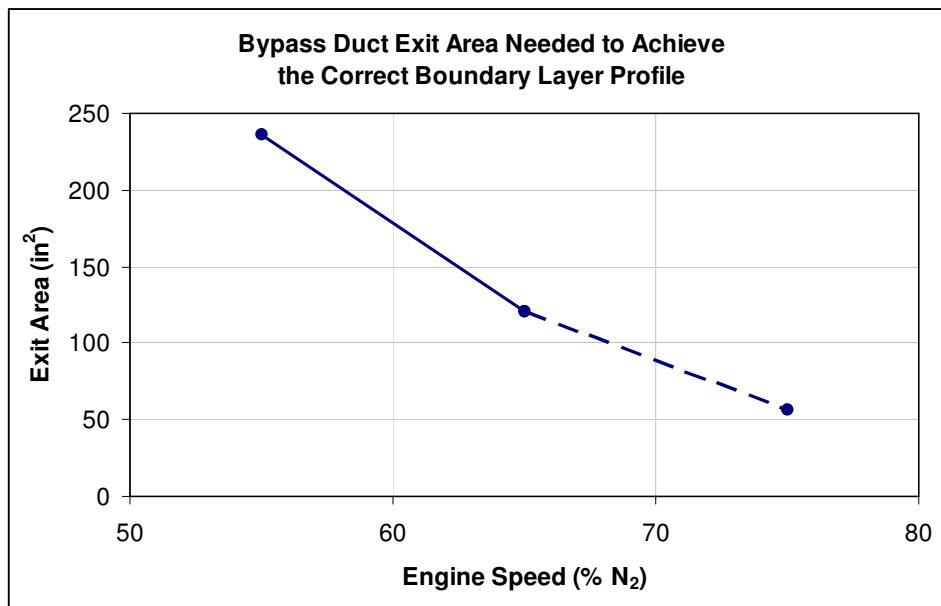


Figure 4.12 – Predicted Bypass Duct Exit Area at 75% Engine Speed

In addition to the boundary layer profile, the velocity profile of the air entering the bypass duct was also examined. It was used to determine the uniformity of the flow entering the bypass duct, along with the speed associated with that flow. As shown in Figures 4.13, 4.14, and 4.15, air was entering the bypass duct at a higher velocity at the

circumferential locations of forty-five degrees and ninety degrees at engine speeds of fifty-five percent and sixty-five percent. However, at seventy five percent engine speed in Figure 4.16, that pattern reverses, with flow entering at highest velocity at a circumferential location of one hundred thirty-five degrees. Figures 4.13 through 4.16 also show the presence of a boundary layer that formed along the inner surface of the bypass duct. This was evidenced by the lower Mach numbers at the radial locations closest to the wall, and then increasing Mach numbers as the distance from the wall was increased. We have to explain why the mach numbers were different at 45 and 135 degrees.

With no blockage in place, the maximum Mach numbers in the bypass duct at fifty-five percent and sixty-five percent speed were greater than the Mach numbers seen at the throat of the serpentine inlet. The extra mass flow being pulled through the bypass duct was causing the air to accelerate more, resulting in higher Mach numbers. However, installing the blockage for the bypass duct reduced the velocity and Mach numbers of the flow entering it. This can be seen by comparing Figures 4.14 and 4.15. In Figure 4.14 where no blockage was present, the maximum Mach numbers between the three probes ranged from 0.26 to 0.29. But, with the blockage installed in Figure 4.15, the maximum Mach numbers dropped to a range from 0.22 to 0.25. The extra mass flow being pulled through the serpentine inlet caused the mass flow entering the bypass duct to reduce, and therefore the velocity to decelerate. Figure 4.16 shows a similar result at seventy-five percent engine speed, where the maximum Mach numbers range from 0.25 to 0.34. These Mach numbers are substantially smaller than the observed maximum Mach numbers at the serpentine inlet throat of almost 0.4.

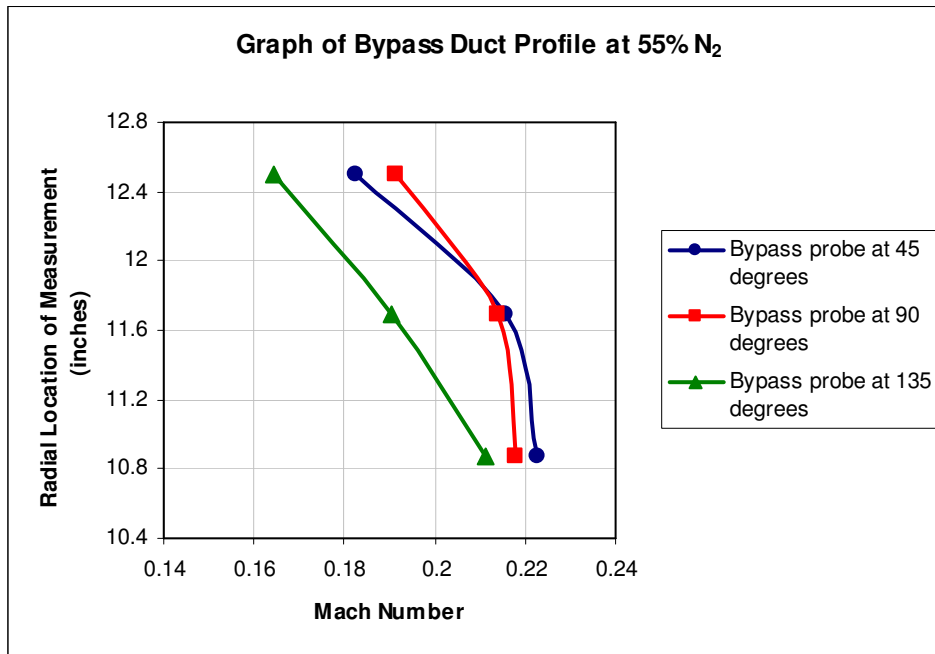


Figure 4.13 – Bypass Duct Profile with Engine Operating at 55% Speed

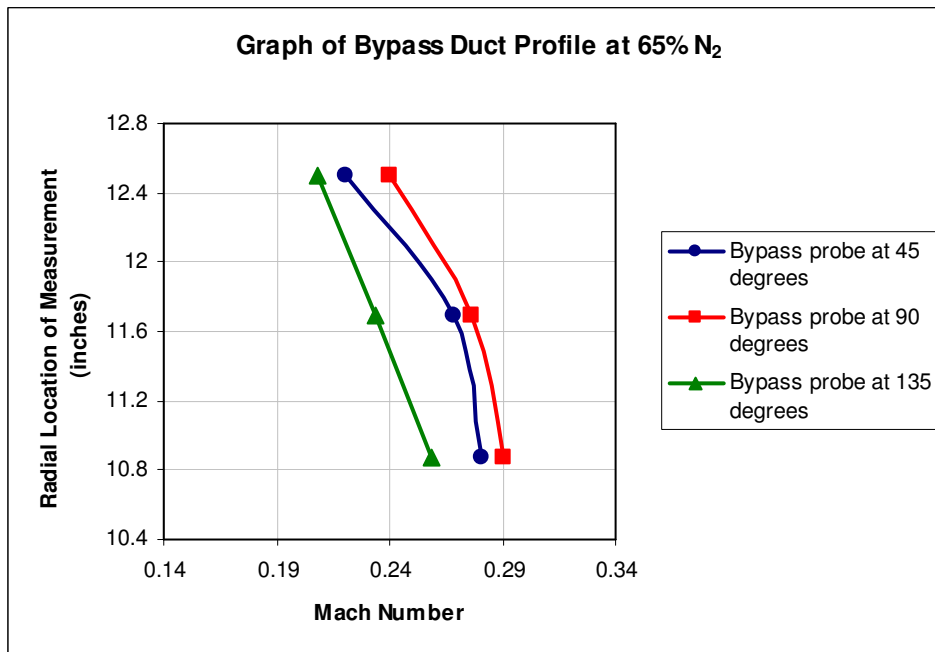


Figure 4.14 – Bypass Duct Profile with Engine Operating at 65% Speed

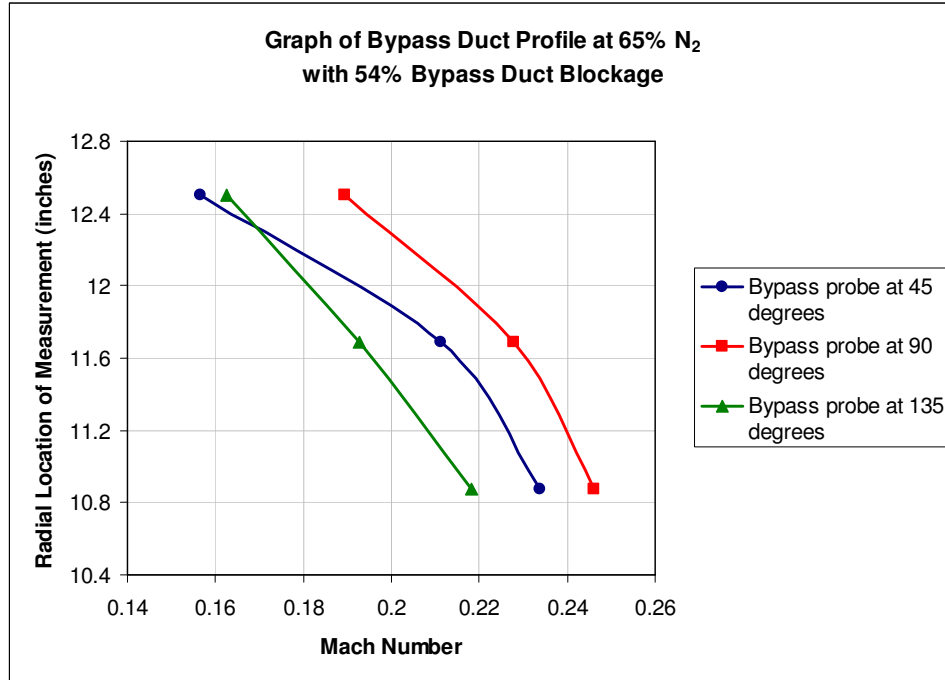


Figure 4.15 – Bypass Duct Profile with Engine Operating at 65% Speed and 54% Bypass Duct Blockage

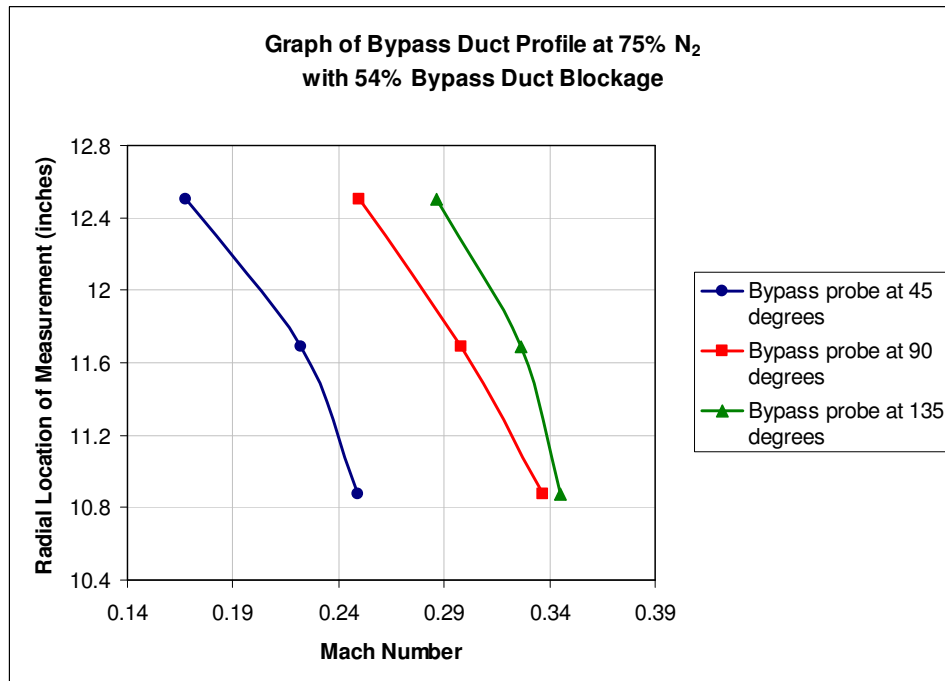


Figure 4.16 – Bypass Duct Profile with Engine Operating at 75% Speed and 54% Bypass Duct Blockage

The bypass duct profiles also revealed that the flow was not symmetrical entering the duct. If the flow was symmetrical, the profiles at the forty-five degree and one hundred thirty-five degree locations would have been equal. As the figures above show, the profiles were different at these two locations for all of the tests run. Inspection of the facility after the runs showed that the serpentine inlet and bypass duct blockages were not perfectly aligned along the centerline of the experiment. The lip of the serpentine inlet had a 0.25 inch smaller circumferential opening on the side with the forty-five degree probe. This smaller radius decreased the area the flow had to enter the bypass duct on that side, resulting in higher Mach numbers than what was seen on the opposite side. This caused the profile differences for the runs at fifty-five percent and sixty-five percent engine speeds. When the bypass duct blockage plate was installed, the opening was concentrated on the side containing the one hundred thirty-five degree probe. This resulted in more mass flow being pulled through that side of the bypass duct, increasing the Mach numbers at that probe. At sixty-five percent engine speed with the blockage plate installed, the extra mass flow through the one hundred thirty-five degree side caused the Mach number close to the duct wall to be greater than the forty-five degree probe side, but the smaller area on the forty-five degree side caused larger Mach numbers in the freestream for that side. When the engine speed was increased to seventy-five percent speed, the extra mass flow through the one hundred thirty-five degree side overpowered the smaller area on the forty-five degree side, resulting in higher Mach numbers entering the bypass duct at all three radial locations on the probe.

4.2 Static Pressures in Experimental Facility

The static pressures that existed in the experimental facility during operation were needed for performing calculations, but were also important because they gave an indication of the local forces and losses present. These pressures and losses load the facility structure, so monitoring the pressures was necessary for safe tests. In addition to providing information about the forces present, the static pressure plots helped to estimate the stability margin of the engine by monitoring the pressure just upstream of the fan casing in the engine inlet. A large static pressure loss at this location would cause the fan to stall, and could eventually lead to damage of the engine or experiment if operation continued. Figures 4.17 and 4.18 below summarize the static pressures present in the facility at fifty-five percent and sixty-five percent engine speed, respectively, with no blockage in place for the bypass duct.

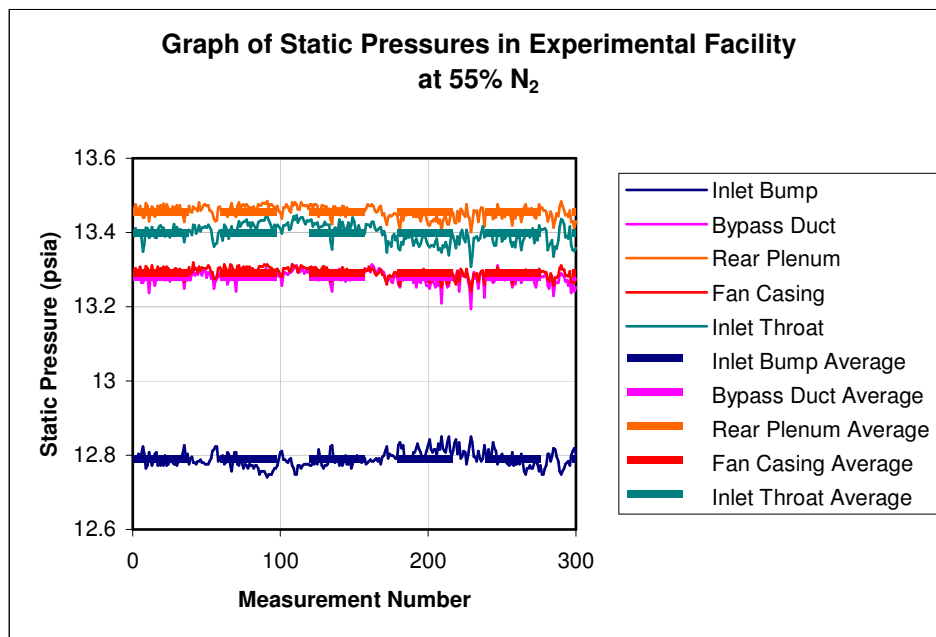


Figure 4.17 – Local Static Pressures in Experimental Facility at 55% Engine Speed

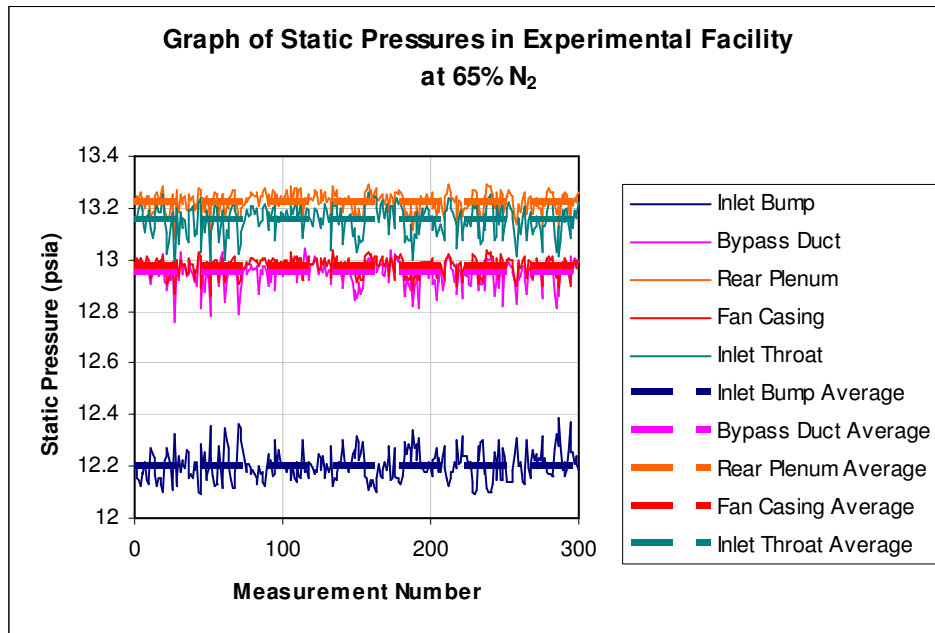


Figure 4.18 – Local Static Pressures in Experimental Facility at 65% Engine Speed

Examining the above figures shows some unsteadiness in the facility. Because a jet engine was used to generate the flow, a perfectly steady test could not be achieved. The problem associated with the unsteadiness was solved by calculating the average of all the measurements taken to arrive at one average value for each measurement location. When operating at fifty-five percent speed, the maximum static pressure loss below atmospheric pressure was 0.9 psi, seen at the maximum height of the inlet ramp. This region was expected to see the largest static pressure losses because it had the smallest cross-sectional area, resulting in the highest velocity flow. The fan casing saw a pressure loss of only 0.3 psi below atmospheric pressure, which was well within the two psi pressure loss deemed acceptable. At sixty-five percent speed, the location at the maximum height of the inlet ramp again saw the greatest static pressure loss of 1.5 psi. The static pressure loss in the fan casing increased to 0.7 psi, but was still within an

acceptable level. In both cases, the minimum pressure loss was seen in the rear plenum. This was expected because it contained the lowest speed flow and largest area, but also showed the plenum acted as it was designed, serving as a diffusion chamber for the flow to decelerate and increase pressure prior to entering the inlet of the turbofan engine jet engine.

Installing the flow blockage for the bypass duct caused several changes in the static pressures seen in the facility at sixty-five percent engine speed. The maximum static pressure loss still occurred at the maximum height of the inlet ramp, but the magnitude of the loss decreased to 1.3 psi. However, although the loss at the inlet ramp was decreased, the loss measured at the fan casing increased to 0.8 psi. It is an important result to note that installing blockage in front of the bypass duct increased the losses in the fan casing, because this affects the overall stability and safety of the experimental setup and the jet engine. Installing blockage increases the losses of total pressure, resulting in a reduced fan casing pressure. This reduces the fan stall margin. This result is shown below in Figure 4.19.

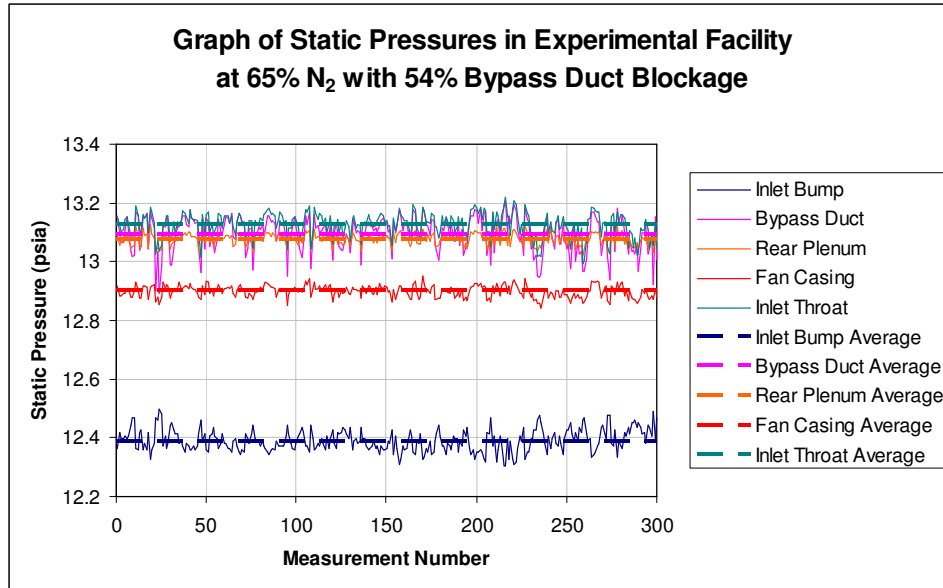


Figure 4.19 – Local Static Pressures in Experimental Facility at 65% Engine Speed with 54% Bypass Duct Blockage

The static pressures measured when running the engine at seventy-five percent speed are shown in Figure 4.20. At that speed, the maximum static pressure loss in the facility increased to 2.2 psi and was again located at the maximum height of the inlet ramp. The loss in the fan casing increased to 1.4 psi, which approached the maximum loss of two psi that was set as the threshold for safe operation. In addition to the static pressure loss in the fan casing, another concern were the spikes in static pressures seen around measurement numbers one hundred ten, one hundred eighty, and from two hundred sixty to three hundred. Upon test termination, the inlet ramp was found to be distorted. This was deemed to be the cause of the increased pressure losses. The inlet ramp also produced audible vibrations during the tests. The condition was deemed unsafe, and the test was stopped before a complete set of data including AIP measurements could be taken. For operation at the 75% fan speed level, extra reinforcing

is needed to withstand the large static pressure losses that exist on top of the inlet ramp assembly.

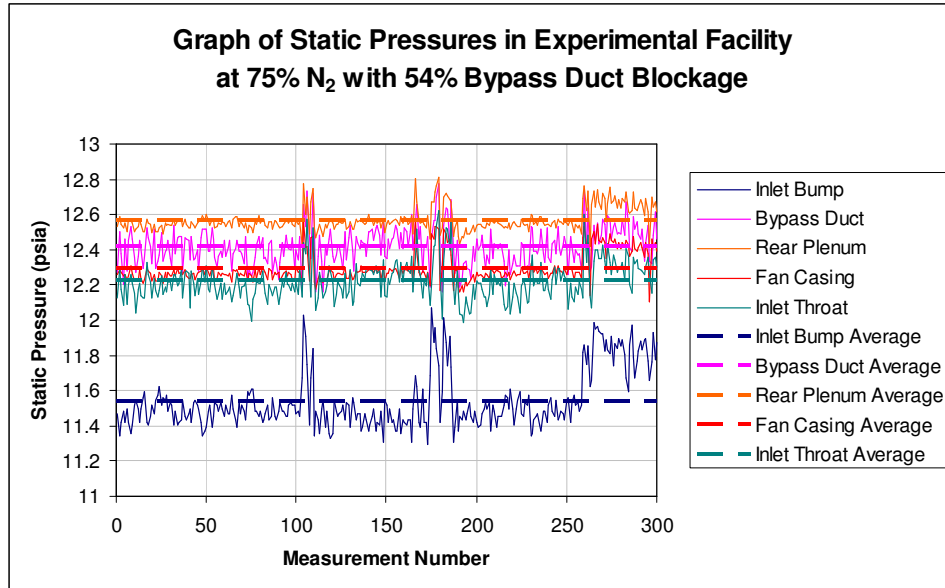


Figure 4.20 – Local Static Pressures in Experimental Facility at 75% Engine Speed with 54% Bypass Duct Blockage

4.3 AIP Data

The results at the AIP of the serpentine inlet are focused on the circumferential and radial distortion intensities, along with the extents of the distortion and the multiple-per-revolution patterns. The circumferential distortion elements for the two fan speeds tested will be given first, followed by the radial distortion element. It is noted that the reported distortions are influenced by the inlet boundary layer thickness of the serpentine duct flow.

4.3.1 Circumferential Distortion Elements

The results of the circumferential distortion descriptors provide insight into the magnitude and size of the distortion pattern. The intensity and extent are both needed to understand whether the pressure deficient region has a large or small magnitude, and whether it is spread out over a large or small radial region. The multiple-per-revolution pattern describes the number of low pressure regions the fan blades must pass through during each revolution.

Figure 4.21 shows a graph of the total pressures for the probes in each ring at the AIP, along with the average total pressure and average low pressure for the ring. Figure 4.22 below shows a contour plot of the total pressure losses associated with the graphs from Figure 4.21. The pressure losses in the contour plot were normalized using atmospheric pressure. Table 4.1 summarizes the distortion intensities associated with each ring. The total inlet pressure recovery was 0.993 for the case below.

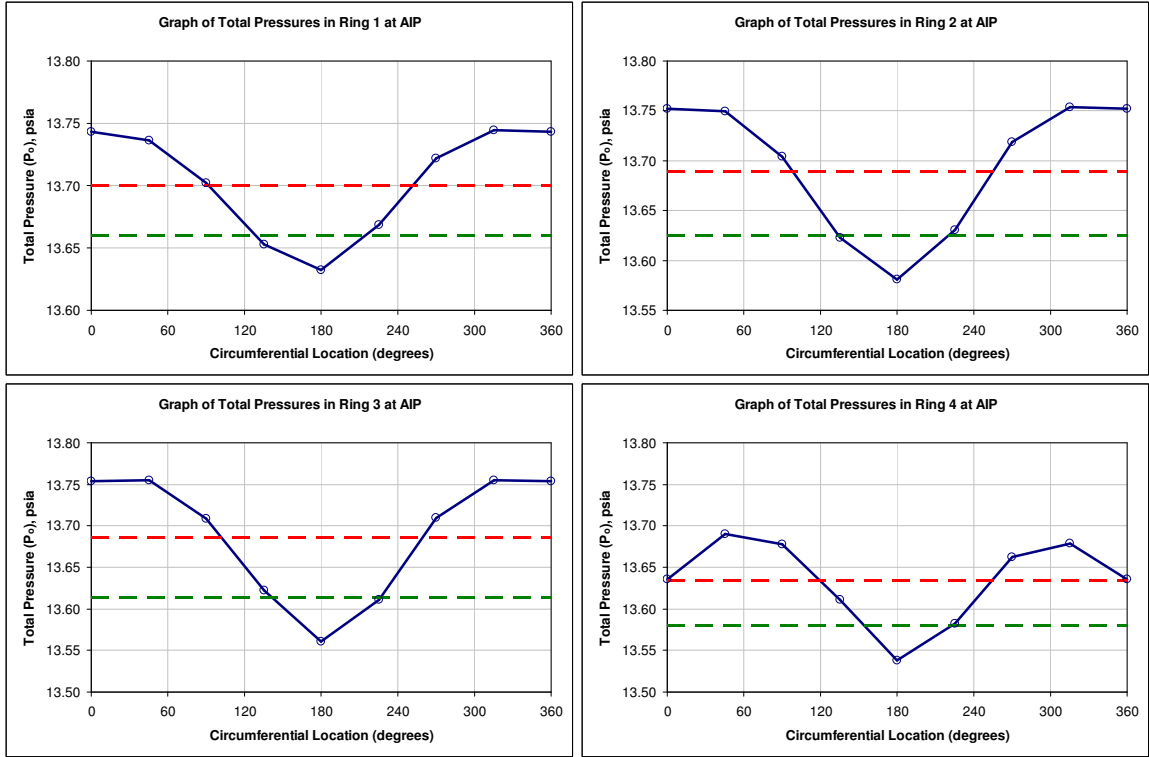


Figure 4.21 – Circumferential Distortion Graphs at 55% Engine Speed

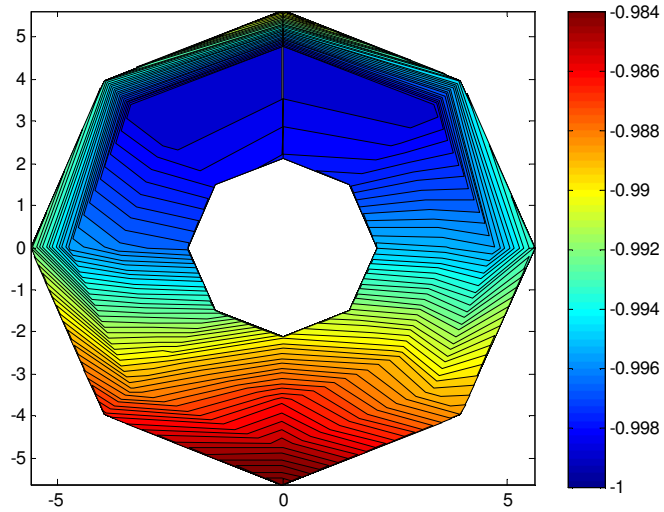


Figure 4.22 – AIP Total Pressure Loss at 55% Engine Speed

**Table 4.1 – Circumferential Distortion Intensities
at 55% Engine Speed**

Ring	DPCP_i
1	0.0030
2	0.0047
3	0.0052
4	0.0040

The average distortion seen across all rings was 0.0042. The extent of the distortion associated with each ring is given in Table 4.2.

**Table 4.2 – Circumferential Distortion Extents
at 55% Engine Speed**

Ring	Extent (degrees)
1	160
2	156
3	156
4	134

The graphs and tables above show that the main low pressure regions were located at the bottom of the inlet. While the intensities showed that the magnitude of these pressure losses was small, the extents showed they were spread out across a wide section of the AIP. Since there was only one low pressure region for each ring, the multiple-per-revolution pattern for each ring was one, as shown below in Figure 4.23.

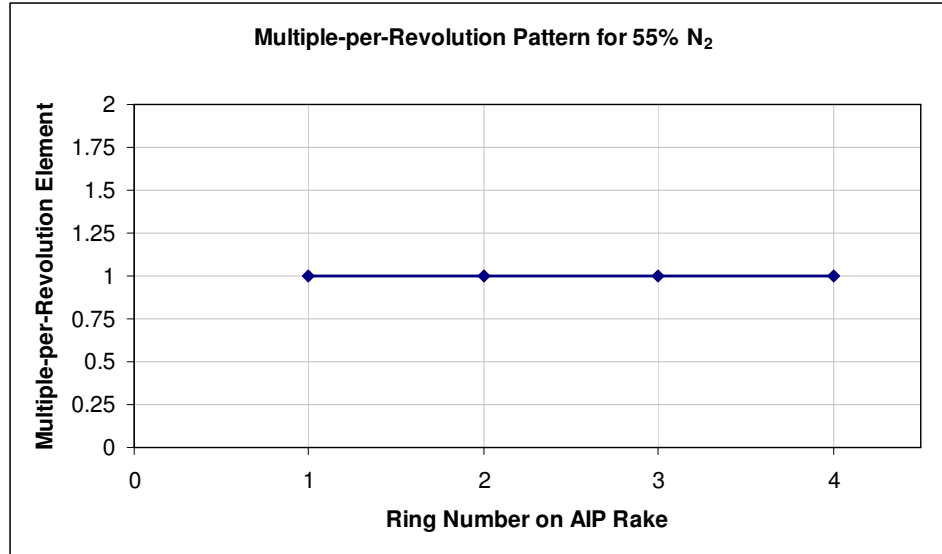


Figure 4.23 – Multiple-per-Revolution Pattern for Inlet at 55% Engine Speed

When the engine fan speed was increased to sixty-five percent speed with no bypass duct flow blockage, the magnitudes of the distortions increased, but the profiles stayed relatively constant. The total pressure recovery for the inlet dropped to 0.987, and the average distortion intensity increased to 0.0075. Figure 4.24 shows a graph of the total pressures in the different AIP rings, while Figure 4.25 shows a contour plot of these pressure losses. Tables 4.3 and 4.4 summarize the distortion intensities and extents associated with each ring, respectively.

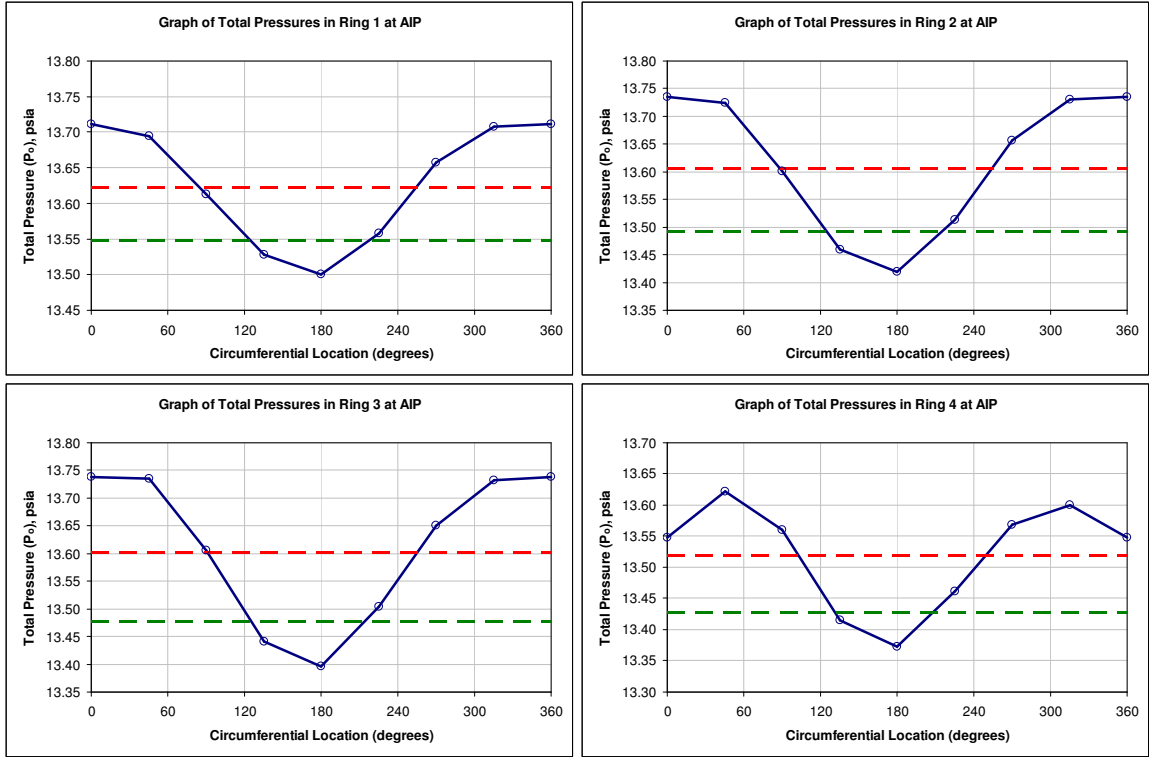


Figure 4.24 – Circumferential Distortion Graphs at 65% Engine Speed

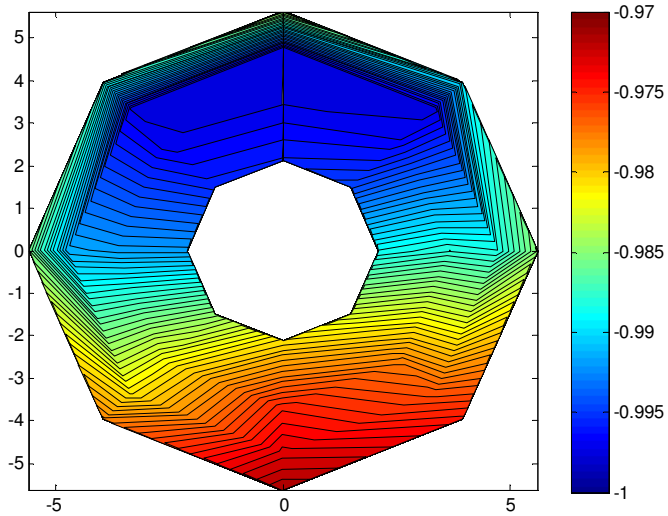


Figure 4.25 – AIP Total Pressure Loss at 65% Engine Speed

Table 4.3 – Circumferential Distortion Intensities at 65% Engine Speed

Ring	DPCP _i
1	0.0055
2	0.0084
3	0.0091
4	0.0068

Table 4.4 – Circumferential Distortion Extents at 65% Engine Speed

Ring	Extent (degrees)
1	168
2	165
3	163
4	146

The low pressure region in this case also occurred at the bottom of the serpentine inlet, and was spread out over a slightly larger radial area. The single low pressure region in each ring meant the multiple-per-revolution pattern was once again one for all four rings, as shown below in Figure 4.25.

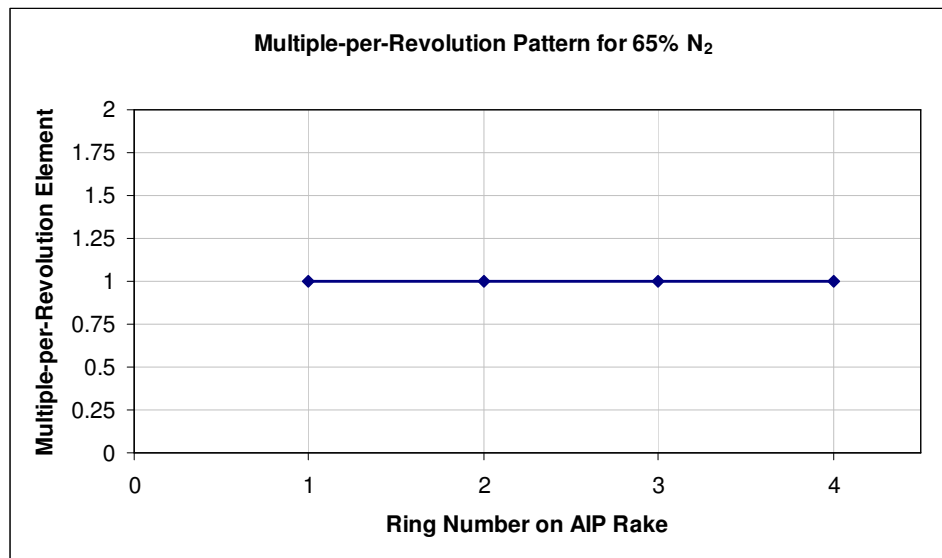


Figure 4.26 – Multiple-per-Revolution Pattern for Inlet at 65% Engine Speed

Installing the flow blockage for the bypass duct affected not only the boundary layer profile, but also the circumferential distortion elements. With fifty-four percent of the bypass exit area blocked, the total pressure recovery for the inlet dropped to 0.982 while the average circumferential distortion intensity increased to 0.0098. The extents associated with this intensity also increased, resulting in a pressure deficient region with a larger magnitude distributed over a larger area at the AIP. Similar to the first two tests, the low pressure region was concentrated in the bottom half of the duct toward the middle. Figures 4.27 and 4.28 along with Tables 4.5 and 4.6 summarize the distortion at the AIP when the engine was run at sixty-five percent fan speed with the bypass duct blockage installed.

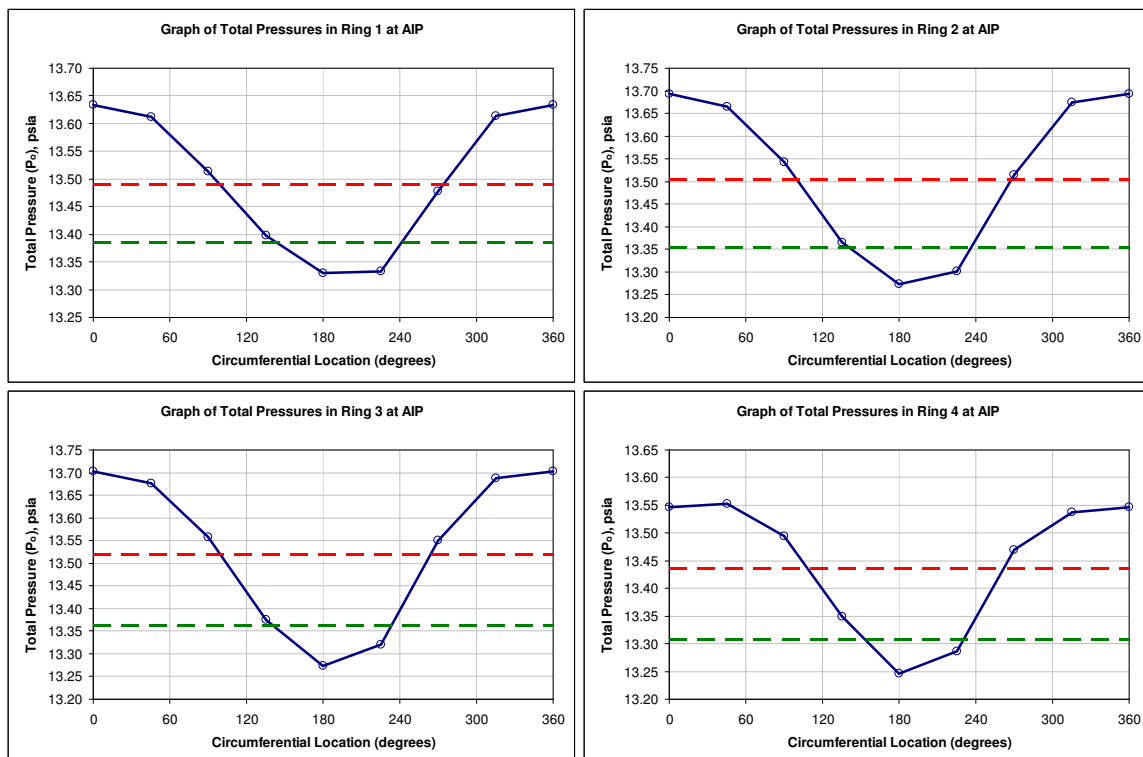


Figure 4.27 – Circumferential Distortion Graphs at 65% Engine Speed with 54% Bypass Duct Blockage

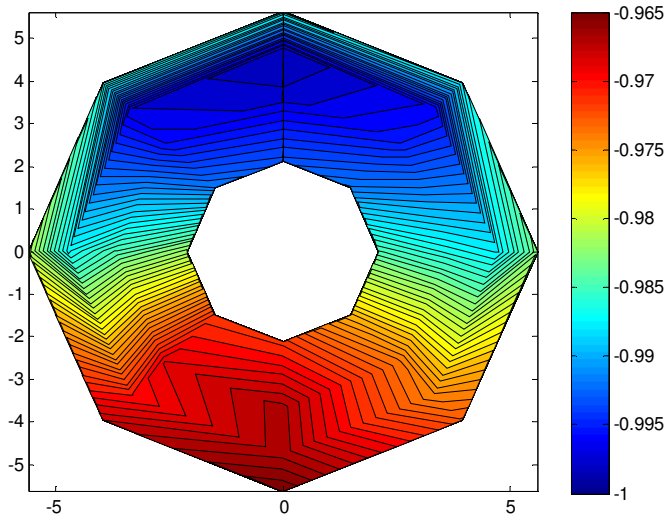


Figure 4.28 – AIP Total Pressure Loss at 65% Engine Speed with 54% Bypass Duct Blockage

Table 4.5 – Circumferential Distortion Intensities at 65% Engine Speed with 54% Bypass Duct Blockage

Ring	DPCP _i
1	0.0078
2	0.0110
3	0.0114
4	0.0089

Table 4.6 – Circumferential Distortion Extents at 65% Engine Speed with 54% Bypass Duct Blockage

Ring	Extent (degrees)
1	174
2	168
3	164
4	153

With only one low pressure region per ring, the multiple-per-revolution pattern is again one for all rings. This matches the results from the previous two tests where the

engine was run at the same speed with no bypass duct blockage, and when the engine was run at a lower speed. Figure 4.29 shows the multiple-per-revolution pattern.

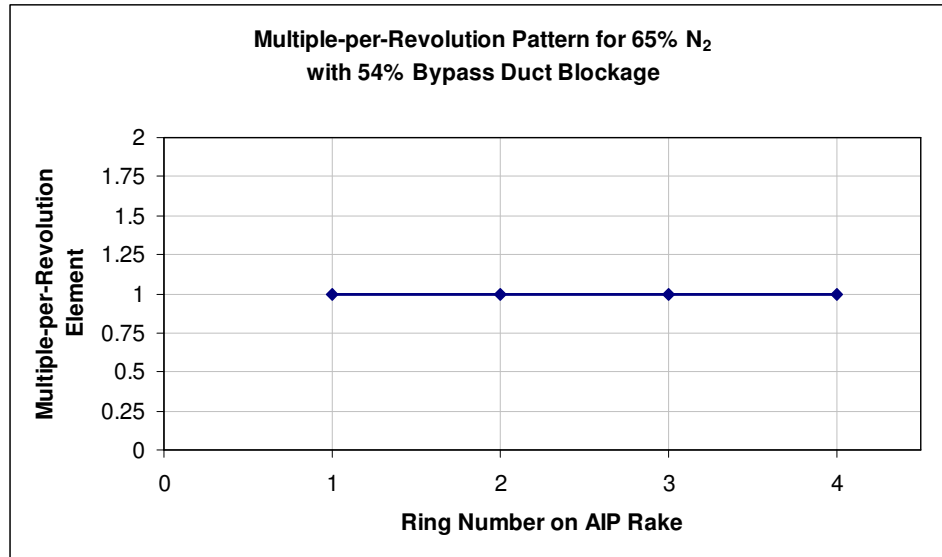


Figure 4.29 – Multiple-per-Revolution Pattern for Inlet at 65% Engine Speed with 54% Bypass Duct Blockage

4.3.2 Radial Distortion Element

The radial distortion at the AIP can be described using only the radial intensity. At fifty-five percent engine speed, the radial distortion intensity was negative for the first three radial rings, resulting in ring average total pressures that were greater than the face average total pressure. The outermost ring on the AIP measured an average total pressure that was less than the face average total pressure, resulting in a positive value. Figure 4.30 below shows a plot of the radial distortions, while Table 4.7 summarizes the values of the distortions.

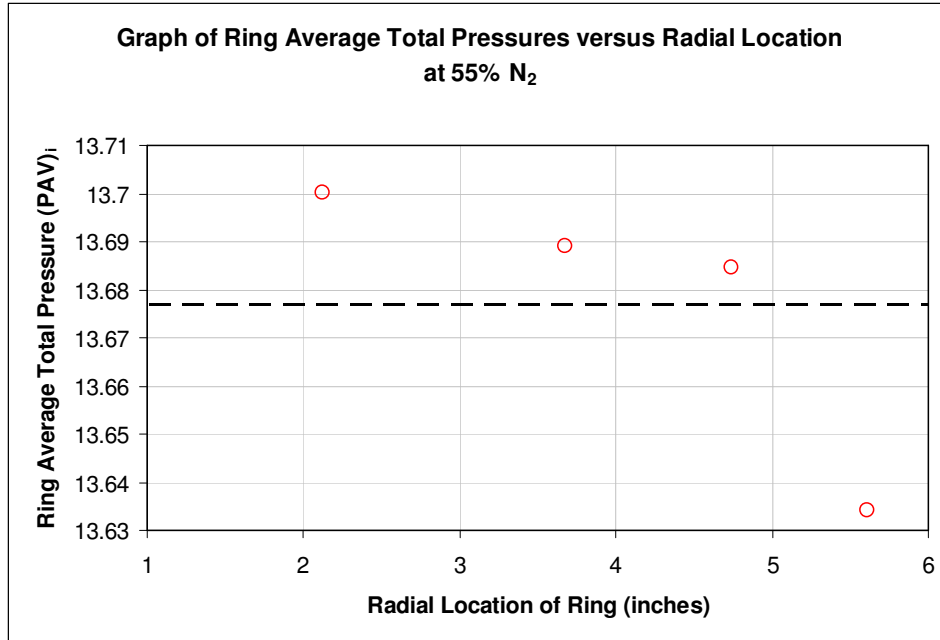


Figure 4.30 – Radial Distortion Graph at 55% Engine Speed

**Table 4.7 – Radial Distortion Intensities
at 55% Engine Speed**

Ring	DPRP _i
1	-0.0017
2	-0.0009
3	-0.0006
4	0.0031

At an engine speed of sixty-five percent, the same pattern of distortions existed, but the magnitudes were larger. Again, the inner three rings on the AIP rake all had ring average total pressures that were greater than the face average total pressure, resulting in negative radial distortion intensities. Only the outermost ring on the AIP rake had a positive radial distortion intensity where the ring average total pressure was less than the face average total pressure. Figure 4.31 shows the radial intensities, while Table 4.8 summarizes the values.

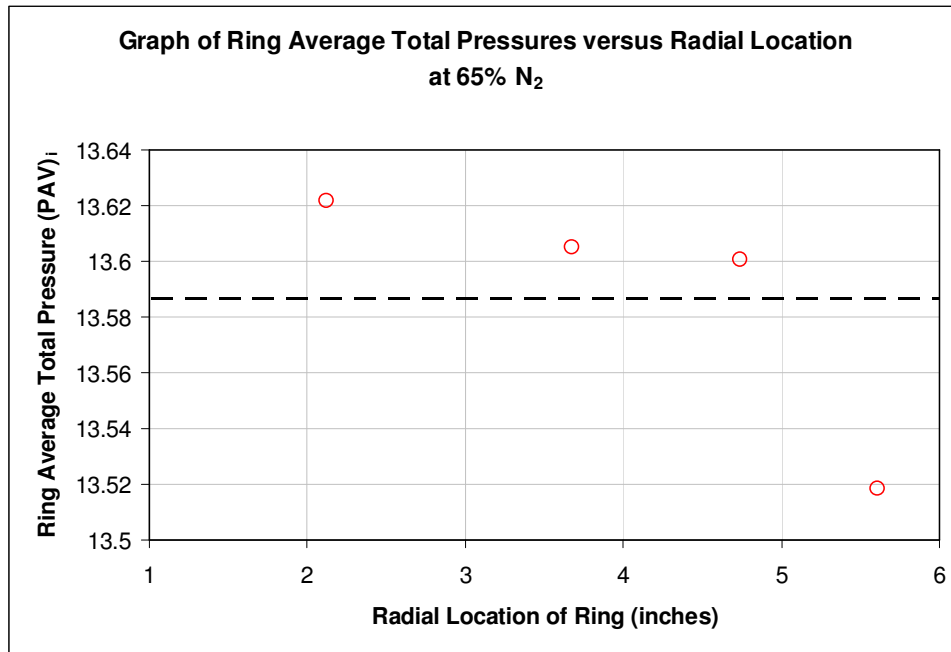


Figure 4.31 – Radial Distortion Graph at 65% Engine Speed

Table 4.8 – Radial Distortion Intensities at 65% Engine Speed

Ring	DPRP _i
1	-0.0026
2	-0.0014
3	-0.0010
4	0.0050

When the flow blockage was installed in the bypass duct, the extra mass flow that was pulled through the serpentine inlet affected the radial distortion intensity. The pattern of distortion intensities is shown below in Figure 4.27. Instead of having ring average total pressures that are constantly decreasing as the radial position of the rings increases, the pattern for this test varied across the rings. The first three rings again had negative radial distortion intensities because the ring average total pressures were greater

than the face average total pressure, but the ring average pressures increased as the radial position increased. This was opposite of the pattern that occurred in the first two tests. The outermost radial ring had the only ring average total pressure that was less than the face average total pressure, giving it the only positive distortion intensity. This was similar to the data from the first two tests. Figure 4.32 shows a graph of the distortions while Table 4.9 summarizes the values calculated.

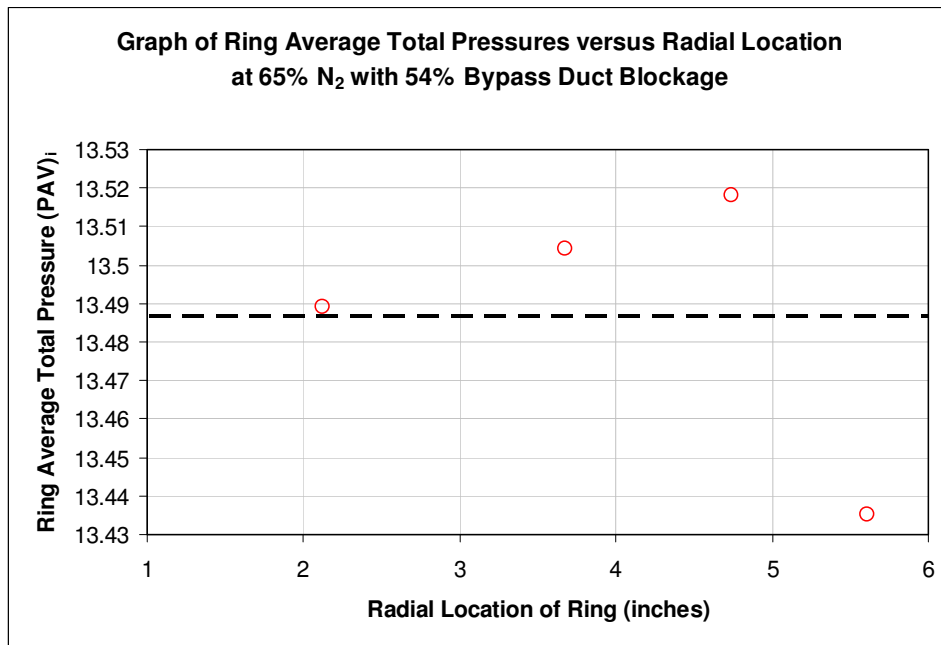


Figure 4.32 – Radial Distortion Graph at 65% Engine Speed with 54% Bypass Duct Blockage

Table 4.9 – Radial Distortion Intensities at 65% Engine Speed with 54% Bypass Duct Blockage

Ring	DPRP _i
1	-0.0002
2	-0.0013
3	-0.0023
4	0.0038

4.4 Wall Static Pressures in Serpentine Inlet

The wall static pressure measurements inside the serpentine inlet help describe the flow within the duct. Knowing the location of large static pressure losses inside the inlet can help in the design of a flow control system for the inlet. Large losses in static pressures typically means the flow has separated at that point in the inlet, and adding either suction or injection at that point could help the flow reattach and as a result, increase the static pressure.

To report the results, the static pressure was non-dimensionalized using the atmospheric pressure to better understand the losses that occurred. The axial location of the static pressure taps along the inlet, x , was also non-dimensionalized using the overall axial length of the inlet, L .

The static pressure recoveries in the serpentine inlet with no bypass duct blockage are shown below in Figures 4.33 and 4.34. While the trends of the losses were consistent between both engine speeds, the magnitudes of the losses were greater at an engine speed of sixty-five percent. One important characteristic of the flow was the large pressure loss that occurred on the top surface of the inlet at the second axial location. This location would be a good choice for inserting some type of active flow control to help reduce the pressure loss. Otherwise, the flow behaved as expected, with the static pressure losses decreasing as the flow was decelerated closer to the AIP of the inlet. The locations for these static pressure taps can be seen in Appendix C, Figures C.4 and C.5.

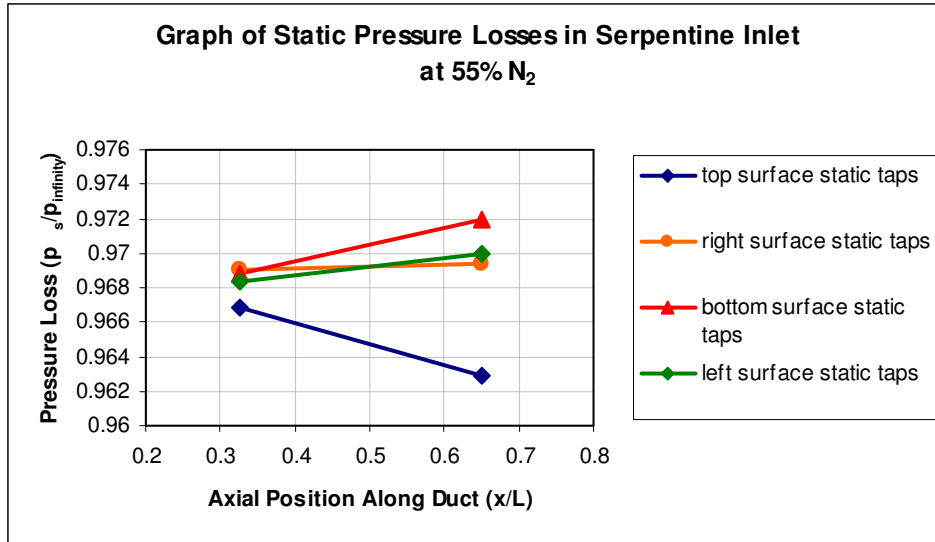


Figure 4.33 – Static Pressure Losses in Serpentine Inlet at 55% Engine Speed

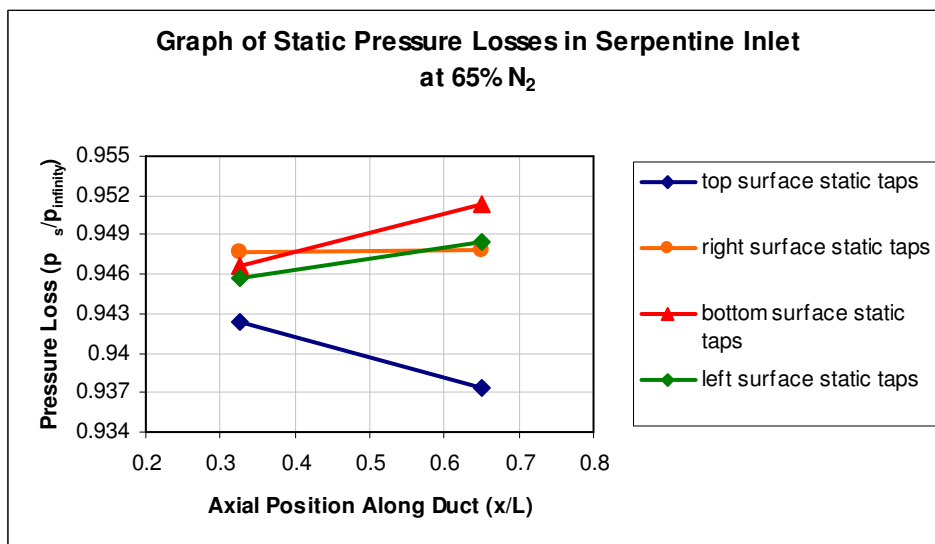


Figure 4.34 – Static Pressure Losses in Serpentine Inlet at 65% Engine Speed

When flow blockage was installed for the bypass duct with the engine operating at sixty-five percent speed, a similar trend in losses was seen when compared to the results obtained at sixty-five percent with no blockage in place. The top surface of the duct again saw the largest pressure loss, and was the only location where the pressure decreased at a further axial location along the duct. One important difference was the

increase in the magnitudes of the losses at all locations. When compared to the results with no blockage in place, increasing the mass flow through the serpentine inlet caused the static pressures to decrease at all locations. Figure 4.35 shows the resulting static pressures.

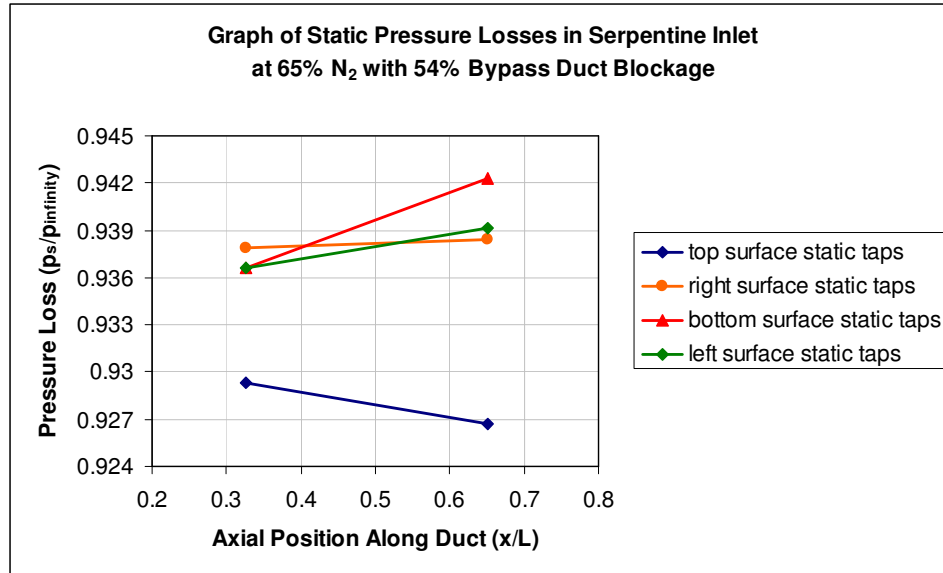


Figure 4.35 – Static Pressure Losses in Serpentine Inlet at 65% Engine Speed with 54% Bypass Duct Blockage

Because the number of pressure measurements in the facility was limited to sixty-four, only eight could be allotted to static pressure taps on the inner surface of the serpentine inlet. It was difficult to draw many meaningful conclusions from the flow inside the duct because of this limited number and the large gaps between measurements.

4.5 Comparison with NASA Results

Since experimental work had previously been performed on the serpentine inlet geometry tested here, the results of that experiment can be compared with the results of

the experiment presented here. NASA performed tests on the inlet at a range of Mach numbers between 0.25 and 0.83. Since the maximum Mach number achieved at the inlet throat when the engine was run at fifty-five percent speed was 0.19, no results were available for comparison. When the engine was run at sixty-five percent speed with and without flow blockage in the bypass duct, the maximum Mach number at the inlet throat was 0.25 in both cases, allowing those results to be compared with the NASA results.

Figure 4.36 below shows a comparison of the boundary layer profiles obtained between the NASA experiment and the experiment here. The profiles were non-dimensionalized using the freestream Mach number from the respective experiment. As the figure shows, both boundary layer profiles are fully developed at approximately forty percent, and match closely for the upper sixty percent of the inlet height. There was a difference in profiles in the bottom part of the inlet, as the NASA experiment had a smoother parabolic shape, while the experiment here followed a linear trend. The difference can be attributed in part to the locations of the boundary layer rakes. The rake in the NASA experiment was placed outside of the inlet, while the rake in the experiment here was placed in the center of the inlet three inches upstream of the throat. By placing the rake outside the opening in the inlet, the NASA experiment assumed the boundary layer had a constant profile across the width of the test section. This is likely not the case, because the lip of the inlet will have some affect on the flow, causing a slight variation in boundary layer profile from what is measured outside the inlet in the freestream.

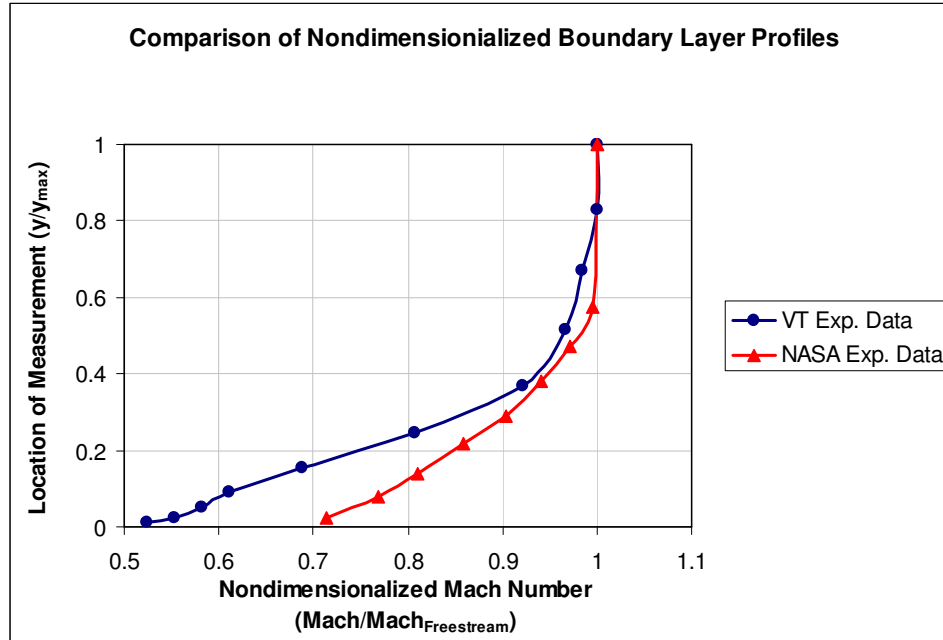


Figure 4.36 – Comparison of Nondimensionalized Boundary Layer Profiles

In addition to the boundary layer profiles, the distortion results at the AIP can also be compared between experiments. Because of a difference in AIP rakes, a comparison on a ring-by-ring basis could not be done. The NASA experiment used a forty probe AIP rake which consisted of eight arms with five probes per arm located every forty-five degrees circumferentially. The thirty-two probe rake used here was similar except it only used four probes per arm, positioning the probes at different radial locations. Table 4.10 below contains a summary of the NASA experimental results.

Table 4.10 – NASA Experimental Results

Ring	DPCP_i	Extent	DPRP_i	MPR_i
1	0.000	79	-0.009	1
2	0.004	111	-0.007	1
3	0.009	146	-0.003	1
4	0.014	150	0.002	1
5	0.013	119	0.017	1

The NASA average circumferential distortion intensity over the five rings was 0.008. When this value was compared to the average of 0.0075 over the four rings for the test at sixty-five percent speed with no flow blockage conducted here, the result was a difference of only six percent. A comparison to the average of 0.0098 obtained with the engine at sixty-five percent speed and fifty-four percent bypass duct blockage resulted in a difference of twenty-three percent. The extents recorded for the NASA experiment were smaller than the extents seen for both tests in the experiment here, meaning the NASA circumferential distortion intensity was located in a smaller angular region. The radial distortion intensities also differed from the results obtained here, ranging from -0.009 to 0.017 for NASA versus -0.003 to 0.005 for no bypass duct blockage and from -0.0023 to 0.0038 for fifty-four percent bypass blockage. The inlet total pressure recoveries agreed well for the two experiments, with NASA observing an inlet recovery ratio of 0.992. The present experiment with no bypass duct blockage showed a recovery ratio of 0.987 and with bypass duct blockage showed a recovery ratio of 0.982. The multiple-per-revolution pattern was also one for all rings in the experimental tests at both locations.

To help visualize the pressure losses at the AIP in the NASA experiment, a contour plot has been included below in Figure 4.37. This contour plot corresponds to

the data collected at Mach 0.25. The plot here can be compared to the plot in Figure 4.28 which had a similar boundary layer profile entering the serpentine inlet. The total pressure losses for the two figures have similar profiles and magnitudes, with the largest pressure losses located in the center at the bottom of the AIP.

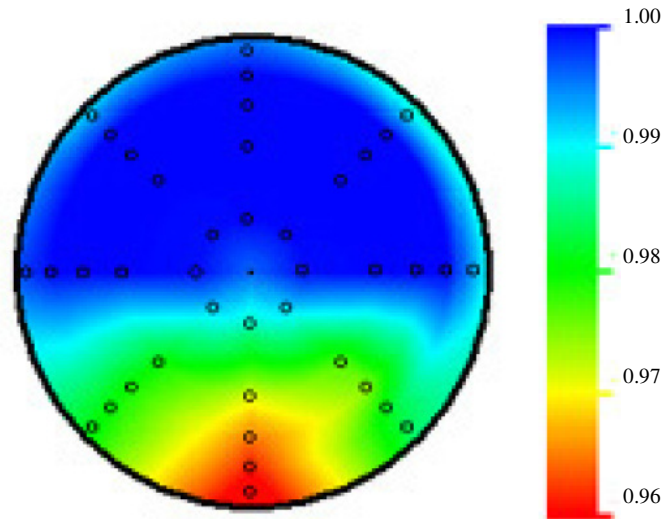


Figure 4.37 – NASA Total Pressure Loss at AIP

When performing the comparison of results, it should be noted that the NASA inlet geometry tested was a smaller-scale version of the same inlet geometry. While the inlet tested here had an AIP diameter of twelve inches, the NASA experiment used an inlet with an AIP diameter of only 2.448 inches. The Reynolds numbers for the NASA tests were also higher than the Reynolds numbers tested here. This was caused by the pressurized air in the NASA tunnel increasing the density of the air flowing through the inlet. While the results obtained in this experiment are considered to agree well with the NASA results, a difference in individual values were expected because the conditions could not be matched exactly and a different instrumentation arrangement was used.

4.6 Summary

The results presented above showed that an experimental facility capable of simulating actual flight conditions expected for serpentine inlets on BWB aircraft was successfully developed and tested. The results were presented at three different engine fan speeds (flow levels) and included a combination of tests with and without flow blockage for the bypass duct. The 30% boundary layer thickness desired was achieved at an engine fan speed of fifty-five percent, and it was proved that the boundary layer could be controlled at higher engine speeds by adjusting the flow blockage for the bypass duct. By blocking the bypass duct opening into the rear plenum by fifty-four percent, the boundary layer profile at sixty-five percent engine speed was altered to become fully developed at forty-five percent of the inlet height, a significant change from the eighty-three percent boundary layer thickness at the same engine speed with no bypass duct blockage. At seventy-five percent engine speed, the boundary layer profile was again too thick; showing that additional blockage in the bypass duct was needed. The boundary layer profiles proved the ability to control the flow by showing the change in Mach number by installing blockage at the same engine speed. A maximum Mach number of almost 0.4 was achieved at the throat of the serpentine inlet, which approached the desired level of Mach 0.5. The static pressures in the facility showed safe operation of the engine and the experiment, while the static pressures in the serpentine inlet provided insight into the flow inside the duct. The measurements collected using the thirty-two probe rake at the AIP allowed the distortion generated by the serpentine inlet to be described using a combination of circumferential and radial descriptors. This AIP data collected was compared to previous experimental work from NASA, and the results

agreed well with the circumferential distortion intensity, inlet pressure recovery, and multiple-per-revolution pattern, but differed slightly in the extent and radial distortion intensity. Some differences were expected in the results since NASA used a fan-driven wind tunnel to blow air through a small-scale inlet, while the experiment here used a jet engine to create suction through a large-scale inlet. Even with these significant differences in experimental facilities, the results are considered to compare well within an acceptable margin of error.

5.0 Conclusions and Recommendations

The purpose of this project was to help develop a method for testing engines and inlets being installed on BWB aircraft using an integrated, system level approach. Although this project used a scaled-down version of a serpentine inlet for testing and separated the inlet and engine using a rear plenum chamber, it resulted in valuable research with results that can be used for current tests, and further development of integrated static ground test facilities. An experimental facility of this type had never been developed or built before, so the lessons learned and experiences gained will be beneficial for further research in this area. With NASA placing an emphasis on BWB aircraft as the airplanes of the future, methods for testing the aircraft components including the engine installation will need to be developed. This project and its results will help form the design basis for that new test strategy.

5.1 Summary of Key Results

The experimental facility developed here was able to successfully test a diffusing serpentine inlet with large amounts of boundary layer ingestion at a range of Mach numbers from 0.19 to 0.39. At an engine speed of fifty-five percent, a boundary layer profile was created that was fully developed at thirty-six percent and had a maximum Mach number at the serpentine inlet throat of 0.19. It resulted in an average circumferential distortion intensity of 0.0042 and radial distortion intensities ranging between -0.0017 and 0.0031. At an engine speed of sixty-five percent, it was proven that the boundary layer profile could be controlled by adjusting the blockage in front of the

bypass duct exit into the rear plenum. This blockage controlled the mass flow ratio between the bypass duct and serpentine inlet. Increasing the bypass duct blockage reduced its mass flow, allowing more air to be pulled through the serpentine inlet at the same engine speed. With no blockage, an eighty-three percent boundary layer profile was developed having a maximum Mach number at the serpentine inlet throat of 0.25. This resulted in an average circumferential distortion intensity of 0.0075 and radial distortion intensities between -0.0026 and 0.0050. Installing a plate that blocked fifty-four percent of the bypass duct area altered the boundary layer profile so it was fully developed at forty-five percent, but had no affect on the maximum Mach number at the serpentine inlet throat of 0.25. The average circumferential distortion intensity increased to 0.0098 while the radial distortion intensities ranged from -0.0002 to 0.0038. At an engine speed of seventy-five percent with fifty-four percent blockage in the bypass duct, the resulting boundary layer profile was not fully developed until eighty-three percent, resulting in a maximum Mach number at the serpentine inlet throat of almost 0.4. For this test, a larger blockage was needed to reduce the mass flow through the bypass duct even more to give the boundary layer desired. From all the data that was collected and processed, the most important results from these tests were achieving distortions close to the NASA experimental data, and the demonstration of the ability to control the boundary layer profile at different flows produced by different engine fan speeds by altering flow blockages in the bypass duct. These two key results prove that a validated experimental facility has been developed.

5.2 Recommendations for Future Research

With the successful completion of this project, there are several modifications that will improve the experimental facility developed. The first would be to install more static pressure measurements along the inner surfaces of the serpentine inlet. The eight static pressure taps used here were not sufficient to describe the internal flow characteristics for the inlet. Previous research showed that ducts of this geometry typically have flow separation along the bottom surface of the second curve. This phenomenon could not be confirmed because of the large distances between measurements.

Another improvement that could be made to the experimental facility would be to install an inlet ramp with an adjustable height. This would create another variable that could be altered to help deliver different boundary layer flows for test of the serpentine inlet. Adjusting the blockage in the bypass duct to reduce its mass flow rate achieved a similar result, but it also creates additional losses in the facility. These losses could prevent the engine from running at its maximum speed, reducing the maximum inlet Mach numbers for test. Having an adjustable ramp height would allow additional boundary layer control, perhaps with reduced pressure losses in the system.

With the future of commercial airplanes implementing a BWB design with embedded engines, a method for testing the serpentine inlets on these aircraft must be developed. The results of the research conducted here are considered an important first step in creating a static ground test facility capable of such tests.

6.0 References

Allan, Brian G., and Lewis R. Owens. "Numerical Modeling of Flow Control in a Boundary-Layer-Ingesting Offset Inlet Diffuser at Transonic Mach Numbers." 44th AIAA Aerospace Sciences Meeting and Exhibit. AIAA-2006-845. January, 2006.

Allan, Brian G., Lewis R. Owens, and John C. Lin. "Optimal Design of Passive Flow Control for a Boundary-Layer-Ingesting Offset Inlet Using Design-of-Experiments." 44th AIAA Aerospace Sciences Meeting and Exhibit. AIAA-2006-1049. January, 2006.

Anderson, R.E. "Aircraft Engine Inlet Pressure Distortion Testing in a Ground Test Facility." 19th Joint Propulsion Conference. AIAA-83-1233. June, 1983.

Beale, D. K. "Improving Information Productivity and Quality in Turbine Engine Ground Testing." 39th AIAA Aerospace Sciences Meeting and Exhibit. AIAA-2001-0163. January, 2001.

Berrier, Bobby L., Melissa B. Carter, and Brian G. Allan. "High Reynolds Number Investigation of a Flush-Mounted, S-Duct Inlet With Large Amounts of Boundary Layer Ingestion." NASA TP-2005-213766. September 2005.

Cengel, Yunus A., and John M. Cimbala. Fluid Mechanics : Fundamentals and Applications. New York: The McGraw-Hill Companies, Inc., 2006.

Davis, M., et al. "A Proposal for Integration of Wind Tunnel and Engine Test Programs for the Evaluation of Airframe-Propulsion Compatibility Using Numerical Simulations." Journal of Engineering for Gas Turbines and Power 124 (2002): 447-458.

Florea, Razvan. "RDEES." E-mail correspondence. February, 2008.

Harloff, Gary J., Bruce A. Reichert, and Steven R. Wellborn. "Navier-Stokes Analysis and Experimental Data Comparison of Compressible Flow in a Diffusing S-Duct." 10th Applied Aerodynamics Conference Exhibit. AIAA-92-2699. June, 1992.

Hibbeler, R.C. Mechanics of Materials: Fourth Edition. New Jersey: Prentice Hall, Inc., 2000.

Hill, Philip, and Carl Peterson. Mechanics and Thermodynamics of Propulsion. Massachusetts: Addison-Wesley Publishing Company, Inc., 1992.

Liebeck, R. H., M. A. Page, and B. K. Rawdon. "Blended-Wing-Body Subsonic Commercial Transport." 36th Aerospace Sciences Meeting and Exhibit. AIAA 98-0438. January, 1998.

Miller, Richard W., Flow Measurement Engineering Handbook: Third Edition. Massachusetts: The McGraw-Hill Companies, Inc., 1996.

National Aeronautics and Space Administration. "The Blended-Wing-Body." NASA FS-1997-24-LaRC. July 1997.

Owens, Lewis R., Brian G. Allan, and Susan A. Gorton. "Boundary-Layer-Ingesting Inlet Flow Control." 44th AIAA Aerospace Sciences Meeting and Exhibit. AIAA-2006-839. January, 2006.

Plas, A. P., et al. "Performance of a Boundary Layer Ingesting (BLI) Propulsion System." 45th AIAA Aerospace Sciences Meeting and Exhibit. AIAA-2007-450. January, 2007.

Pratt and Whitney Canada. JT15D-1/1A/1B/4/4B/4D Training Guide. Quebec, Canada: Pratt and Whitney Canada, 1999.

Rabe, Angela C. "Effectiveness of a Serpentine Inlet Duct Flow Control Scheme at Design and Off-Design Simulated Flight Conditions." Diss. Virginia Polytechnic Institute and State University, 2003.

Reichert, Bruce A. and Bruce J. Wendt. "Improving Diffusing S-Duct Performance by Secondary Flow Control." 32nd Aerospace Sciences Meeting and Exhibit. AIAA-94-0365. January, 1994.

Smith, Robert E. Jr. "Marrying Airframes and Engines in Ground Test Facilities: An Evolutionary Revolution." Journal of Aircraft 33 (1996): 649-679.

Society of Automotive Engineers. Aerospace Recommended Practice 1420: Gas Turbine Engine Inlet Flow Distortion Guidelines: Revision B. Pennsylvania: Society of Automotive Engineers, Inc., 2001.

Taylor, A. M. K. P., J. H. Whitelaw, and M. Yianneskis. "Developing Flow in S-Shaped Ducts." NASA CR-3759. February 1984.

Ting, C. T., G. Kaldschmidt, and B. E. Syltebo. "Design and Testing of New Center Inlet and S-Duct for B-727 Airplane with Refanned JT8D Engines." 13th AIAA Aerospace Sciences Meeting. AIAA-75-59. January, 1975.

Tournier, Serge. "Flow Analysis and Control in a Subsonic Inlet." Thesis. Massachusetts Institute of Technology, 2005.

Towne, Charles E. "Computation of Viscous Flow in Curved Ducts and Comparison With Experimental Data." 22nd Aerospace Sciences Meeting, AIAA-84-0531. January, 1984.

United Sensor. Probes by United Sensor Corporation. United Sensor Corporation. February, 2008 <www.unitedsensorcorp.com/>.

Wellborn, Steven R., and Theodore H. Okiishi. "A Study of the Compressible Flow Through a Diffusing S-Duct." NASA TM-106411. December 1993.

Wellborn, Steven R., Bruce A. Reichert, and Theodore H. Okiishi. "Study of the Compressible Flow in a Diffusing S-Duct." Journal of Propulsion and Power 10 (1994): 668-675.

Appendix A: Uncertainty Analysis

Due to the limited resolution of the instruments used to take measurements in experimental work, there is always an uncertainty associated with those measurements and the resulting calculations. To fully understand the results presented, an uncertainty analysis must be performed to identify sources of error in the experiment. The uncertainty for this experiment was calculated using the propagation of uncertainty. It takes into account the resolution of the instruments used, and how the calculations can be affected by that resolution.

The pressure measurements in this experiment were collected using a miniature electronic pressure transducer with a range of zero to fifteen psig. The transducer had a resolution of 0.05 percent of its full-scale value, giving it a resolution of 0.0075 psig. The uncertainty in the Mach number calculations was then found using Equation A.1.

$$U_M = \left[\left(\frac{\partial M}{\partial P_o} U_{P_o} \right)^2 + \left(\frac{\partial M}{\partial P_s} U_{P_s} \right)^2 \right] \quad \text{A.1}$$

The partial derivatives are taken with respect to Equation 3.3 above used to calculate the Mach number. The variables U_{P_o} and U_{P_s} refer to the resolution of the instruments used to take the measurements. This leads to an uncertainty in the Mach number calculations of 0.0024.

A similar method is used to calculate the uncertainties associated with the distortion measurements at the AIP. Equation A.2 calculates the uncertainty in the circumferential distortion calculation with the partial derivatives based on Equation 3.9. The resulting uncertainty was 0.00011.

$$U_{DPCP} = \left[\left(\frac{\partial DPCP}{\partial PAV} U_{PAV} \right)^2 + \left(\frac{\partial DPCP}{\partial PAVLOW} U_{PAVLOW} \right)^2 \right] \quad A.2$$

Equation A.3 calculates the uncertainty in the radial distortion calculation with the partial derivatives based on Equation 3.16. The resulting uncertainty here was also 0.00011.

$$U_{DPRP} = \left[\left(\frac{\partial DPRP}{\partial PFAV} U_{PFAV} \right)^2 + \left(\frac{\partial DPRP}{\partial PAV} U_{PAV} \right)^2 \right] \quad A.3$$

Appendix B: Material Properties for Aluminum 6061

The following properties were used to complete the structural analysis of the wind tunnel assembly consisting of the inlet ramp cover, removable Lexan section, and bypass duct cover.

Table B.1 – Summary of Aluminum 6061 Material Properties

Material Property	Value (Units)
Mass Density	2.537×10^{-4} (in ⁴)
Reference Temperature	70 (°F)
Young's Modulus	1×10^7 (in ⁶)
Poisson's Ratio	0.33
Thermal Expansion Coefficient	1.241×10^{-5} (1/°F)
Thermal Conductivity	2.064×10^{-3} (lb _f /in ²)
Yield Strength	35000 (psi)
Ultimate Strength	40001 (psi)

Appendix C: Instrumentation Numbering Scheme

The instrumentation numbering scheme provided in this appendix was used to develop a series of Matlab programs. These programs aided data postprocessing by performing calculations and generating graphs in seconds that would have taken hours if done by hand. The following figures also helped when labeling and installing tubes used to collect the pressure measurements in the experimental facility.

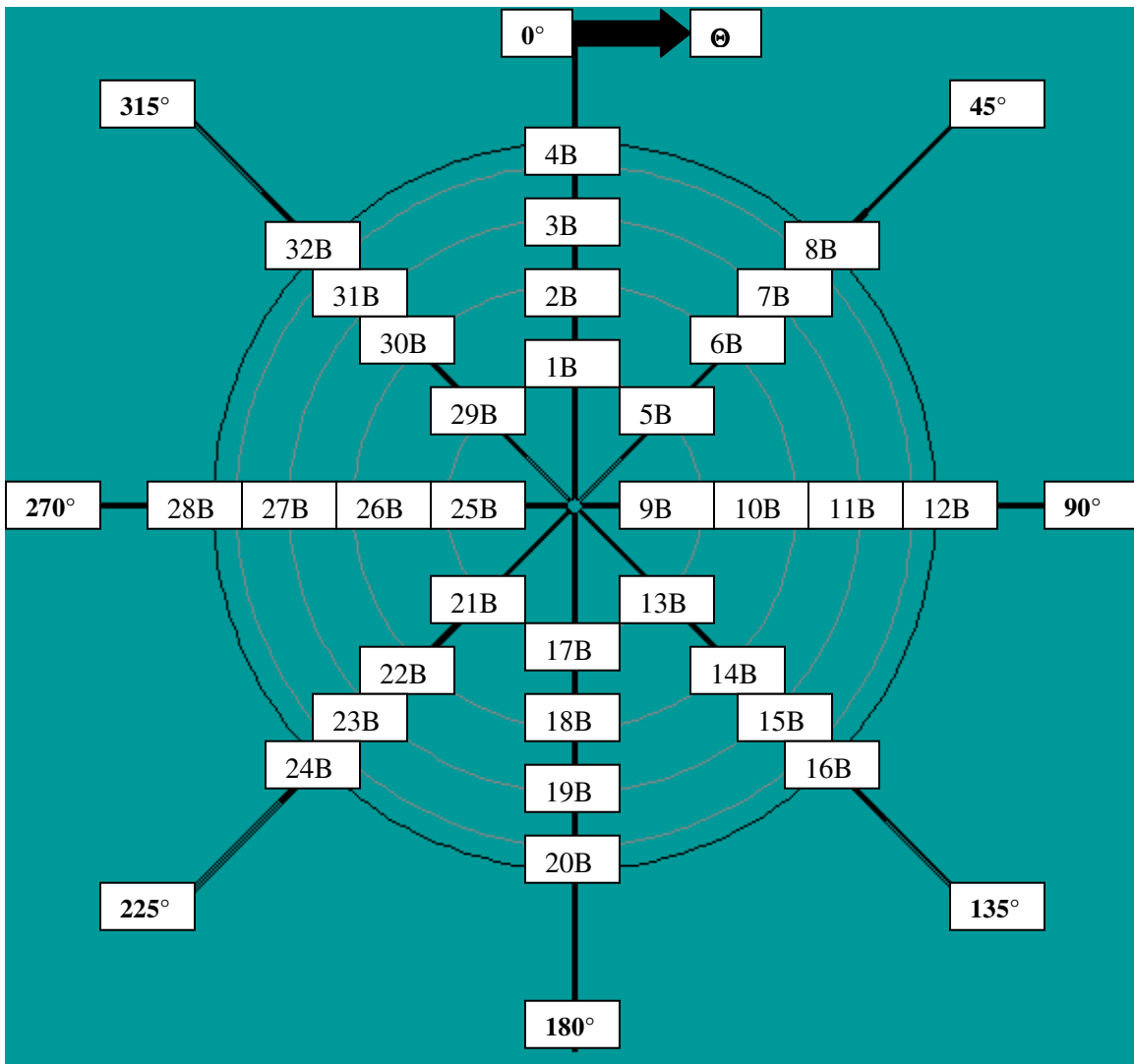


Figure C.1 – AIP Rake (Looking through AIP from Upstream)

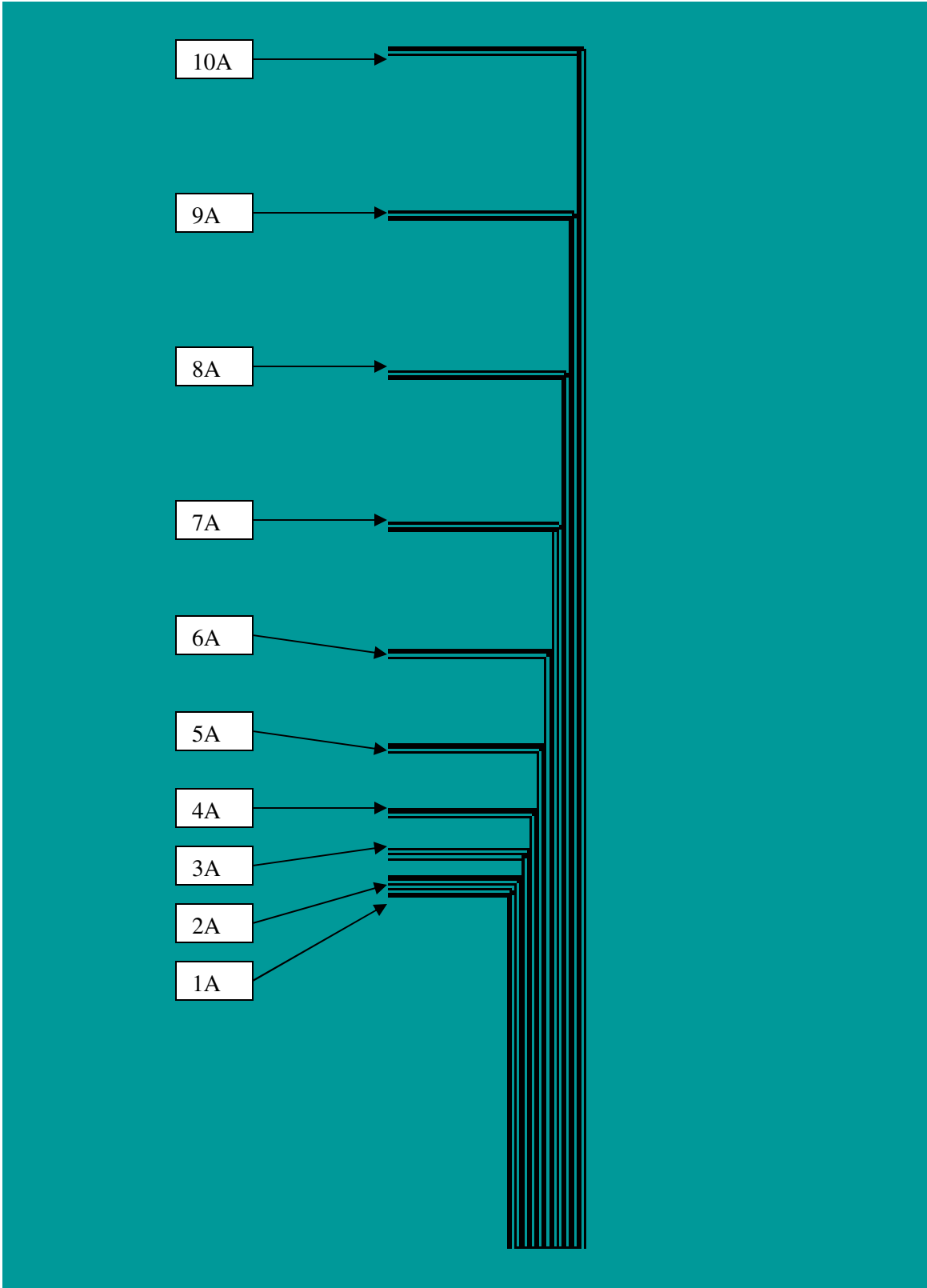


Figure C.2 – Boundary Layer Rake

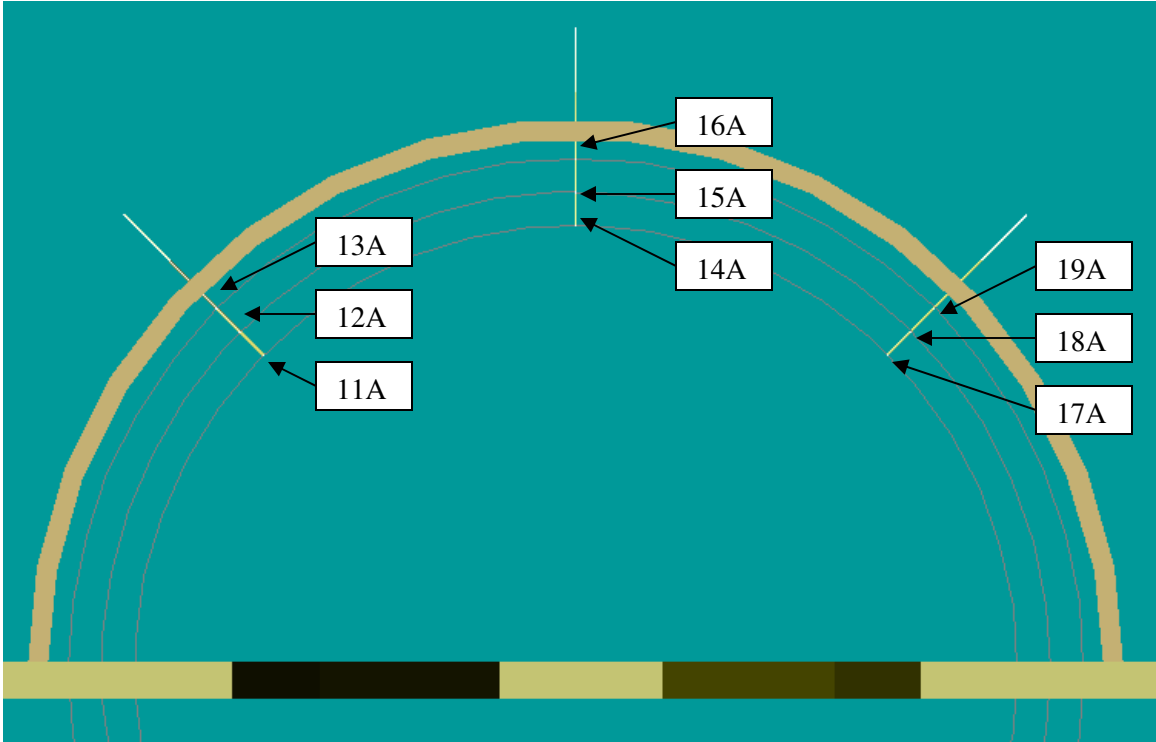


Figure C.3 – Bypass Duct Rakes (Looking through Bypass Duct from Upstream)

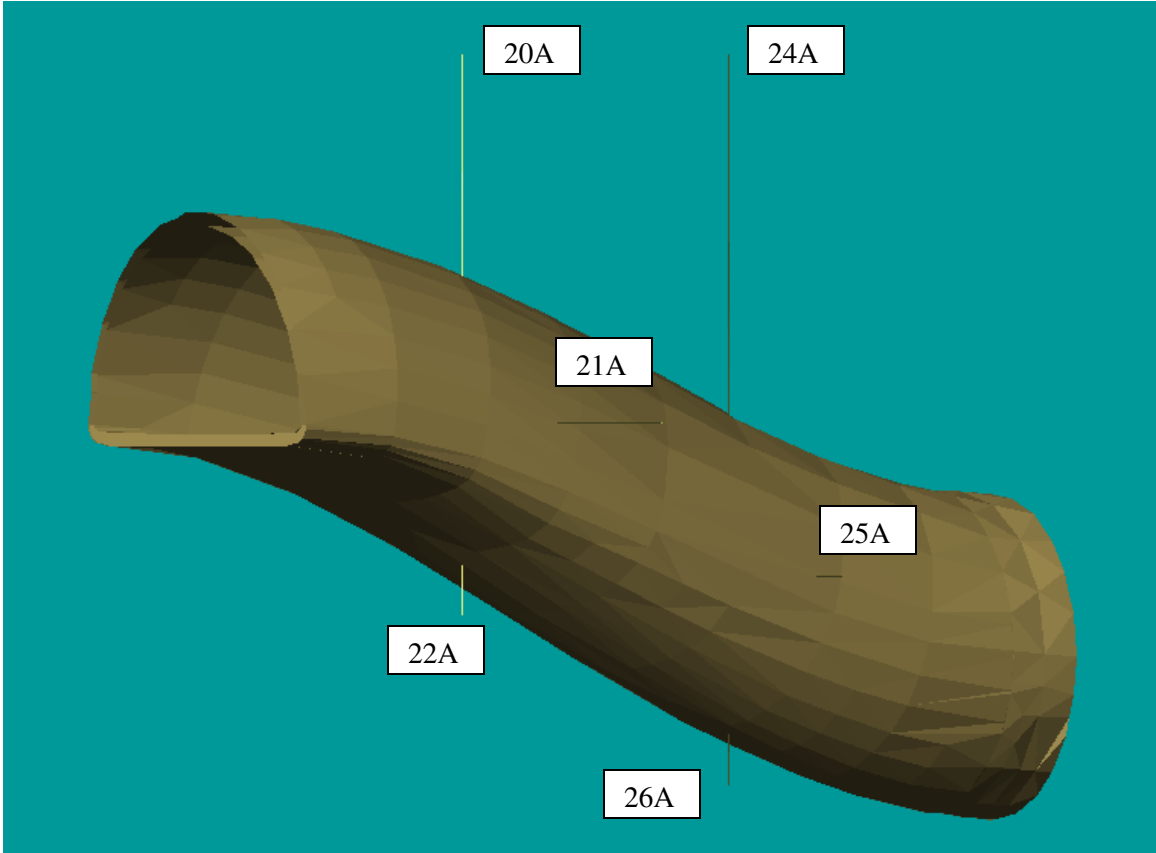


Figure C.4 – Serpentine Inlet Static Pressure Taps (View 1 of 2)

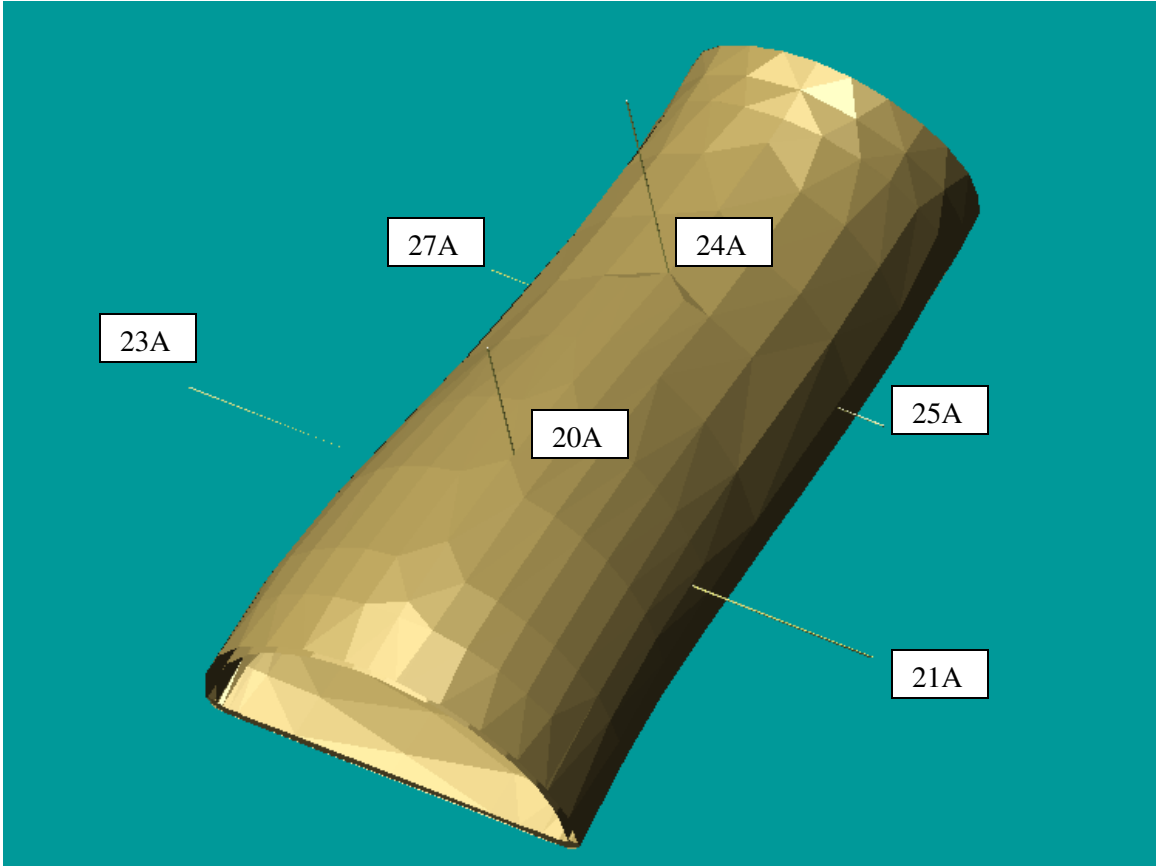


Figure C.5 – Serpentine Inlet Static Pressure Taps (View 2 of 2)

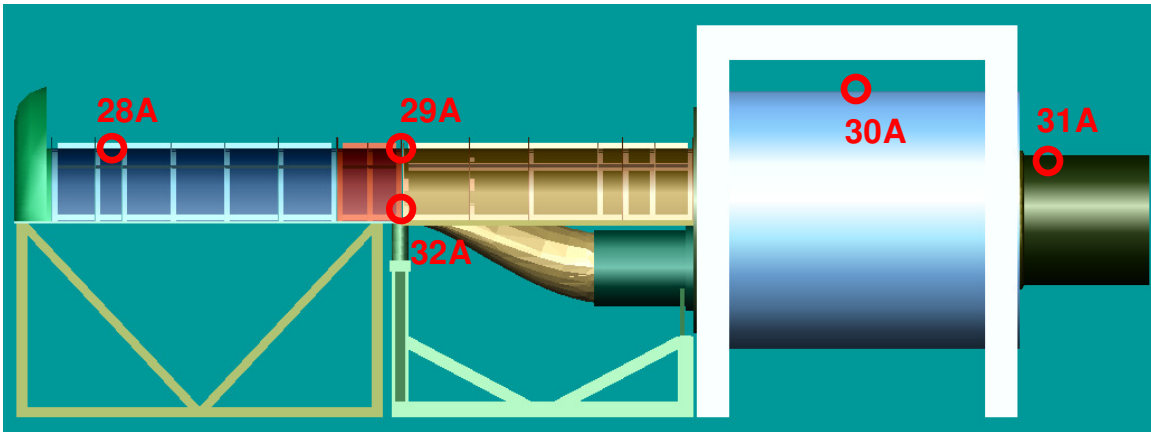


Figure C.6 – Static Pressure Taps in Experimental Facility

The following two tables below show the coordinates for the locations of these measurements. The coordinate system is centered at the AIP of the serpentine inlet, with the x-axis oriented along the axial length of the facility, the y-axis oriented vertically, and the z-axis oriented into and out of the plane of the page.

Table C.1 – Measurement Locations in Experimental Facility

Measurement Number	x location (inches)	y location (inches)	z location (inches)
1A	39.90	8.73	0.00
2A	39.90	8.84	0.00
3A	39.90	9.05	0.00
4A	39.90	9.38	0.00
5A	39.90	9.91	0.00
6A	39.90	10.68	0.00
7A	39.90	11.71	0.00
8A	39.90	12.94	0.00
9A	39.90	14.24	0.00
10A	39.90	15.59	0.00
11A	36.90	16.32	-7.69
12A	36.90	16.89	-8.26
13A	36.90	17.47	-8.84
14A	36.90	19.50	0.00
15A	36.90	20.31	0.00
16A	36.90	21.13	0.00
17A	36.90	16.32	7.69
18A	36.90	16.89	8.26
19A	36.90	17.47	8.84
20A	24.60	15.13	0.00
21A	24.60	9.38	7.75
22A	24.60	3.63	0.00
23A	24.60	9.38	-7.75
24A	12.30	9.63	0.00
25A	12.30	3.38	7.25
26A	12.30	-3.00	0.00
27A	12.30	3.38	-7.25
28A	90.90	21.63	0.00
29A	36.90	21.63	0.00
30A	-49.00	32.75	0.00
31A	-83.63	20.83	0.00
32A	39.90	8.63	0.00

Table C.2 – Measurement Locations at AIP of Serpentine Inlet

Measurement Number	x location (inches)	y location (inches)	z location (inches)
1B	0.00	2.12	0.00
2B	0.00	3.67	0.00
3B	0.00	4.74	0.00
4B	0.00	5.61	0.00
5B	0.00	1.50	1.50
6B	0.00	2.60	2.60
7B	0.00	3.35	3.35
8B	0.00	3.97	3.97
9B	0.00	0.00	2.12
10B	0.00	0.00	3.67
11B	0.00	0.00	4.74
12B	0.00	0.00	5.61
13B	0.00	-1.50	1.50
14B	0.00	-2.60	2.60
15B	0.00	-3.35	3.35
16B	0.00	-3.97	3.97
17B	0.00	-2.12	0.00
18B	0.00	-3.67	0.00
19B	0.00	-4.74	0.00
20B	0.00	-5.61	0.00
21B	0.00	-1.50	-1.50
22B	0.00	-2.60	-2.60
23B	0.00	-3.35	-3.35
24B	0.00	-3.97	-3.97
25B	0.00	0.00	-2.12
26B	0.00	0.00	-3.67
27B	0.00	0.00	-4.74
28B	0.00	0.00	-5.61
29B	0.00	1.50	-1.50
30B	0.00	2.60	-2.60
31B	0.00	3.35	-3.35
32B	0.00	3.97	-3.97

Appendix D: Experimental Facility Section Views

This appendix shows the flow path of the air at different axial locations in the facility. Sectional views are shown at each of the axial locations in the figures that follow.

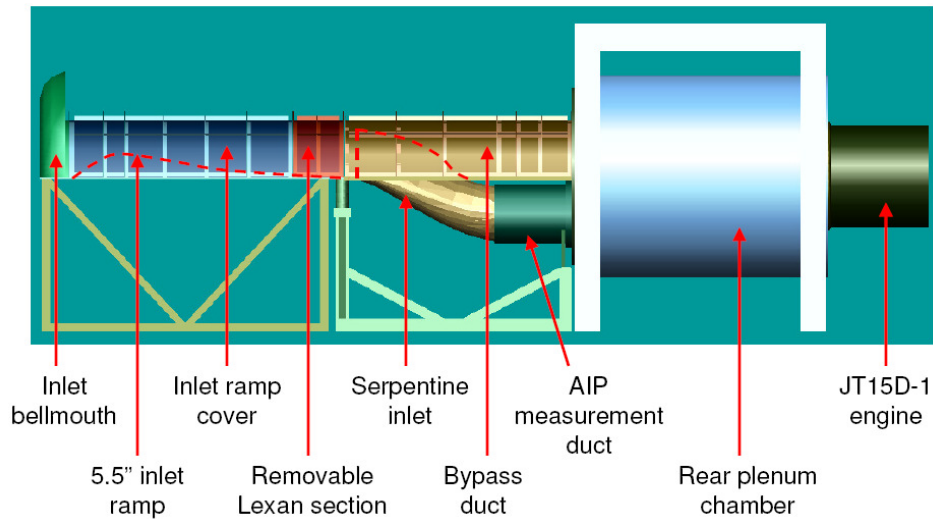


Figure D.1 – Detailed Description of Experimental Facility

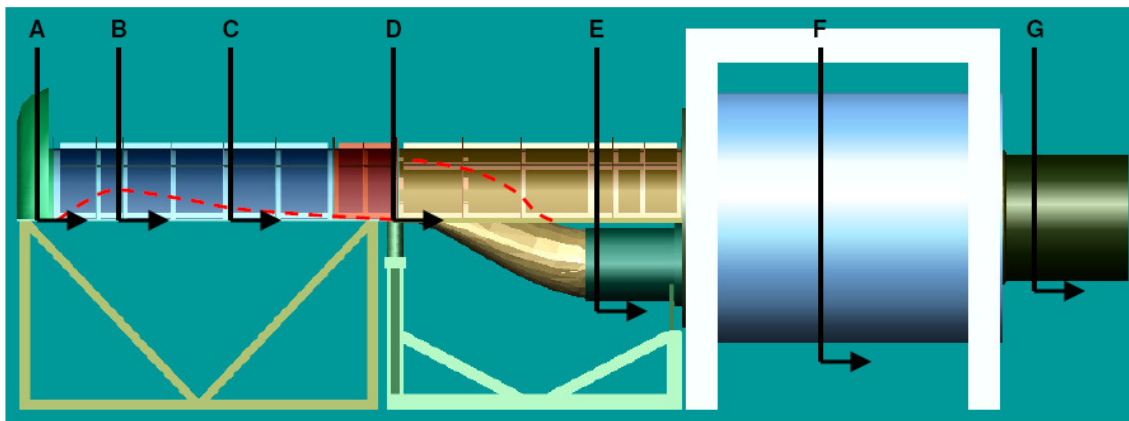


Figure D.2 – Locations of Section Views in Experimental Facility

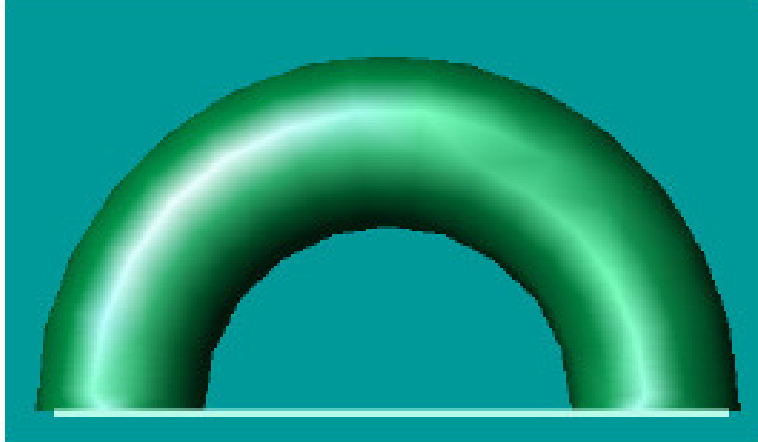


Figure D.3 – Section View A



Figure D.4 – Section View B

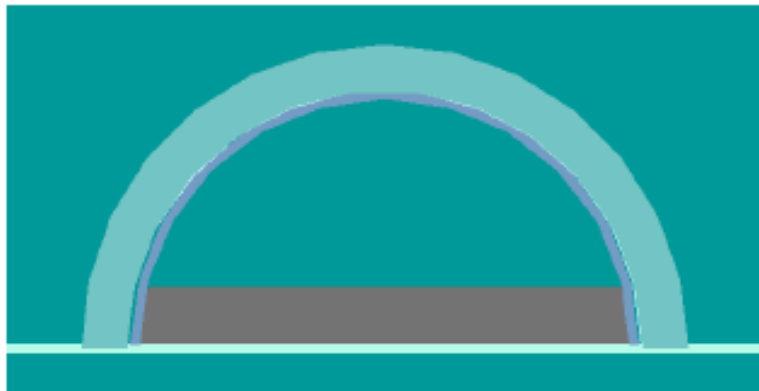


Figure D.5 – Section View C

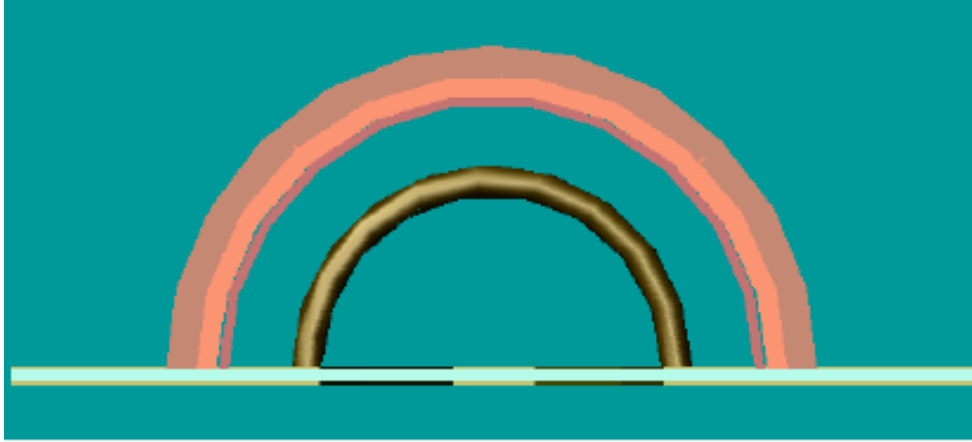


Figure D.6 – Section View D

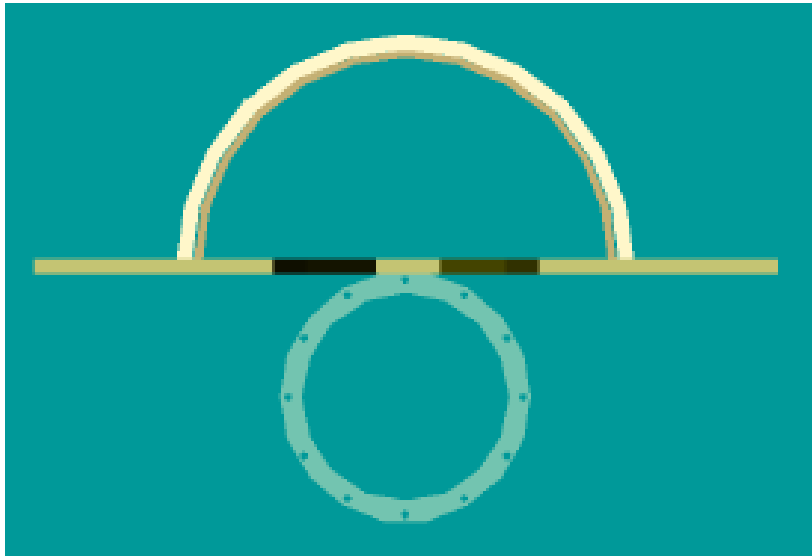


Figure D.7 – Section View E



Figure D.8 – Section View F

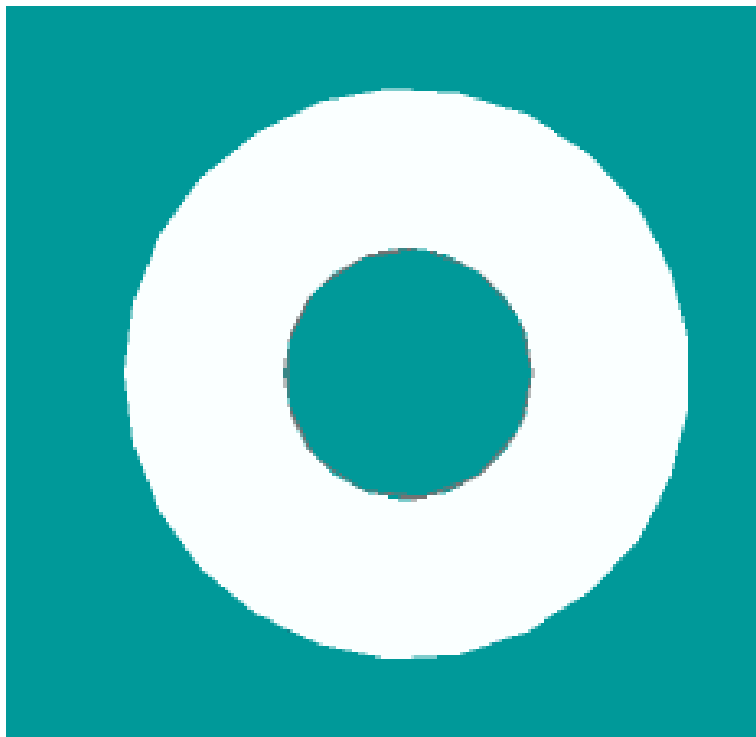


Figure D.9 – Section View G